2014

Heat Transfer Analysis of Encapsulated Phase Change Materials for Thermal Energy Storage

Ali Elmozughi
Lehigh University

Heat Transfer Analysis of Encapsulated Phase Change Materials for Thermal Energy Storage

by

Ali F Elmozughi

Presented to the Graduate and Research Committee

of Lehigh University

in Candidacy for the Degree of

Doctor of Philosophy

in

Mechanical Engineering

Lehigh University

(January 2015)

December 05, 2014

Ali F. Elmozughi

Approved and recommended for acceptance as a dissertation in partial fulfillment of the requirements for the degree of Doctor of Philosophy.

_____

Date

_____

Dr. Alparslan Oztekin, Committee Chair

_____

Accepted Date

Committee Members:

_____

Dr. Sudhakar Neti,

_____

Dr. Jacob Y Kazakia,

_____

Dr. Kemal Tuzla,

ACKNOWLEDGMENT

I would like to express the deepest appreciation to everyone who contributed to this dissertation. First I'd like to thank my advisors, Dr. Sudhakar Neti and Dr. Alparslan Oztekin for their extensive guidance and assistance during my PhD program. It would have been impossible for me to finish this research without their continuous support and encouragement.

Besides my advisors, I would like to thank my PhD. Committee Members: Dr. Kemal Tuzla and Dr. Jacob Y Kazakia for their encouragement, insightful comments. I would like to thank the other members of the Thermal Energy Storage group at Lehigh University; Dr. Wojciech Misiolek, Dr. John C. Chen, Dr. Weihuan Zhao, Dr. Ying Zheng, and fellow graduate students Laura Solomon.

I also would like to thank fellow graduate Haolin Ma and Wei Wei for their help to use ANSYS FLUENT. And I'd like to thank all my colleagues and friends at Lehigh University especially in the Lab PL201 for continuous encouragement during my study at Lehigh.

Also, I would like to thank my parent: Mr. Faraj Elmozughi and Mrs. Salha Elmozughi, and all my brother and sisters for provided me unending encouragement and support. I would thank my family in-low: Dr. Ali Shebani and Mrs. Fuzia Shita for supporting me and for continuous encouragement.

Finally, and most importantly, I would like to thank my wife: Mrs. Narjes Shiban for her unconditional support, inspiration, patience and solid love were definitely the basis upon my life and also my lovely daughter: Farah, and a little prince: Ameer.

TABLE OF CONTENTS

List Of Tables

LIST OF FIGURES

ABSTRACT

Thermal analysis of high temperature phase change materials (PCMs) is conducted. Transient two dimensional heat transfer analysis is performed to investigate high temperature energy storage and retrieval for concentrated solar power applications. The phase change materials are considered are $NaNO_3$ and the eutectic of $MgCl_2$ and NaCl. Phase change material is encapsulated by a stainless steel in a cylindrical shaped capsule. Energy storage/retrieval into/from various sizes of encapsulated phase change material (EPCM) capsules is simulated for both laminar and turbulent flow conditions of the heat transfer fluid (HTF) by an accurate modeling of the propagating liquid/solid interface in a PCM. Heat transfer inside EPCM capsule and the phase change of PCM are modeled by an enthalpy – porosity method. A two-dimensional cylindrical shaped EPCM capsule or tube is considered in simulations using gas (air) and liquid (Therminol/VP-1) as heat transfer fluids in a cross flow and an axial flow arrangement. The energy storage/retrieval times into/out of the EPCM capsule is dictated by the surface heat transfer of the EPCM for the capsule sizes considered in this study. A single horizontally placed rod in a channel with different blockage ratios for laminar and turbulence flows of HTF is studied in the present study. It is illustrated by the present work that enthalpy-porosity method can be applied to simulate heat transfer at the capsule level and the system level. System level storage module is a thermocline that includes an arrangement of several EPCMs for several megawatts of thermal energy storage (TES) for several hours used in concentrated solar power applications and other industrial thermal systems.

Transport phenomena inside the EPCM are modeled accurately by considering a 20% air void and the buoyancy-driven convection in a stainless steel capsule. The effects of the

thermal expansion and the volume expansion due to phase change on the energy storage and retrieval process are investigated. The charging and discharging into and from the capsule wall is simulated for different boundary conditions and is applied with both laminar and turbulent flow conditions. Computational models are conducted by applying an enthalpy – porosity method and volume of fluid method (VOF) to calculate the transport phenomena within the PCM capsule, including an internal air void. Energy storage and retrieval in different sized capsules is simulated. A cylindrical shaped EPCM capsule or tube is considered in simulations using both gas (air) and liquid (Therminol/VP-1) as the heat transfer fluid in a cross flow arrangement. The presence of the void has profound effects on the thermal response of the EPCM during both energy storage and retrieval process. Melting and solidification per unit mass of the PCM takes longer when the void is present. Additionally, due to material properties and the lack of convective effects, the solidification process is much slower than the melting process.

One of the most significant outcomes of the present work is that the thermal energy module in the power generation systems has to be designed properly by careful consideration of the heat transfer from HTF to the EPCM as well as the heat transport inside the EPCM.

CHAPTER 1 – Introduction

1.1. Motivation

Solar energy is the major energy source for the Earth. This energy comes from the direct radiation. Several applications such as photovoltaic or solar collector use this energy to convert either to electricity or to the thermal energy. The thermal energy uses in concentrating solar power plant to generate electricity. CSP has been implemented using various techniques that can concentrate the sunlight from 25 to 3000 times the intensity of sunlight [1].

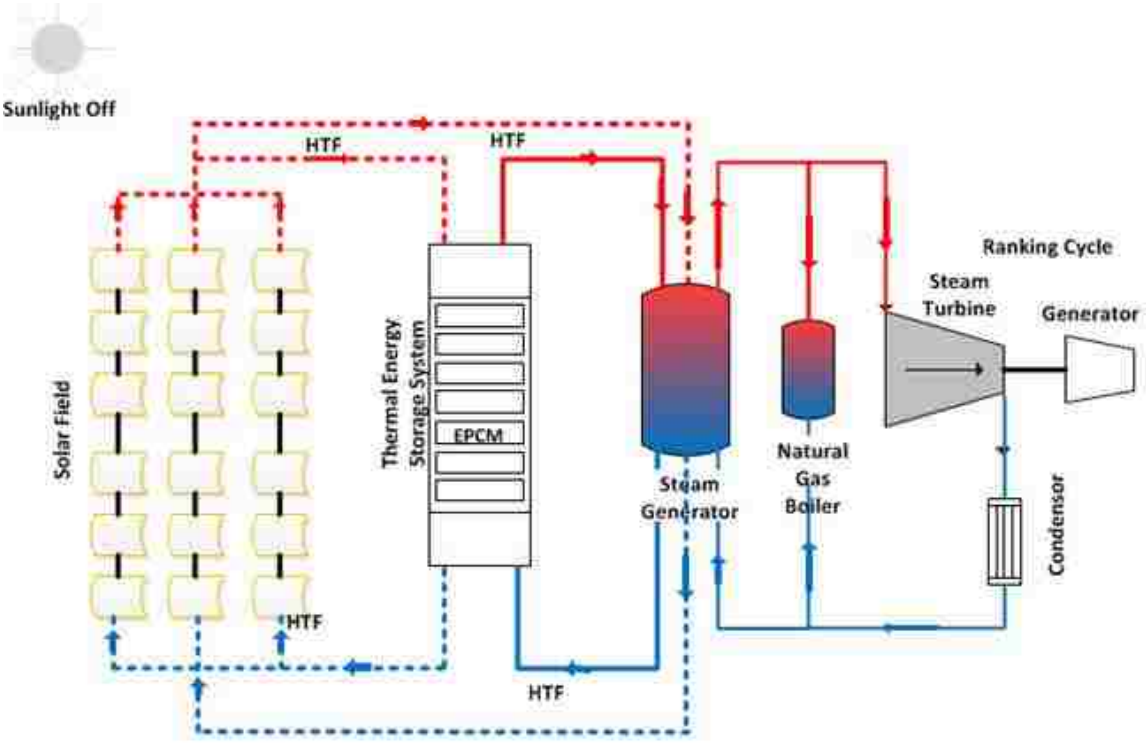

Figure 1. Schematic of a concentrated power plant that includes a thermal energy storage module.

The CSP plant is divided to four subdivisions as shown in figure 1. One of the distinctive characteristic to CSP plants is the thermal energy storage which works to help the CSP plant during cloudy weather or at night [2]. Therefore, thermal energy storage plays a key role to improve the efficiency of the power generation and to keep the stability in the grid power which then stabilizes the system resulting in improved performance at suitable cost. The thermal energy storage system can use different techniques to store energy. Varity of those techniques could be based on the method or the processing of saving dynamic energy to keep it in a certain space with a specific time regard to an application [2, 3, 4]. These techniques have capability to store and to retrieve energy in a material by either sensible heat or latent heat. Sensible heat storage systems store energy in a substance by increasing its temperature (solid or liquid). The amount of heat stored mainly based on the specific heat of the substance, and also the temperature difference. However, Sensible heat storage systems require a large volume of material to store energy. This is a major drawback of sensible heat storage systems. Latent heat storage uses phase change materials to store thermal energy by changing the phase of the substance. This technique is becoming more attractive because it works in a wide range of temperature applications. It can be used in industrial power generation systems such as solar power plants or nuclear power plants. Additionally, the thermal energy can be stored using reversible chemical reaction, this is known as thermo-chemical energy storage [3, 4]. Numerous of researchers have developed promising technologies to store thermal energy at a high temperature by using phase change materials. There are several benefits to the use of latent heat thermal energy storage technique such as minimizing the volume of storage space required compared to that of sensible heat storage techniques

and also the ability to store energy at nearly constant temperature [2, 3, 4, 5]. Studies of low temperature phase change materials are extensive [6, 7, 8]. They have demonstrated numerous advantages and the capability to apply it in wide applications under 120^{o}C. High temperature phase change materials are still developing. Several studies examine the capability of thermal energy storage to be integrated to the existing solar power plants to increase the performance. Several studies also focus on reducing the cost of per kilowatt – hour of electricity that is produced from the solar power plants to be in competitive with other resources such as fossil fuel [2].

1.2. Background and literature review

Changing phase of the latent heat thermal energy storage begins when the temperature rises and reaches the critical temperature, for instance, the melting temperature (solid to liquid). Melting process occurs at constant temperature that means the heat flux changes the internal structure of the material and stores energy in it, thus, the amount of the absorbing heat (endothermic) depends on the latent heat of the material as well as the mass. In contrast, the exothermic process to expose the heat flux out from the material and reverses back to the original phase that is called discharging process. The heat stores/retrieves during the phase change process of the material is called latent heat storage. Latent heat storage has two main advantages: storage capacity and the latent thermal energy storage systems have high storage capacity. In addition, the phase change is isothermal process, so, it has high efficiency. PCM's have capability to store and release energy in wide range of temperature applications. However, there are certain considerations that PCM has to be succeeded to be suitable to be used in latent heat

thermocline. The phase change material has to demonstrate: stability, no sub-cooling, non-toxicity, no hazard. The phase change materials, in general, can be divided into three main categories: organic, inorganic, and eutectic. They have wide range of melting temperatures so they can be used in a wide range of applications from low temperature to high temperature. The present study focuses on the thermal energy storage at temperature greater than 300ºC [3, 9, 6]. Variety of potential high melting temperature PCMs is shown in Table1 [10, 11]. The melting temperature and the latent heat of fusion of materials are two very important parameters to determine the phase change material for thermal energy storage. The range of the temperature, the thermal conductivity, and the heat of fusion of the materials also play important role in selection of PCM. Special attention should be given to the material compatibility between the encapsulation and phase change materials, and the heat transfer fluid and the encapsulation materials.

Table 1. Phase change materials with melting points from 300 °C to 800 °C [10]

Phase Change Materials Composition (mole%)	Melting Points (°C)	Heat of Fusion (kJ/kg)
NaNO3	308	173
KNO3	337	100
Zinc	420	113
NaCl/MgCl2 (57/43)	444	292
NaF/KF (40/60)	710	403.3
MgCl2	714	454
CaCl2	782	255.7
NaCl	800	430

Numerous researches have investigated latent heat storage at both low temperature and at the high temperature PCM [2, 3, 4, 9]. Latent heat thermal energy storage at high temperature for concentrated solar power applications requires further investigations. Phase change materials are classified according to their structural characteristics and according to their nature characteristics; i.e. organic or inorganic. Velraj et al. [12] reviewed the heat transfer mechanism in the PCMs and proposed a technique to enhance the heat transfer through the PCMs. Esakkimuthu et al. [13] investigated the feasibility of using an inorganic salt based PCM to store and release the excess solar energy. Mathematical model has been developed and conducted to the study the solidification and melting process using various approaches [10,13,14,15]. Computational and experimental studied have been conducted to study latent heat storage using various PCMs in different configurations [14, 15, 13, 16, 2, 17]. Numerical simulations are conducted to explore the details of the transport phenomena to store and retrieval energy using phase change materials. Assumptions such as one dimension module and using approach like front tracking are conducted. A fixed grid and an adaptive grid have been applied for studying characteristics of the phase change problem by capturing the interface. Chun and Park [18] conducted thermal analysis using fixed grid approach. Finite difference method used in this study for discretization. The enthalpy formulation used to model a phase change in one dimension discussed for slabs of pure material [19] by considering a superficial phase change region near the melting. They applied the Galerkin finite element method for varying Stefan number from 0.1 to 10. Voller [20] developed a fixed grid by using an implicit technique for conduction controlled phase change process and confirmed that a comparison of time steps shows his technique is 1.5 to 10 times faster than the previous

schemes. Mackenzie and Robertson [21] solved the nonlinear enthalpy equation using a novel semi-implicit moving mesh discretization at each time step. Brent and Voller [22] discussed a fixed-grid solution of the coupled momentum and energy equations to be undertaken without resorting to variable transformations and they used a two-dimensional dynamic model as well as the influence of laminar natural-convection flow on the melting process of pure gallium in a rectangular cavity. A semi – solid slurry and porous media for defined solid fraction in the region is conducted by [23]. Earliest numerical and experimental investigation of the unconstrained PCM melting of spherical geometry has studied by Moore and Bayazitoghu [24]. Khodadadi and Zhang [25]studied the effects of buoyancy-driven convection on the constrained melting of phase change materials within spherical containers. They used iterative finite-volume method using primitive-dependent variables and convection accounted for by using a Darcy's law with considered porous media for low temperature. They documented the effect of Prandtl number on the melting process at a fixed Rayleigh number. They showed the buoyancy-driven convection accelerates the melting process when compared to melting from diffusion models. Ismail and Moraes [26] studied the solidification of different PCMs in spherical and cylindrical shells of different materials and diameters subject to constant surface temperature. They reported the solidification is affected by the variations of the surface temperature, material and diameter of spherical shells. Tan et al. [27] reported the effect of buoyancy-driven convection of Paraffin wax n-octadecane constrained inside a transparent glass sphere through the use of thermocouples installed inside the sphere. They have solved an enthalpy – porosity equation using an iteration finite volume method. Assis et al. [28] produced a parametric investigation of low temperature melting PCM in spherical shells.

Their simulations incorporated such phenomena as convection in the liquid phase, volumetric expansion due to melting, sinking of the solid in the liquid, and close contact melting. Their model attempts to solve the complete transient conservation equations simultaneously for solid PCM, liquid PCM, and air, while allowing for PCM expansion, convection in the fluid media (melted PCM and air), and solid phase motion in the liquid. Several investigations have studied turbulent flows past cylinder by using experimental and numerical [29, 30, 31, 32]. They have examined flows past a circular cylinder confined in the channel at high Reynolds number [32]. U. Piomelli [33] reported issues related to the large-eddy simulation (LES) technique to study such flows. Sub-grid scale model is studied by U. Piomelli to describe the flow structure of flow field. Large-eddy simulation and Reynolds average Navier – stokes are used to model turbulent flows. Mehmet Sahin and Robert G. Owens [34] studied flows past an object confined a channel to examine the proximity of wall effects on the Strouhal number and the wake structure behind the cylinder for various of blockage ratios of 0.1 to 0.9 for $0 < Re \leqslant 280$.

1.3. Objectives

The main objective of this study is to conduct thermal analysis for an encapsulated phase change material (EPCM). The buoyancy-driven convection in the molten PCM and the void are included in the thermal analysis. The effect of flow characteristics of the heat transfer fluid on the thermal energy storage into the PCM is also studied here. The results presented here would assists in the designing of a latent heat thermocline storage module for concentrated solar power applications.

Chapter 2 – Mathematical Model and Numerical Method

The thermal analysis of an EPCM capsule has been performed for various phase change materials in different geometries under various boundary conditions. Simulations are conducted to model thermal energy storage/retrieval to/from EPCM. Following assumptions are considered:

1. Two - dimensional geometries.
2. PCM is a pure substance, no moisture or impurities so the sub-cooling effects are negligible.
3. EPCM is placed in a cross flow with the heat transfer fluid.
4. Molten PCM and the heat transfer fluid are considered to be incompressible flow.
5. Physical properties such as viscosity, thermal conductivity, specific heats of solid and molten PCM are constant.

Heat transfer analyses are performed for high melting temperature EPCM capsules. Two-dimensional transient heat transfer simulations are conducted for different sizes of capsules using different types of heat transfer fluids at various flow conditions. Furthermore, simulations are conducted for a single horizontally placed rod in a channel with different blockage ratios for laminar and turbulence flows of heat transfer fluid. Boussinesq approximation is adopted for the buoyancy-driven convection in the molten PCM with gravity effects. The volume of fluid (VOF) method is applied to treat the multiphase media which consists of air, being treated as an ideal gas, and the molten salt expansion (liquid region). Air is treated as an ideal gas. A computational solution of the

PCM and air system is solved using the enthalpy-porosity method and VOF approach simultaneously. The computational domain in the PCM will be divided into three regions; a solid, a liquid, and a mushy zone (porosity region). As the temperature distribution is determined, the liquid fraction, γ, can be calculated. Thus the solid, liquid, and mushy zones can be identified. A value of $\gamma = 0$ and 1 denotes the solid and the liquid regions, respectively, while $0 < \gamma < 1$ denotes the mushy zone. The heat transfer analysis of an EPCM capsule with an internal air void is being studied by modeling the phase changes within the capsule for various geometries and boundary conditions. Air and VP-1 were used as heat transfer fluids. Additionally, the phase change within a sphere with a constant surface temperature was examined. A 20% internal air void located at the top of the capsule was considered in every case.

2.1. External flow past EPCM

Heat transfer fluid flows past an EPCM have been examined. Flows of HTF past an EPCM could be laminar or turbulent depending on the fluid speeds and the type of heat transfer fluid. Flow regime is determined by the Reynolds number:

$$Re = \frac{\rho u D}{\mu} \qquad (2\text{-}1)$$

Here:

ρ: Density of the heat transfer fluid (kg/m^3)

u: The average velocity in the channel (m/sec)

D: The diameter of the capsule (m)

μ: The viscosity of the heat transfer fluid ($N.m/sec$)

2.1.1. Laminar flow model

Equations governing the laminar flow are:

- The conservation of mass:

$$\frac{\partial \rho}{\partial t} + \frac{\partial (\rho u_i)}{\partial x_i} = 0 \qquad (2\text{-}2)$$

- The conservation of momentum:

$$\frac{\partial}{\partial t}(\rho u_i) + \frac{\partial}{\partial x_i}(\rho u_j u_i) = \mu \left(\frac{\partial^2 u_i}{\partial x_j \partial x_j} \right) - \frac{\partial P}{\partial x_i} \qquad (2\text{-}3)$$

Here ρ is the density of fluid, u_i is the velocity vector, μ is the viscosity of the fluid. The flow is incompressible.

2.1.2. Turbulence model

For high Reynolds flows, surface heat transfer of an EPCM should be characterized by a proper modeling of heat transfer and fluid flow analysis of the heat transfer fluid. The Reynolds average Navier – Stokes (RANS) and the large eddy simulation (LES) are employed to study turbulent flows pass an EPCM.

I. Reynolds Averaged Navier-Stokes (RANS)

RANS methods are commonly used to model turbulent flows. The model is based on a statistical time-average of the flow properties. The overall velocity vector (u) can be

defined by a mean velocity ($\bar{u}$) and a fluctuating component about the mean (u′) [17, 35, 36].

$$u = \bar{u} + u` \qquad (2\text{-}4)$$

Time average conservation equations are written as

$$\frac{\partial \rho}{\partial t} + \frac{\partial (\rho u_i)}{\partial x_i} = 0 \qquad (2\text{-}5)$$

$$\frac{\partial (\rho u_i)}{\partial t} + \frac{\partial}{\partial x_j}(\rho u_i u_j) = -\frac{\partial p}{\partial x_i} + \frac{\partial}{\partial x_j}\left[\mu\left(\frac{\partial u_i}{\partial x_j} + \frac{\partial u_j}{\partial x_i} - \frac{2}{3}\delta_{ij}\frac{\partial u_l}{\partial x_l}\right)\right] + \frac{\partial}{\partial x_j}\left(-\rho\overline{u_i' u_j'}\right) \qquad (2\text{-}6)$$

Here, ρ is the density of the HTF, μ is the viscosity of the fluid, u_i is the time averaged velocity vector, δ_{ij} is the Kronecker delta (δ_{ij} = 0 for i ≠ j and δ_{ij} = 1 for i = j), *t* is the time and x_i is the spatial coordinate. The term $\rho\overline{u_i' u_j'}$ denotes the Reynolds stresses [36].

II. Large eddy simulation:

LES solves the Navier – Stokes equations by spatially filtering to the size of the grid. Large eddies transport the mass, momentum, and energy scalars and they possess an anisotropic behavior. On the other hand, smaller eddies are less dependent on the geometry and they display universally isotropic behavior. Typically, the grid spacing is such that most of the total turbulent kinetic energy contained in the large eddies is directly calculated. The remaining fraction of the kinetic energy must then be modeled for the flow to be physically realistic. As a result, LES suffers from the high cost of computational time at high Reynolds numbers. There is a wide range between the largest and smallest dissipative scales at high Reynolds numbers. Even though the smallest

dissipative scales are modeled, there is still a wide range of flow scales that must be calculated directly, which can be computationally intensive.

Most of the current developments to LES have been in developing sub-grid models. Some of these include the structure-function, selective structure-function, filtered structure-function, scale-similarity, mixed, and dynamic models [37]. In order to apply a sub-grid model, smaller scales of turbulence must be eliminated from the calculation through a filter. The sub-grid model is an important mode of storing and transferring kinetic energy. One of the most important functions of the filter is to distinguish between the modeled sub-grid flow and the calculated large eddy flow. This allows transfer of kinetic energy from the calculated scale to the modeled scale. Each parameter in the flow filed or scalar φ is divided into large scale $\tilde{\varphi}$ (Grid scale: GS) and small scale φ' (subgrid scale: SGS) as shown below [33, 37]:

$$\phi = \tilde{\phi} + \phi' \qquad (2\text{-}7)$$

Here:

$$\tilde{\phi}(x) = \int_V \phi(x')G(x,x')dx' \qquad (2\text{-}8)$$

Here,

$$G(x,x') = \begin{cases} \frac{1}{V} & for\ x' \in V \\ 0 & otherwise \end{cases} \qquad (2\text{-}9)$$

This expression represents the moving average equation, therefore, x' is a spatial vector and G is a function of the cell volume shown here in the equations (2-8) and (2-9).

Therefore, the equation (2-9) could be written as:

$$\tilde{\phi}(x) = \frac{1}{V}\int_V \phi(x')dx' \qquad (2\text{-}10)$$

with:

$$x' \in V \tag{2-11}$$

The governing equations that represent the LES could be written in index notation as:

$$\frac{\partial \tilde{u}_i}{\partial x_i} = 0 \tag{2-12}$$

$$\frac{\partial(\tilde{u}_i)}{\partial t} + \frac{\partial}{\partial x_j}\left(\tilde{u}_i \tilde{u}_j\right) = -\frac{1}{\rho}\frac{\partial \tilde{p}}{\partial x_i} + \frac{\partial^2 \tilde{u}_i}{\partial {x^2}_j} + \frac{\partial \tau_{ij}}{\partial x_j} \tag{2-13}$$

τ_{ij} is the stress tensor which is defined as the difference of the local average of the product of the instantaneous velocities and the product of the local averages as shown:

$$\tau_{ij} = \widetilde{u_i u_j} - \tilde{u}_i \tilde{u}_j \tag{2-14}$$

τ_{ij} is computed by relating the sub-grid stress with the turbulent viscosity and strain rate:

$$\tau_{ij} - \frac{1}{3}\delta_{ij}\tau_{kk} = -2\,\mu_i S_{ij} \tag{2-15}$$

Here:

δ_{ij}: The Kronecker delta,

S_{ij}: The rate of strain tensor,

μ_i: The SGS eddy viscosity.

The SGS eddy viscosity model is the Smagorinsky-Lilly model. In this model, the eddy viscosity is proportional to a sub-grid mixing length (*Ls*) and the strain rate tensor as defined

$$\mu_t = \rho\, L_s^2 \sqrt{2\, S_{ij} S_{ij}} \tag{2-16}$$

Overall, Smagorinsky's model is good for isotropic flows however usually breaks down near boundaries unless near wall treatment is employed since the contribution of

turbulent viscosity at the wall should be zero. Therefore, the wall boundary condition requires modifications to the mixing length [38].

$$L_s = \min(k.y, C_s.V^{1/3}) \qquad (2\text{-}17)$$

In equation (2-15), κ is the Von Karman constant (κ = 0.42), y is the distance to the closest wall, Cs is the Smagorinsky constant and V is the volume of the computational cell. Cs = 0.1 yields the best results for a wide range of flows and will be used in this research.

2.1.3. Heat transfer model

Surface heat transfer of an EPCM is modeled by the conduction and the convection.

I. Surface heat transfer from/to EPCM:

Both laminar and turbulent models are used to characterize the flow of heat transfer fluid around the capsule. For the turbulent flow, the energy equation for the heat transfer fluid is

$$\frac{\partial(\rho E)}{\partial t} + \frac{\partial}{\partial x_j}(u_i(\rho E + p)) = \frac{\partial}{\partial x_j}\left[k_{ff}\frac{\partial T_i}{\partial x_j} + \left(\tau_{ij}{}_{eff}\, u_i\right)\right] + S_h \qquad (2\text{-}18)$$

where, the energy of the fluid per unit mass is:

$$e = h - \frac{p}{\rho} + \frac{V^2}{2} \qquad (2\text{-}19)$$

Since, the fluid is incompressible h can be written as

$$h = \int_{T_{ref}}^{T} C\, dT \qquad (2\text{-}20)$$

and,

$$k_{ff} = k + \frac{C\mu_t}{P_{rt}} \qquad (2\text{-}21)$$

Here, k is the thermal conductivity and V is the fluid speed. The default value for turbulent Prandtl number $P_{rt} = 0.85$.

$(\tau_{ij})_{eff}$ is the stress tensor and it is defined as:

$$(\tau_{ij})_{eff} = \mu_{eff}\left(\frac{\partial u_i}{\partial x_j} + \frac{\partial u_j}{\partial x_i}\right) - \frac{2}{3}\mu_{eff}\frac{\partial u_k}{\partial x_k}\delta_{ij} \qquad (2\text{-}22)$$

where μ_{eff} is the effective viscosity of the fluid.

2.2. EPCM modeling

2.2.1. Enthalpy – porosity method

The enthalpy method has been used to account the latent heat fusion in energy equation by estimated a total heat value (absorbed/released) to each computational model based on the changing temperature. The enthalpy - porosity method depends on the liquid fraction which denotes the ratio of mass of liquid to the total mass in each cell. The computational domain in the PCM will be divided into three regions a solid, a liquid, and a mushy zone (porosity region). As the temperature distribution is determined, the liquid fraction, γ, can be calculated. Thus the solid, the liquid and the mushy zones can be identified. γ = 0 and 1 denotes the solid and the liquid regions, respectively, while 0 <γ< 1 denotes the mushy zone. The energy equation (2-16) could be rewritten to represent enthalpy terms as [39, 20, 40]:

$$\frac{\partial}{\partial t}(\rho H) + \frac{\partial}{\partial x_i}(\rho u_i H) = \frac{\partial}{\partial x_i}\left(k\frac{\partial T}{\partial x_i}\right) \qquad (2\text{-}23)$$

$$H_s = H_{s_{ref}} + \int_{T_{ref}}^{T} cdT \qquad (2\text{-}24)$$

$$H_L = \gamma L \qquad (2\text{-}25)$$

$$H = H_s + H_L \qquad (2\text{-}26)$$

where H is the total enthalpy; $H_{s_{ref}}$ is the reference enthalpy; L is the latent heat of fusion; u_i is the velocity vector; ν is the kinematic viscosity of the molten PCM; T_{ref} is the reference temperature and T is the temperature. γ is determined by the following set of equations [40]:

$$\begin{bmatrix} \gamma = 0 & if & T < T_{lower} \\ \gamma = 1 & if & T > T_{upper} \\ \gamma = \frac{T - T_{lower}}{T_{upper} - T_{lower}} & if & T_{lower} < T < T_{upper} \end{bmatrix} \qquad (2\text{-}27)$$

where T_{lower} and T_{upper} are temperatures slightly below and above the melting temperatures, respectively. The values of these temperatures determine the size of the mushy region and it is selected by the algorithm based on the heating/cooling rate and the physical properties of the PCM.

2.2.2. Buoyancy – driven convection in the molten PCM

Boussinesq approximation is adopted to model the buoyancy-driven convection in the molten PCM. The equations governing the buoyancy-driven convection in the molten PCM [28, 22] are written for an incompressible fluid as

$$\frac{\partial u_i}{\partial t} + u_j \frac{\partial u_i}{\partial x_j} = \nu \frac{\partial^2 u_i}{\partial x_j \partial x_j} - \frac{1}{\rho_m} \frac{\partial p}{\partial x_i} + \frac{\rho_l}{\rho_m} g_i + S_i \qquad (2\text{-}28)$$

where u_i is the velocity vector; ν is the kinematic viscosity of the molten PCM; p is the pressure;

g_i is the gravitational acceleration vector; ρ_m is the reference density of PCM determined at the melting temperature [22, 41]; and ρ_l is the density of the liquid PCM. The density of liquid PCM can be written as

$$\rho_l = \rho_m - \rho_m \beta (T - T_m) \qquad (2\text{-}29)$$

T is the temperature; T_m is the melting temperature and β is the thermal expansion coefficient of the molten PCM. The momentum source vector in equation (2-28) is modeled as:

$$S_i = -A(\gamma) u_i \qquad (2\text{-}30)$$

with the porosity function [38].

$$A(\gamma) = \frac{C(1-\gamma)^2}{(\gamma^3 + \varepsilon)} \qquad (2\text{-}31)$$

Here C is a constant value denoting the morphology of the melting front and ε is a small computational constant [38]. The values of C and ε are chosen as 10^4 and 0.0001, respectively. The porosity function reduces the velocity to zero at a solid region. $A(\gamma)$ makes the momentum equation (Kozeny-Carman equation) for flow in porous media [38]. The buoyancy – driven convection enhances the rate of the heat transfer. The convection is induced by the density stratification promotes heat transfer in the PCM and results in the increase of the rate of which the heat is stored in EPCM. In general, the ratio of the Grashof number and square of Reynolds number as shown below [42]:

$$\frac{G_r}{R_e^2} = \frac{g \beta \Delta T L}{\vartheta^2} \qquad (2\text{-}32)$$

Where:

g: The gravity acceleration (m/sec^2)

ΔT: The temperature difference (K)

L: The characteristics length (m)

ϑ: The dynamic viscosity

β: Thermal expansion coefficient (1/K) which is calculated by

$$\beta = -\frac{1}{\rho}\left(\frac{\partial \rho}{\partial T}\right) \quad (2\text{-}33)$$

if this ratio number exceeds unity, the buoyancy – driven convection can be dominant form of the convection. The strength of the buoyancy-driven can be measured by the Rayleigh number

$$R_a = \frac{g\beta \Delta T L^3 \rho}{\mu \alpha} \quad (2\text{-}34)$$

Here, g is the magnitude of the gravitational acceleration; β is the thermal expansion coefficient of the liquid PCM; ΔT is the representative temperature difference; υ is the kinematic viscosity and α is the thermal diffusivity of the liquid PCM:

$$\alpha = \frac{k}{\rho\, C} \quad (2\text{-}35)$$

The significance of the buoyancy – driven convection is discussed further below.

2.2.3. Volume of fluid - VOF

According to the volume fraction, each cell either is completely defined by one of two phases or defined by the transitional region where the line of interface is localized. Therefore, the VOF in the cell could be calculated by: $\alpha_{i,j}\Delta x\,.\,\Delta y$ where $\Delta x \; and \; \Delta y$ is grid in x and y spaces. It could be written as:

$$\alpha_{i,j}\Delta x\,.\,\Delta y \approx \int_i \int_j \alpha_{i,j} dx dy \quad (2\text{-}36)$$

Here, $\alpha_{i,j}$ is the volume fraction function in equation *(2-36)* and it is advected with the flow. To evaluate the volume conservation at each cell, Sum of all volume fluxes must be equal to the total volume flux. For instance:

$$\sum dV_{i+\frac{1}{2},j} = V_{i+\frac{1}{2},j} = \left(\Delta t\, u_{i+\frac{1}{2},j}\right) A_{i+\frac{1}{2},j} \qquad (2\text{-}37)$$

where A is the area of edge vector. Based on the face velocity at the east face of the cell, control volume can be calculated by using equation *(2-37)*. As shown in figure 2, fluid fluxed into the neighbor cell can be calculated as

$$\alpha_e u_e = u_{i+1/2,j} = \frac{V_{i+\frac{1}{2},j}}{\Delta t \times \Delta y} \qquad (2\text{-}38)$$

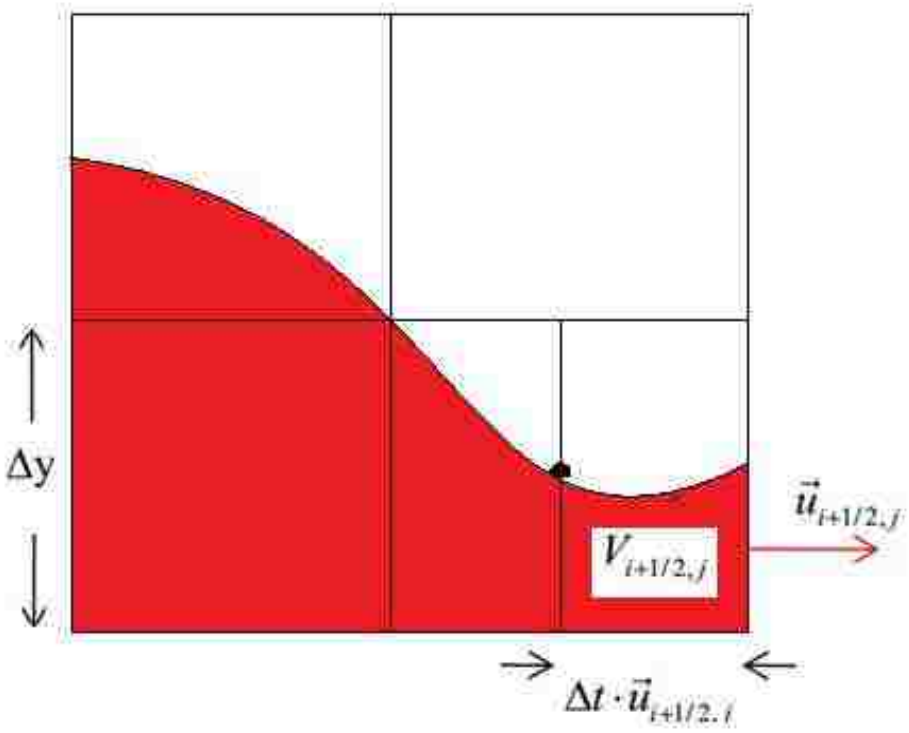

Figure 2. A computational cell for flux calculation.

PCM – Air system is modeled by the volume of fluid approach. VOF method can be simulated two or more immiscible fluids by computing one set of momentum equations and capturing the volume fraction of each fluids, α_q . The interface between the phases is tracked and obtained by the solution of a continuity equation for the volume fraction of phases.

$$\frac{\partial \alpha_q}{\partial t} + u \frac{\partial \alpha_q}{\partial x_i} = 0 \qquad (2\text{-}39)$$

Here, $\alpha_q = 0$ denotes the case that the cell does not contain q_{th} fluid, $\alpha_q = 1$ denotes the case that the cell contains %100 of qth fluid, or $0 < \alpha_q < 1$ denotes the case that cell contains the interface between the q_{th} fluid and another fluid.

2.3. Numerical model

The equations governing the fluid motion of the heat transfer fluid and the PCM and heat transfer inside and outside the EPCM is solved using the commercial software ANSYS – FLUENT

2.3.1. Discretization in the FLUENT: general transport equation

ANSYS - FLUENT uses a finite-volume-based technique to convert the governing equations to algebraic equations (discretization). The set of coupled nonlinear algebraic equations is solved numerically. The control volume technique consists of integrating the governing equations about each control volume; it yields discrete equations that conserve

each quantity on a control-volume basis [38]. FLUENT applies the discretization of the set of equations of the computational domain [17].

$$\int_V \frac{\partial \rho\varphi}{\partial t} dV + \oint \rho\varphi \, \vec{u} \, . \, d\vec{A} = \oint \Gamma \, \nabla\varphi \, . \, d\vec{A} + \int_V S_\varphi \, dV \qquad (2\text{-}40)$$

Here: ρ is the density, $\vec{u}$ is the velocity vector, $\vec{A}$ is the surface area vector, S_φ is the source term per unit volume. At each control volume or cell in the domain, this integration is applied in the domain [17, 43]:

$$\frac{\partial \rho\varphi}{\partial t} V + \sum_f^{N_{face}} \rho_f \varphi_f u_f . \overrightarrow{A_f} = \sum_f^{N_{face}} \Gamma_\varphi \, \nabla\varphi \, . \, \overrightarrow{A_f} + S_\varphi \, V \qquad (2\text{-}41)$$

Here, N_{face} is the number of faces of surrounding cells.

2.3.1.1. Temporal discretization

Here, the temporal discretization $\frac{\partial \rho\varphi}{\partial t}$ includes the integration of every term in the governing equations over a time step Δt. In general, as shown below, the transient term is evaluated for a scalar variable φ as:

$$\frac{\varphi^{n+1} - \varphi^n}{\Delta t} = F(\varphi) \qquad (2\text{-}42)$$

where n+1 denotes the future time, n denotes current time. The implicit method is used to calculate $F(\varphi)$ at the future state. It is described as:

$$\frac{\varphi^{n+1} - \varphi^n}{\Delta t} = F(\varphi^{n+1}) \qquad (2\text{-}43)$$

$F(\varphi^{n+1})$is referred to as implicit integration, rearranging equation (2-43):

$$\varphi^{n+1} = \varphi^{n} + \Delta t\, F(\varphi^{n+1}) \qquad (2\text{-}44)$$

The equation (2-44) is solved iteratively. The advantage of the fully implicit scheme is that it is unconditionally stable with respect to time step size.

2.3.1.2. Spatial Discretization - second order upwind scheme

When the second-order accuracy is wanted, quantities at cell faces are calculated using a linear re-construction approach. In this approach, higher-order accuracy is accomplished at cell faces through a Taylor series expansion. When the second-order upwind approach is selected, the face value φ_f is computed using the following expression:

$$\varphi_f = \varphi + \nabla\varphi \,.\, \Delta\bar{s} \qquad (2\text{-}45)$$

Here φ and $\nabla\varphi$ are the cell-centered value and its gradient in the upstream cell, and $\Delta\bar{s}$ is the displacement vector from the upstream cell centroid to the face centroid. This gradient is obtained using the divergence theorem, which in discrete form is written as:

$$\nabla\varphi = \frac{1}{V}\sum_{f}^{N_{face}} \tilde{\varphi} \quad \bar{A} \qquad (2\text{-}46)$$

Here, the face values $\tilde{\varphi}_f$ which are averaging φ There will not be new maxima or minima introduced as the desired value is averaged over the N_{face} concerned.

Every scalar magnitude is located at the center of the node (grid) and surrounding by neighbor cells (nodes) as shown in figure 3, therefore, a linearized form can be written as:

$$a_P\varphi_P = \sum_{nb} a_{nP}\varphi_{nb} + b \qquad (2\text{-}47)$$

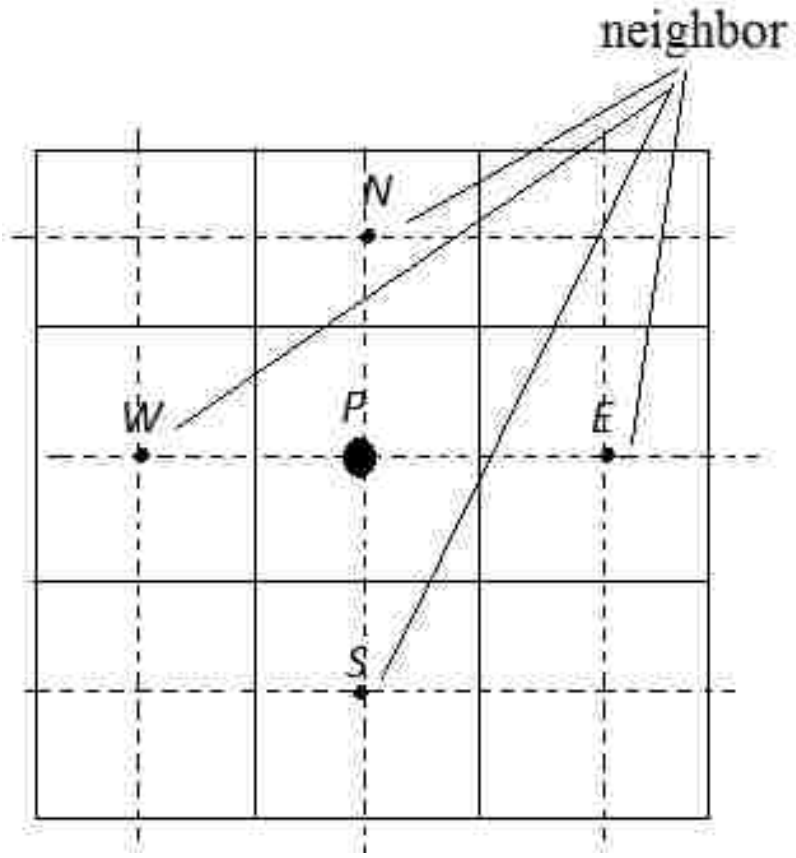

Figure 3.Central node enclosed by neighboring nodes [43].

2.3.1.3. RANS - k-ε model

ANSYS FLUENT provided several RANS turbulence models, such as Spalart-Allmaras One-Equation Model, *k-ε* model, *k-ω* model and Reynolds Stress Model (RSM). The *k-ε* model is selected for the simulation and more detailed discussions are presented in the next section. The formula of kinetic energy and rate of dissipation of the turbulent kinetic energy are described by following [38]:

$$\frac{\partial}{\partial t}(\rho k) + \frac{\partial}{\partial x_i}(\rho k\, u_i) = \frac{\partial}{\partial x_j}\left[\left(\mu + \frac{\mu_t}{\sigma k}\right)\frac{\partial k}{\partial x_j}\right] + G_k + G_b - \rho k + Y_M + S_k \qquad (2\text{-}48)$$

$$\frac{\partial}{\partial t}(\rho\varepsilon) + \frac{\partial}{\partial x_i}(\rho\varepsilon u_i) = \frac{\partial}{\partial x_j}\left[\left(\mu + \frac{\mu_t}{\sigma_\varepsilon}\right)\frac{\partial k}{\partial x_j}\right] + C_{1\varepsilon}\frac{\varepsilon}{k}(G_k + C_{3\varepsilon}G_b) - \rho C_{2\varepsilon}\frac{\varepsilon^2}{k} + S_\varepsilon \quad (2\text{-}49)$$

Here,

$$C_1 = \max\left[0.43, \frac{\eta}{\eta+5}\right] \ , \quad C_{3\varepsilon} = \tanh\left|\frac{v}{u}\right|,$$

and,

$$\eta = S\frac{k}{\varepsilon}S = \sqrt{S_{ij}S_{ij}} \quad (2\text{-}50)$$

The eddy viscosity is computed from

$$\mu_t = \rho C_\mu \frac{k^2}{\varepsilon} \quad (2\text{-}51)$$

The C_μ in the realizable k-ε model is a variable and calculated by

$$C_\mu = \frac{1}{A_0 + A_S\frac{kU^*}{\varepsilon}} \quad (2\text{-}52)$$

where

$$U^* = \sqrt{s_{ij}s_{ij} + \widetilde{\Omega}_{ij}\widetilde{\Omega}_{ij}} \quad (2\text{-}53)$$

and,

$$\widetilde{\Omega}_{ij} = \Omega_{ij} + 2\,\varepsilon_{ijk}\omega_k \quad (2\text{-}54)$$

$$\Omega_{ij} = \overline{\Omega}_{ij} + \varepsilon_{ijk}\omega_k \quad (2\text{-}55)$$

Here Ω_{ij} is the mean rate-of-rotation tensor viewed in a moving reference frame.

$$A_o = 4.04 \ , A_s = \sqrt{6}\cos(\phi) \ ,$$

Also,

$$\phi = \cos^{-1}(\sqrt{6}\,W) \quad (2\text{-}56)$$

$$W = \frac{s_{ij}s_{ik}s_{ki}}{\tilde{s}^3} \quad (2\text{-}57)$$

$$\tilde{s} = \sqrt{s_{ij}s_{ij}} \qquad (2\text{-}58)$$

$$s_{ij} = \frac{1}{2}\left(\frac{\partial u_j}{\partial x_i} + \frac{\partial u_i}{\partial x_j}\right) \qquad (2\text{-}59)$$

The values for other parameters are [38, 36]:

$$C_{1\varepsilon} = 1.44 \ ; C_2 = 1.9 \ ; \ \sigma_k = 1.0 \ ; \sigma_\varepsilon = 1.2$$

and σ_ε , σ_k are additional source terms for *k* and *ε*.

2.3.2. Solution procedure

The finite volume uses a collocated technique to store values like pressure, velocity and temperature. Time integration is calculated by a first – order implicit Euler method. For the convective term, the Green – Gauss theorem is used and the volume integral is transformed into a surface integral. ANSYS FLUENT applies a central point rule integration of the surface integral that has second – order accuracy. The convective term is simulated using a second – order upwind scheme and the diffusive term is calculated using a central-differencing scheme. The SIMPLE technique is used to solve pressure – velocity coupling. The interpolation equation is applied to calculate the face values from the mid - node values because of the collocated technique is stored the values at node center. Here, the algorithm chart is shown in figure 4 [38].

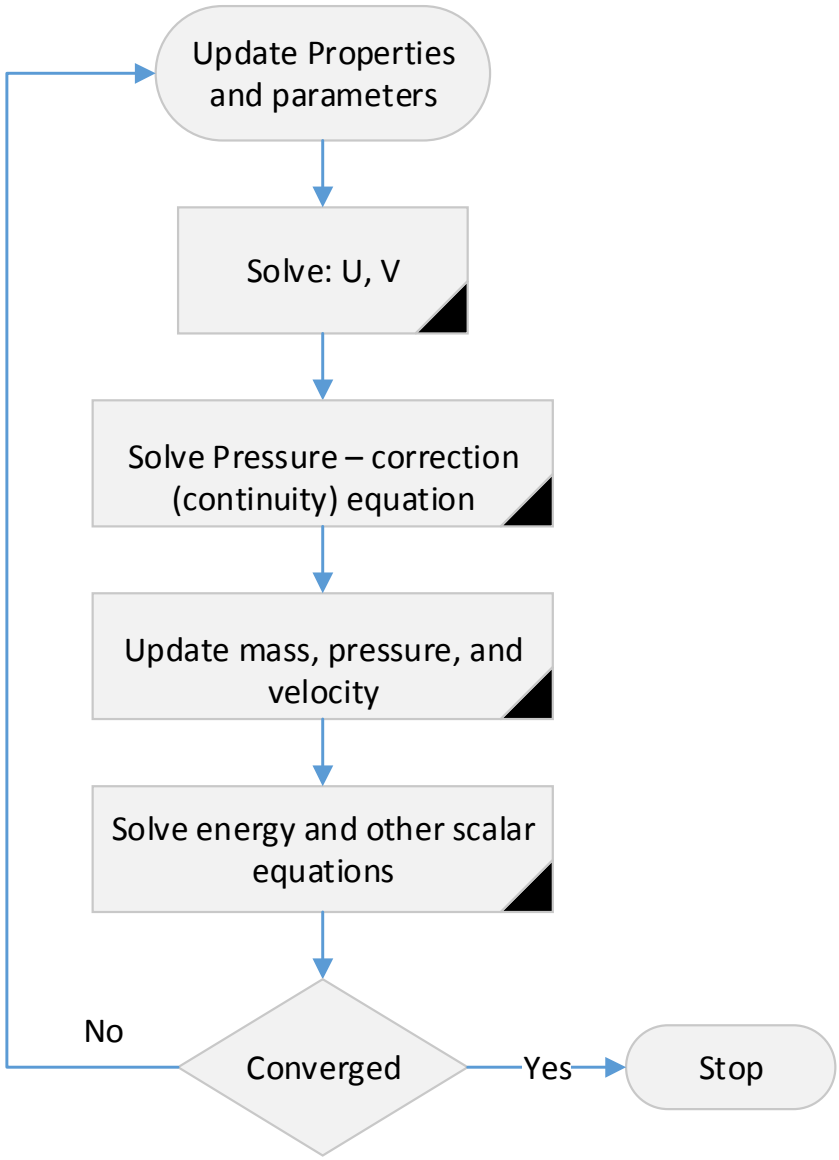

Figure 4. Flow chart for ANSYS FLUENT solution algorithm [38].

Normal initialization method is applied for initializing the velocity and temperature fields in the computational domain. Together with the continuity and momentum equations, the two equations of k-ε model will be solved with the SIMPLE algorithm. In order to achieve better accuracy, the second-order discretization is applied to unstructured meshes in the computational domain.

Results are presented for different cases in next chapters. These cases include the EPCM only analysis and the system analysis of a thermocline. The system analysis considers several EPCM in a thermocline. Specific mathematical modeling and assumptions will be described for each case. Generally, the enthalpy method is used to model the phase change and the heat transfer in the EPCM. Bousinessq approximation with VOF is used to model natural convection and the effect of void in the EPCM. Laminar and turbulent modelings are used to model convection heat transfer to/from EPCM from/to the heat transfer fluid.

CHAPTER 3 – Heat Transfer Analysis of Encapsulated Phase Change Material - Diffusion Only Process

3.1. Motivation

Transient two dimensional heat transfer analysis is conducted to investigate a high temperature energy storage using encapsulated phase change materials (EPCMs) for concentrated solar power applications. Sodium nitrate $NaNO_3$ and eutectic NaCl-$MgCl_2$ are considered as the phase change material (PCM). PCMs are encapsulated by a stainless steel cylindrical shaped capsule. Air and Therminol VP-1 are used as heat transfer fluids in a cross flow. The energy storage/retrieval times into/out of the EPCM capsule is dictated by the surface heat transfer of the EPCM. The enthalpy-porosity method can be applied to simulate heat transfer at the capsule level.

3.2. Mathematical model:

Enthalpy – porosity approach is employed to investigate the heat transfer and phase change in EPCM. Following assumption is used:

- Diffusion only process.
- No gravity.
- No volume change due to the phase change of the PCM.
- No natural convection - the buoyancy-driven in the molten PCM is neglected.

Thus, the enthalpy – porosity equation *(2-23)* can be rewritten as

$$\frac{\partial}{\partial t}(\rho H) = \nabla \cdot (k \nabla T) \qquad (3\text{-}1)$$

where ρ is the density of PCM and H is the total enthalpy. The total enthalpy consists of the sensible enthalpy and the latent heat of fusion. As mentioned earlier there are three region identified by their temperatures. k is the thermal conductivity of PCM.

This chapter will present the sensible and latent heats stored/released to/from EPCM. Storage/retrieval times for a single capsule are presented for various sizes. Iteration method is used in ANSYS FLUENT software. Iteration at each time steps continues until the residual of the energy equation reaches values below 10^{-6} for each node.

3.3. Computational domain and properties

Figure 5 shows the schematic of two-dimensional EPCM for a long cylinder. The direction of the flow is from the top of capsule to the bottom, as shown in figure 5. The half of the circle is taken as the computational domain and symmetry boundary condition is employed.

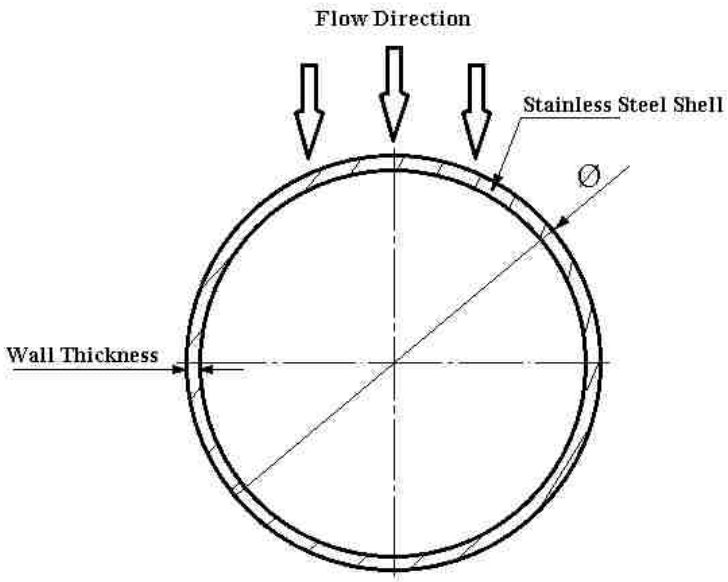

Figure 5. Schematic of the EPCM capsule.

Figure 6 shows the tringle mesh for EPCM. The triangle mesh has been created using Meshing Design software in ANSYS – FLUENT workbench. A high quality mesh is very important in the numerical solution. Thus, the proper size of the element at the interface between two zones PCM and shell will be attained. The triangular meshes have capability to provide accurate results. Mesh optimization is discussed later. It is very important to obtain sufficiently accurate results with a reasonable CPU time.

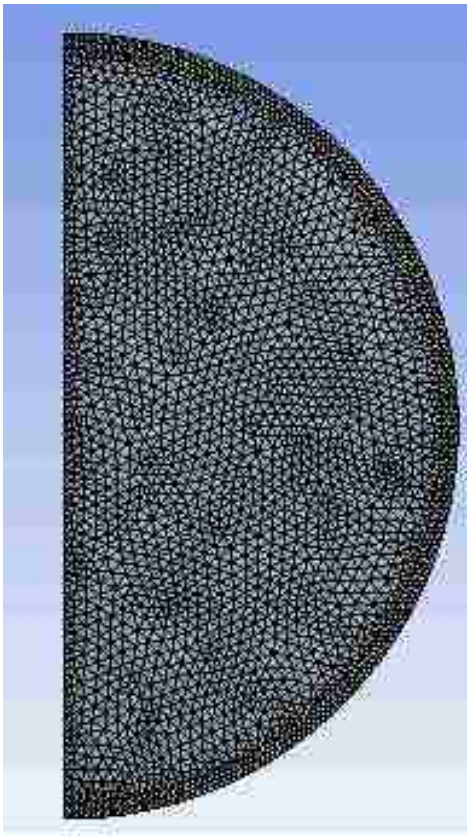

Figure 6. Mesh structure in the EPCM.

Sodium nitrate ($NaNO_3$) and Eutectic mixture of NaCl-MgCl2 (57 mole% NaCl and 43 mole% MgCl2) are considered. It is capsulated by a cylindrical stainless steel shell. The physical properties of the eutectic mixture and the capsule material (stainless steel) are listed in Table 2. Table 3 is listed physical properties of $NaNO_3$. Both Air and Therminol VP-1 (liquid) are considered as a heat transfer fluid in the present simulations. Thermodynamic properties of Air and Therminol VP-1 are listed in Table 4.

Table 2. Physical properties of eutectic NaCl-$MgCl_2$ and stainless steel

	NaCl-$MgCl_2$		Stainless Steel
	Solid	Liquid	
Density (kg/m^3)	2072 [44]	1750 [44]	7900 [32]
Specific Heat (J/kg·K)	885 [a] [11]	1220 [a] [9]	477
Thermal Conductivity(W/m·K)	0.5 [45]		14.9
Melting Point (°C)	444 [46]		---
Latent Heat (kJ/kg)	296 [11]		---

Table 3. Physical properties of $NaNO_3$

	Density (kg/m3)	Thermal Conductivity (W/m·K)	Specific Heat (J/kg·K)	Latent Heat (kJ/kg)
Solid $NaNO_3$	2,260 [47]	0.5 [48]	1,588 [49]	162.5 [49]
Liquid $NaNO_3$	1,900 [44]	0.5 [48]	1,650 [49]	

Table 4. Physical properties of HTF , air [42] and liquid Therminol/VP-1 [50]

	Air (1 atm, 800 K)	Liquid Therminol/VP-1 (698 K)
Density (kg/m^3)	0.4	654
k (W/m·K)	0.057	0.07
c_p (J/kg·K)	1099	2760
Viscosity (N·s/m^2)	3.7×10^{-5}	1.34×10^{-4}
Prandtl number, *Pr*	0.7	5.3
Reynolds number, *Re*	1,230	29,752

3.3.1. Boundary and initial conditions

Two different sizes of the EPCM are considered: 76.2 mm diameter and 25.4 mm diameter. For the range of mass flow rate of HTF in the thermocline between 0.01 kg/s and 0.05 kg/s, the superficial velocity in the thermocline is calculated. Using the Reynolds number determined by the superficial velocity and the diameter of the capsule, the local Nusselt number around cylinder is obtained [51, 52]. The heat transfer coefficient used in the heat transfer analysis of EPCM capsule for enthalpy method is determined from the Nusselt number. Figure 7 depicts the heat transfer coefficient for air and Therminol/VP-1 as heat transfer fluids.

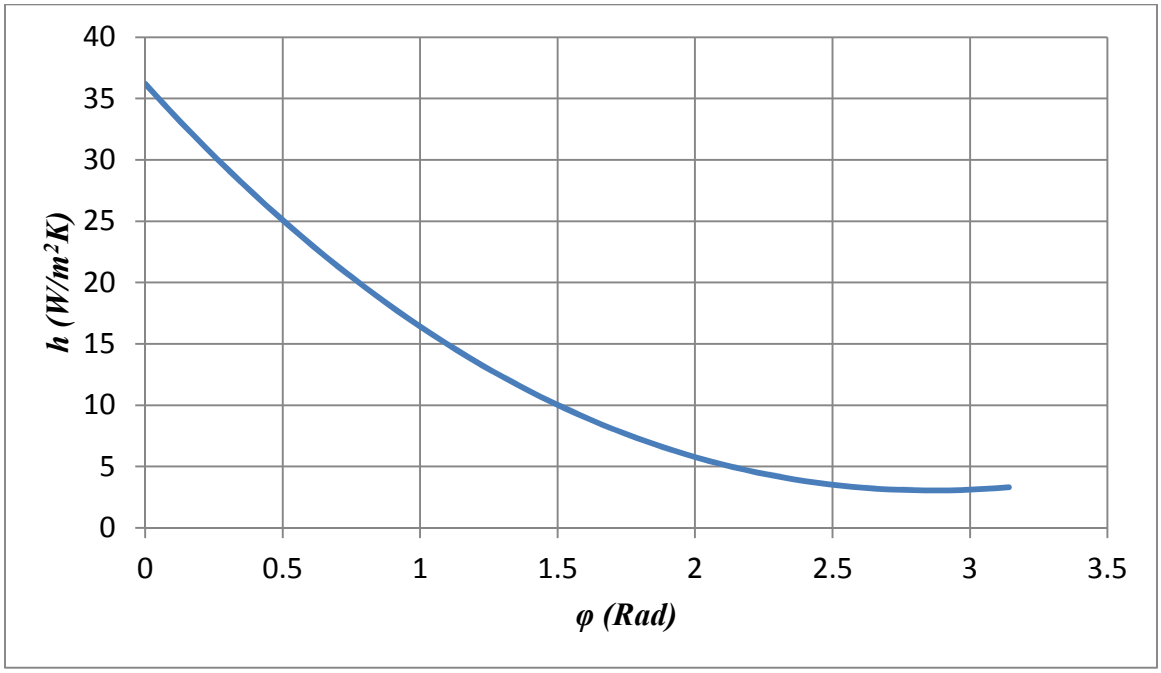

(a) Using air as HTF

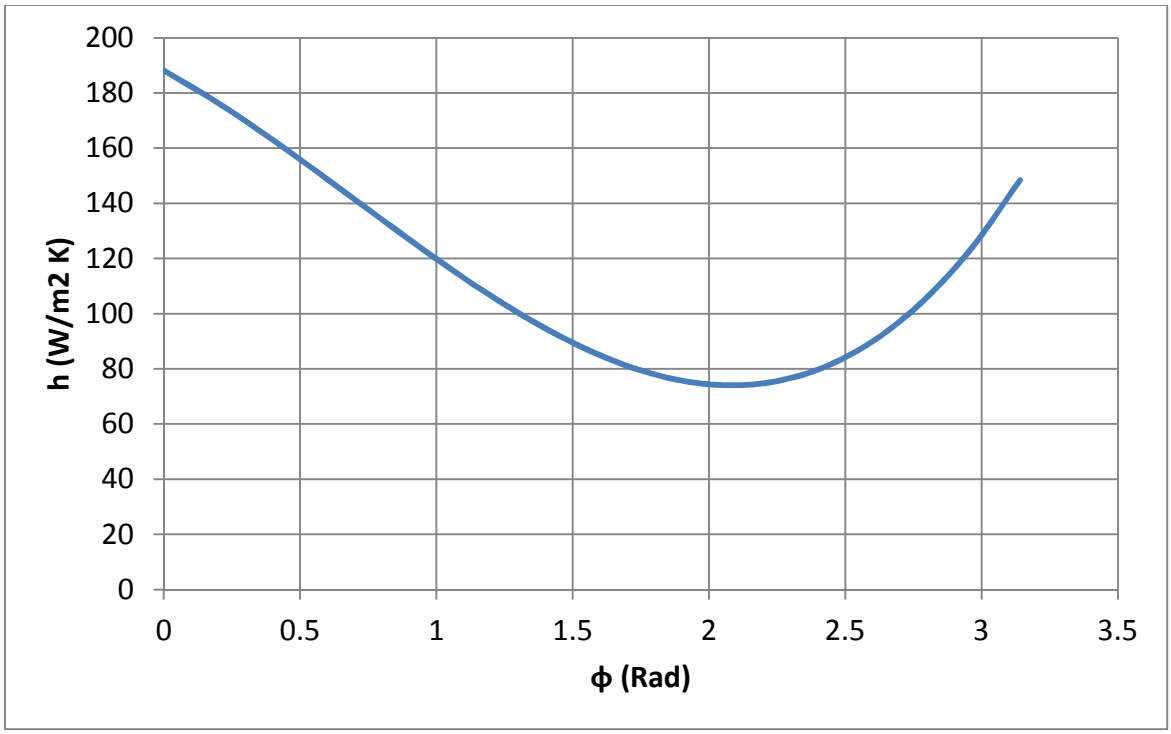

(b) Using liquid Therminol/VP-1 as HTF

Figure 7. Heat transfer coefficient along the surface of the capsule:(a) using air as HTF, and (b) using liquid Therminol/VP-1 as HTF.

3.3.2. Convergence test

The spatial and the temporal convergence of numerical method are established. Results of the spectral and the temporal convergences test are listed in Table 5 for an enthalpy - porosity method. The dimensionless time steps used for the spectral convergence are 0.00024. The temporal convergence test is conducted for 2922 nodes.

Table 5. Convergence test for a 76.2 mm diameter $NaNO_3$ capsule using Therminol/VP-1 as HTF fluid during the chraging process.

Spatial Convergence ($\Delta\tau$ = 0.00024)		Temporal Convergence (2922 nodes)	
Number of nodes	Melting times (Seconds)	Dimensionless time step, $\Delta\tau$	Melting times (Seconds)
170	2748	0.0006	2772
802	2766	0.00024	2772
2922	2772	0.00012	2772

3.3.3. Results and discussions:

3.3.3.1. Comparison between the enthalpy–porosity method and the front tracking method

Figure 8 depicts the location of the interface at various times during charging process predicted by the enthalpy – porosity and the front tracking methods for 76.2 mm diameter EPCM capsule using air as a heat transfer fluid. The $NaNO_3$ interface propagates radially inward as melting process progresses. The top side of the PCM melts faster since the heat transfer fluid flows from top to bottom. Heat transfer coefficient is larger at the top of the capsule, shown in figure 7. Figure 8(a) shows the location of the interface using enthalpy – porosity method. Figure 8(b) shows the location of the solid/liquid interface predicted by the front tracking method. The front tracking method captures the dynamic of interface between solid and liquid PCM in a charging and a discharging process at all times. The front tracking determines the sharp interface separating liquid PCM from the solid PCM. The solid/liquid interface predicted by both methods becomes asymmetric rapidly. This is due the variation of the heat transfer coefficient along the outer surface of

the capsule. The interface location predicted by these methods agrees very well, as indicated in figures 8(a) and 8(b)

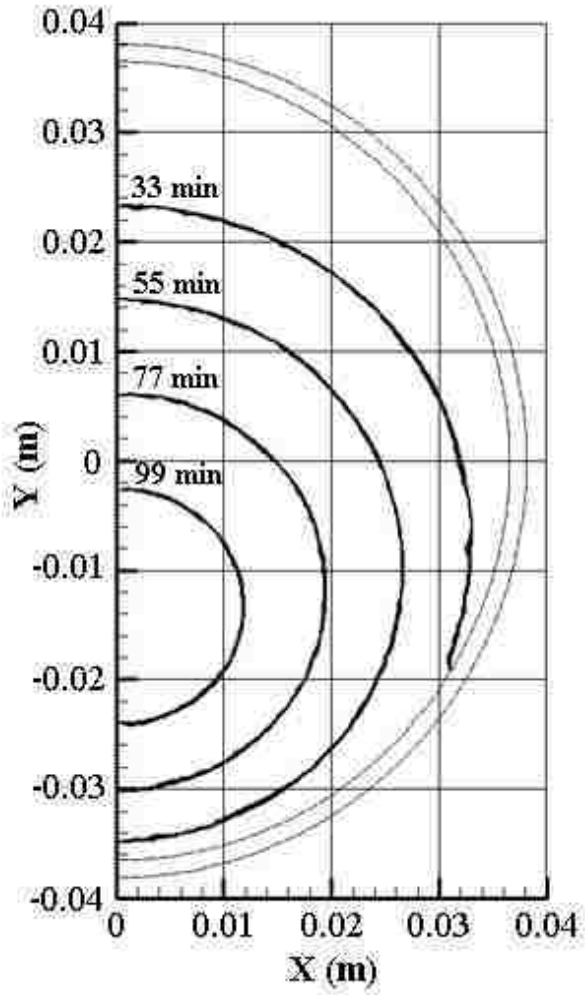

(a) the enthalpy – porosity method

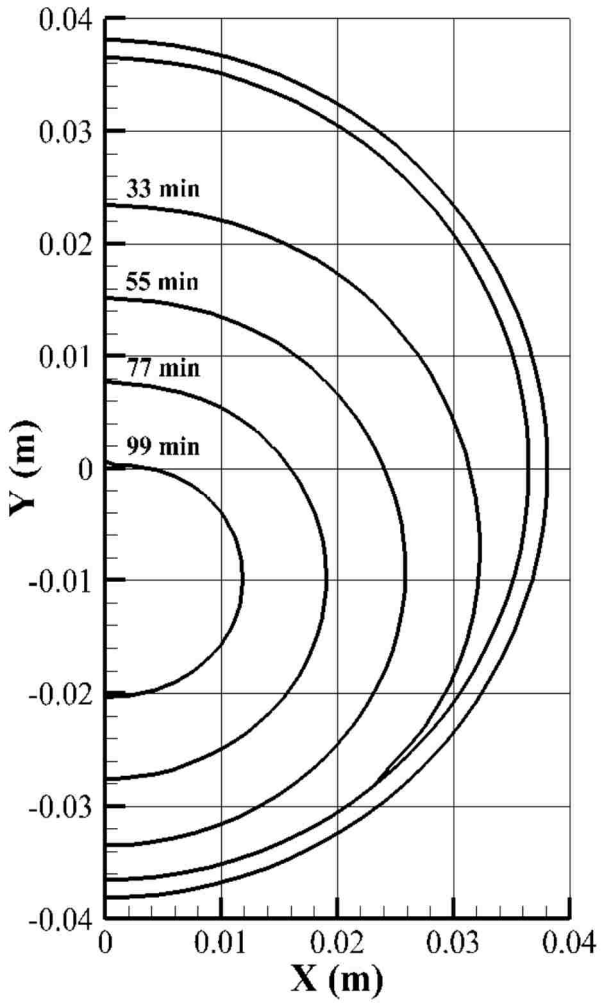

(b) the front tracking method (Results have done by Dr. W. Zhao at Lehigh University)

Figure 8. The location of the liquid/solid interface predicted a) by an enthalpy – porosity method and b) by a front tracking during a charging process.

3.3.3.2. Melting process of $NaNO_3$ as PCM

Figure 9 (a–f) show isotherms predicted by the enthalpy – porosity method at various times for 76.2 mm diameter EPCM capsule using air as a heat transfer fluid. Clearly, the

temperature in the upper part of the capsule is higher than that in the lower part and the isotherms are clearly radially asymmetric. The maximum temperature is reached at the top of the capsule. The temperature at the top is 583K which is greater than the melting temperature $NaNO_3$. Hence, the melting in the EPCM has started near the top of the capsule. As shown in figures 9 (c - f), the interface separating the liquid PCM from the solid PCM propagates radially inward as the melting process progresses. The temperature is much greater at the top. Temperature of the PCM increases in time. The maximum temperature is 595K at 10 minutes into the melting figure 9 (b) and increases to 675K at 77 minutes into the melting. The dark blue region represents the solid phase of the PMC where the temperature is below the melting temperature, 581K.

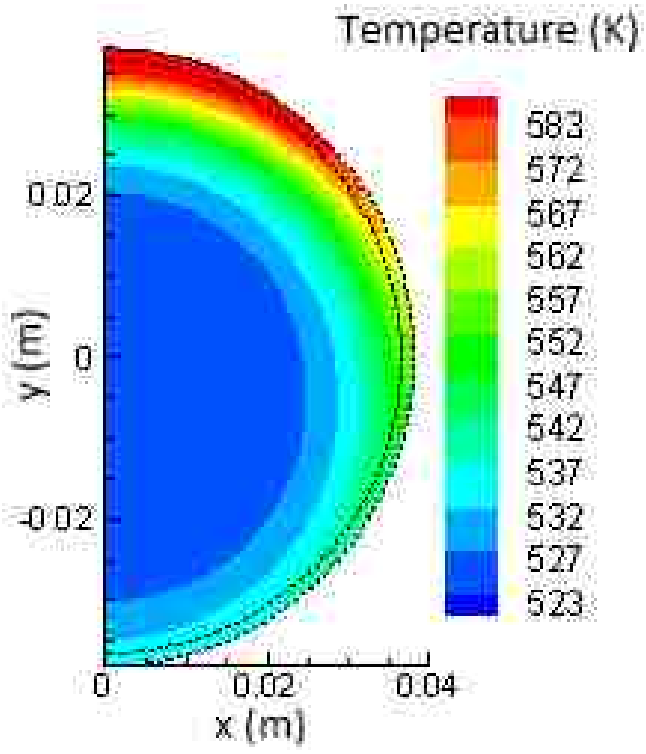

a) Melting process at 5 min

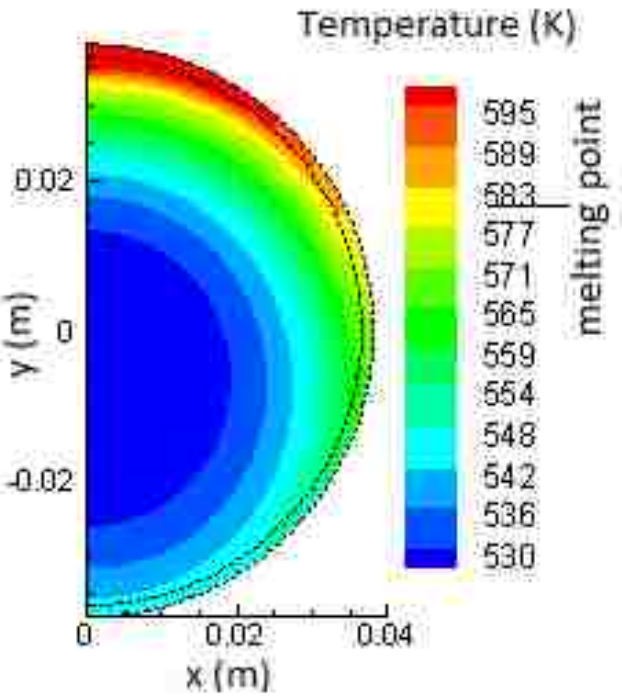

b) Melting process at10 minutes

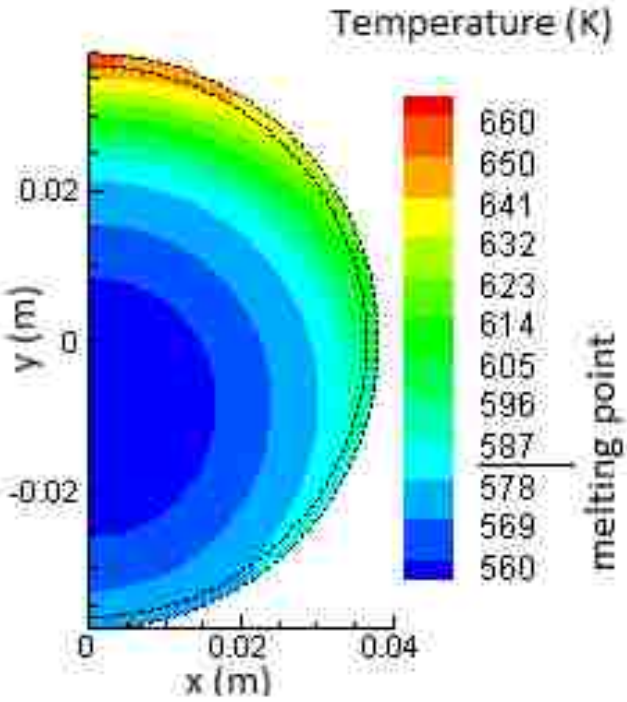

c) Melting process at 33 minutes

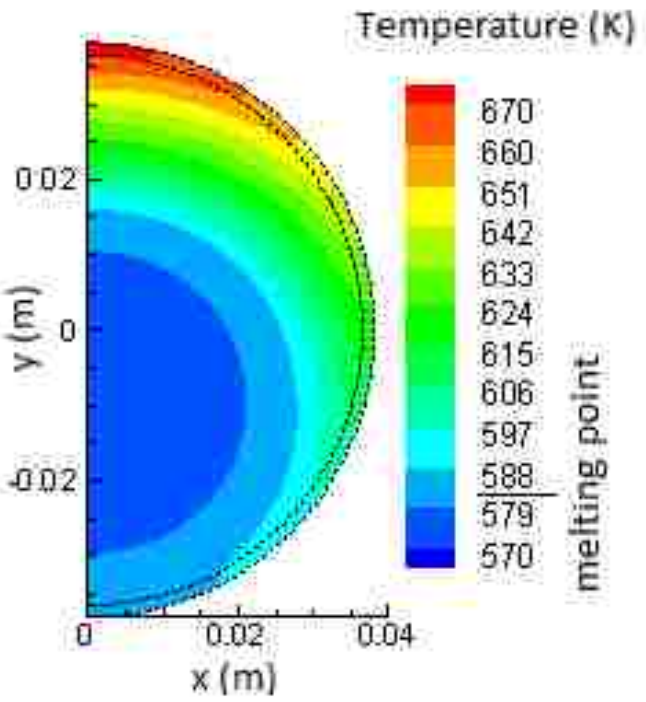

d) Melting process at 55 minutes

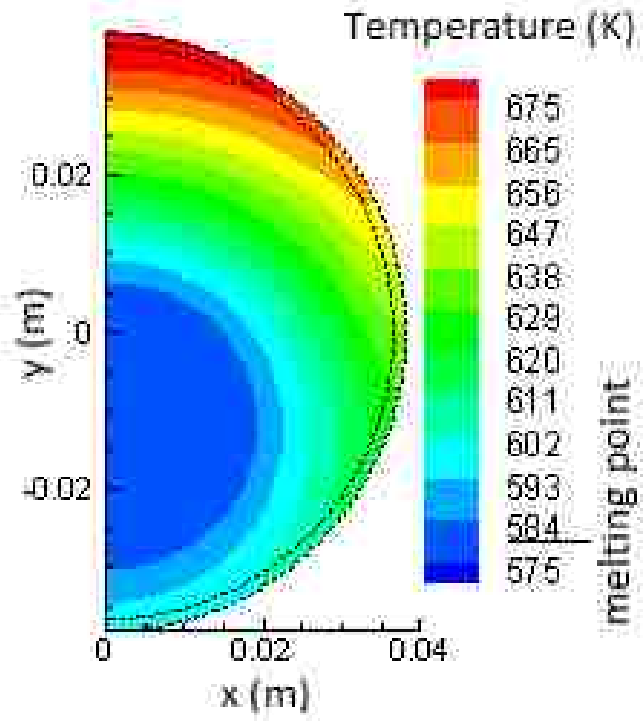

e) Melting process at 77 minutes

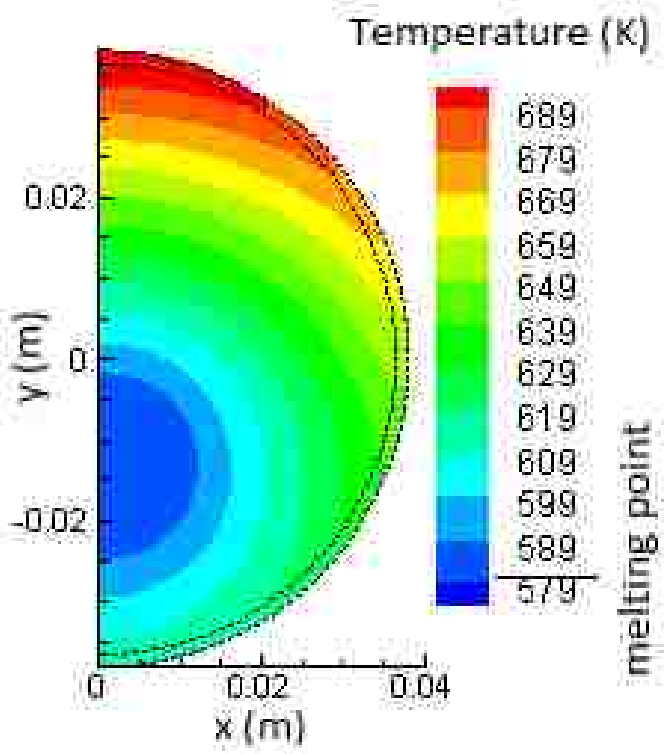

f) Melting process at 99 minutes

Figure 9 (a – f). Isotherms inside $NaNO_3$ capsule at various times during the charging process.

Figure 10 (a –f) show the location of the propagating liquid/solid interface at various times. Results are presented for a 76.2 mm diameter NaNO3 EPCM capsule during a charging process using air as HTF. The front propagates radially inward as the melting process progresses, as displayed in figure 10 (a-f). Here, the figure 10 (a) shows the interface formed near the top of the capsule at the early stage of the melting process. The melting front propagates faster at the top upper region of the capsule compared to the lower section. This is again attributed to the variations of the heat transfer coefficient along the capsule. At the late stage of the melting, the solid PCM is located near the bottom as shown in figure 10(f).

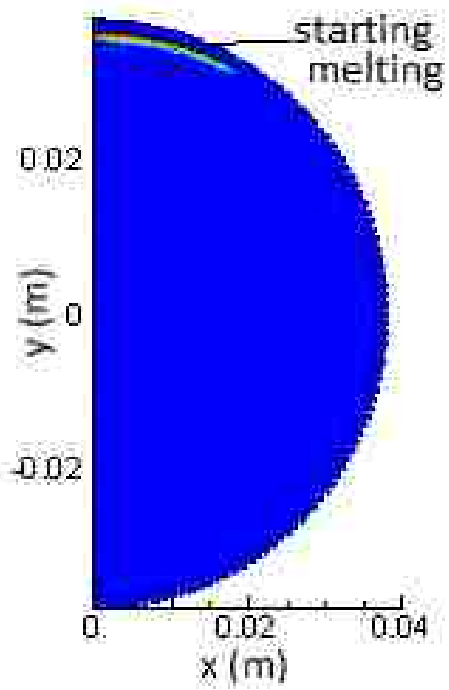

a) Propagating liquid/solid interface at 5 minutes

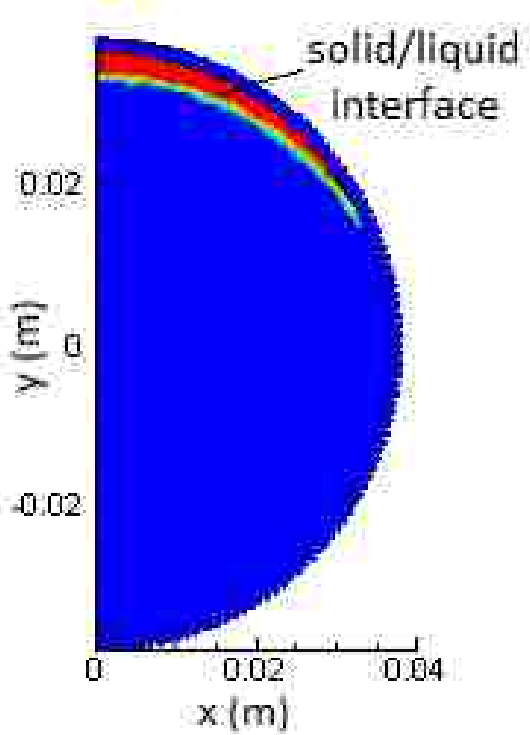

b) Propagating liquid/solid interface at 10 minutes

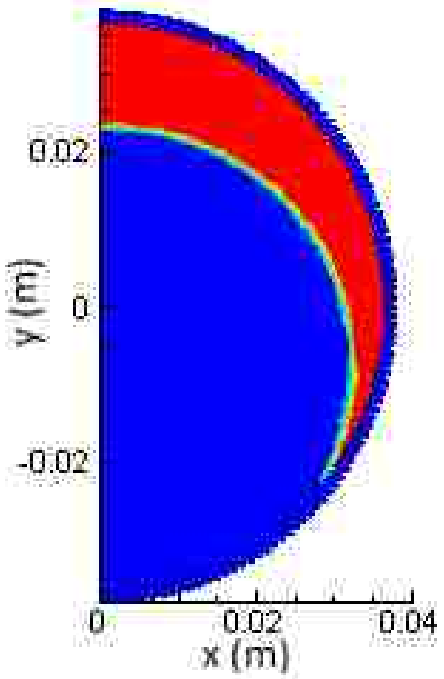

c) Propagating liquid/solid interface at 33 minutes

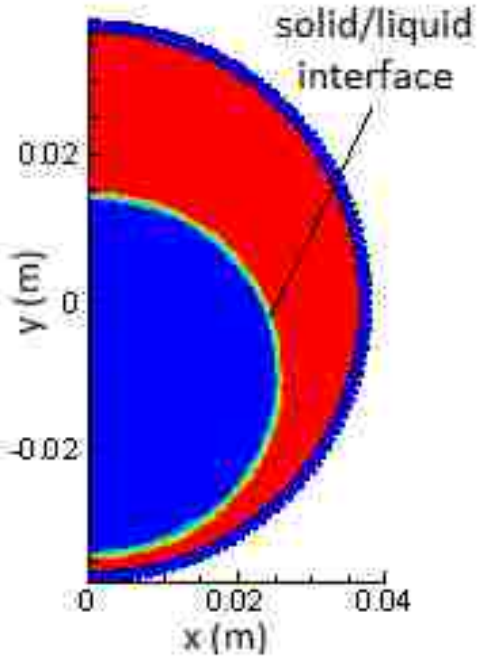

d) Propagating liquid/solid interface at 55 minutes

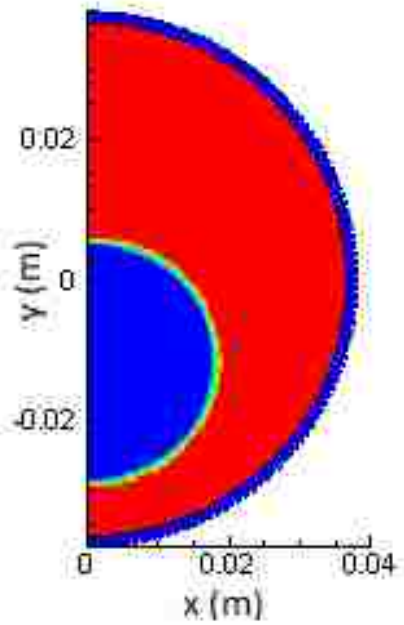

e) Propagating liquid/solid interface at 77 minutes

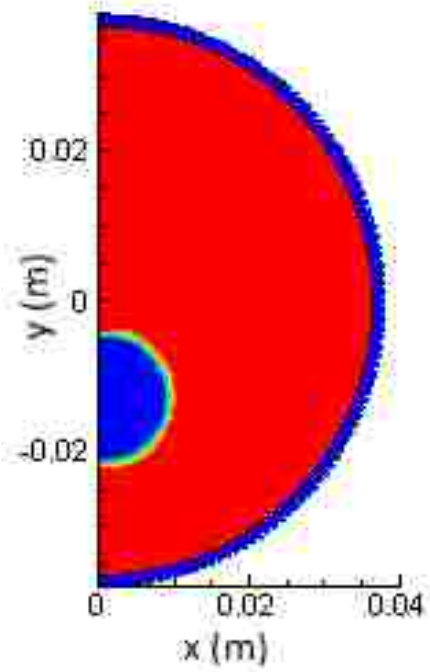

f) Propagating liquid/solid interface at 99 minutes

Figure 10. Locations of the solid/liquid interface in $NaNO_3$ capsule at various times during the melting process.

3.3.3.3. Solidification process in $NaNO_3$ EPCM

Figure 11(a – f) shows isotherms during the solidification process for the 76.2 mm diameter capsule using air as a heat transfer fluid. NaNO3 is encapsulated in a stainless steel capsule. The direction of the heat transfer fluid is from bottom to the top. Hence, the temperature of the upper part of the capsule is being higher than that in the lower part. The temperature at the bottom is 572K which is less than the freezing temperature of the NaNO3. Hence, the solidification in the EPCM has started at the bottom of the capsule.

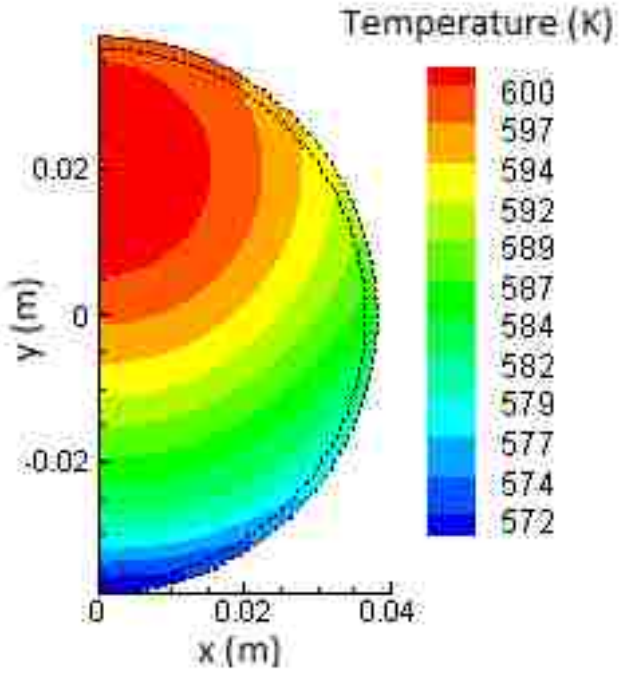

a) Solidification process at 3 hours

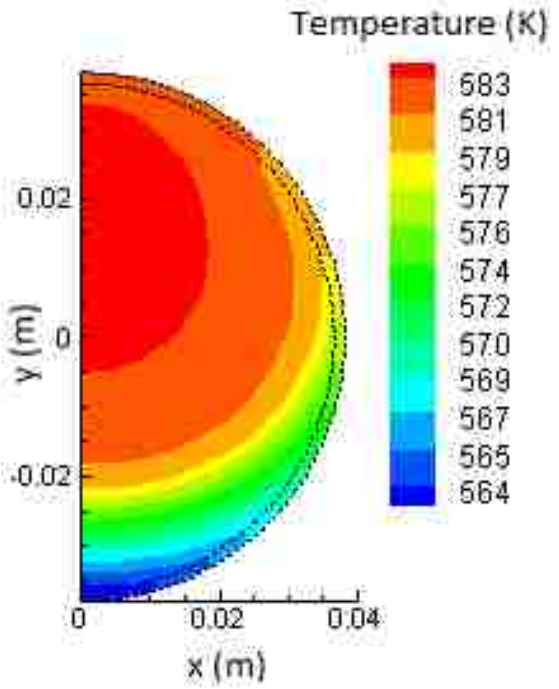

b) Solidification process at 4 hours

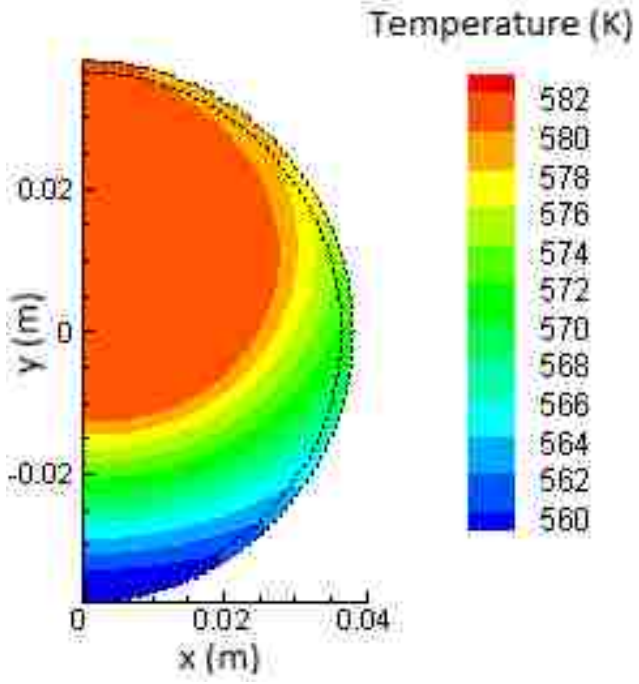

c) Solidification process at 5 hours

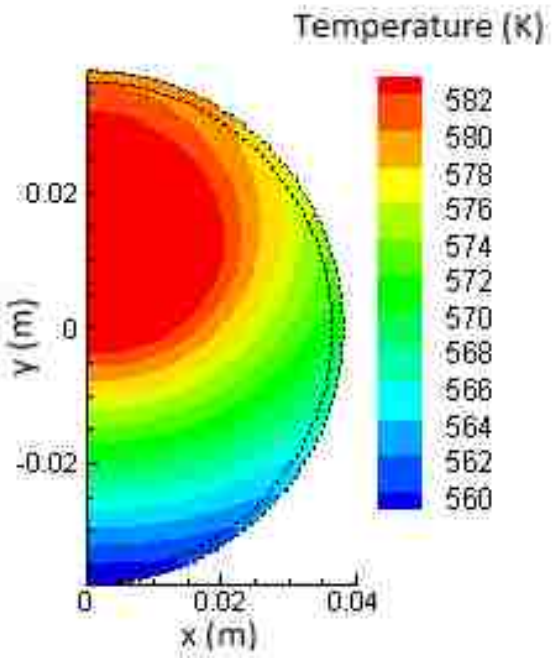

d) Solidification process at 6 hours

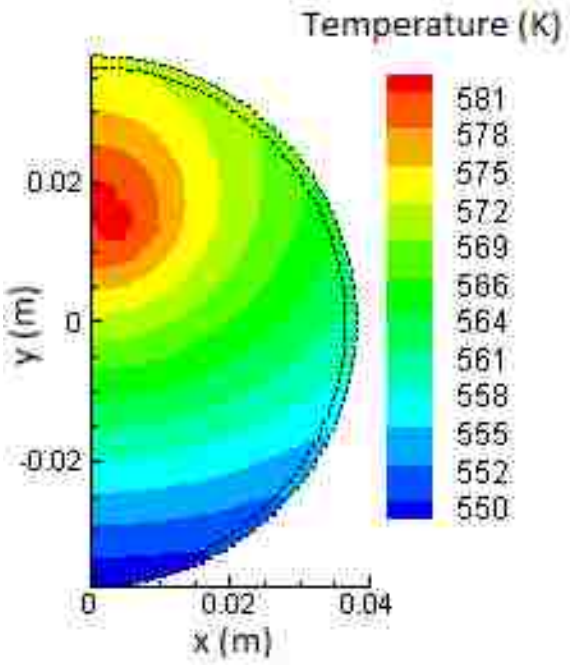

e) Solidification process at 8 hours

Figure 11 (a - e). Isotherms in $NaNO_3$ capsule at various times during the discharge process.

The location of the liquid/solid interface during a solidification process is shown in figure 12 (a-f). The liquid/solid interface propagates radially inward. Since the heat transfer fluid flows from the bottom to the top, the bottom region of PCM solidifies faster. Molten PCM region is located near the top at the late stages of the solidification process.

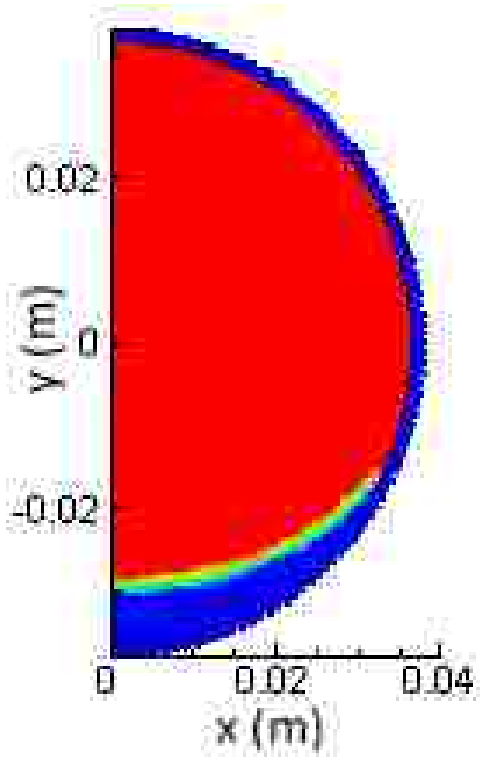

a) Solidification process at 3 hours

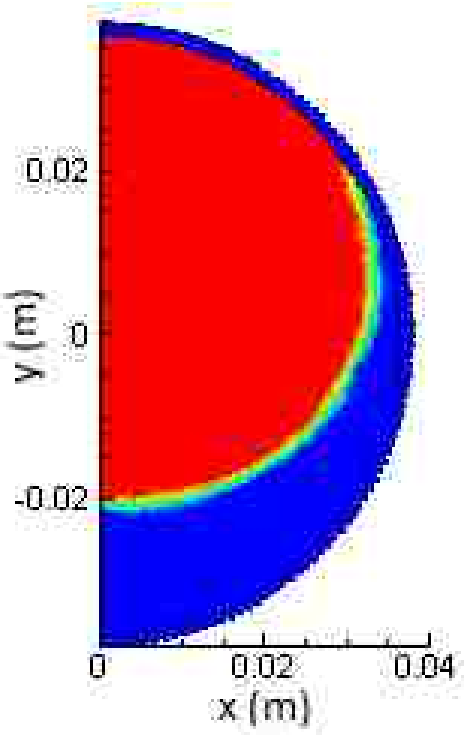

b) Solidification process at 4 hours

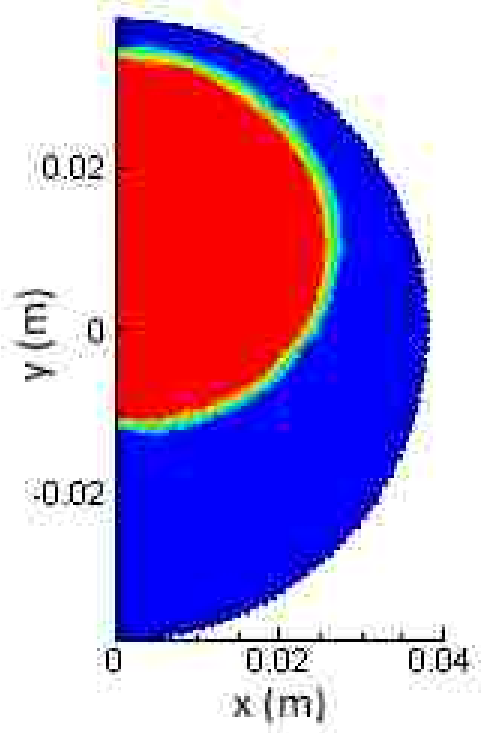

c) Solidification process at 5 hours

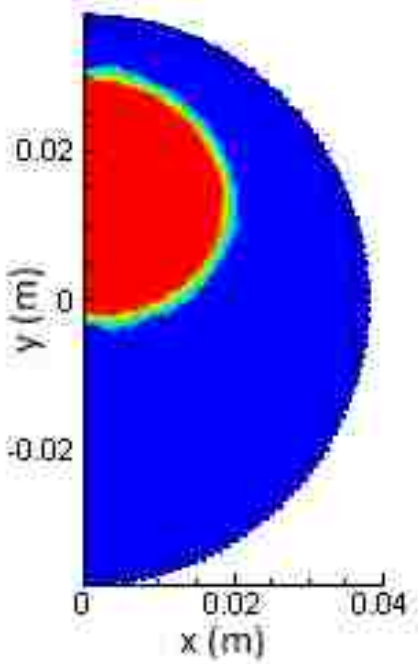

d) Solidification process at 6 hours

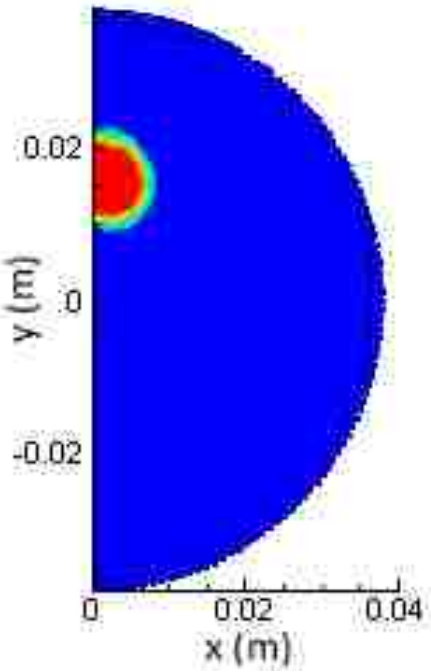

e) Solidification process at 8 hours

Figure 12 (a - e). The loaction of the solid/liquid interface in $NaNO_3$ capsule at various times during discharging process.

3.3.3.4. NaCl-$MgCl_2$ - Eutectic mixture

Figure 13 depicts the location of the interface at various times during charging process for a 76.2 mm diameter EPCM capsule using air as a HTF. The interface propagates radially inward as melting process progresses. The top side of the PCM melts faster since the heat transfer fluid flows from the top to the bottom. The solid/liquid interface is radially asymmetric due to the variation of heat transfer coefficient along the outer surface of the capsule. The solid region becomes very small in four hours after the melting process has started. The time it takes for melting process of NaCl-$MgCl_2$ is calculated to be nearly four hours and seven minutes for 76.2 mm diameter capsule, as displayed in figure 13.

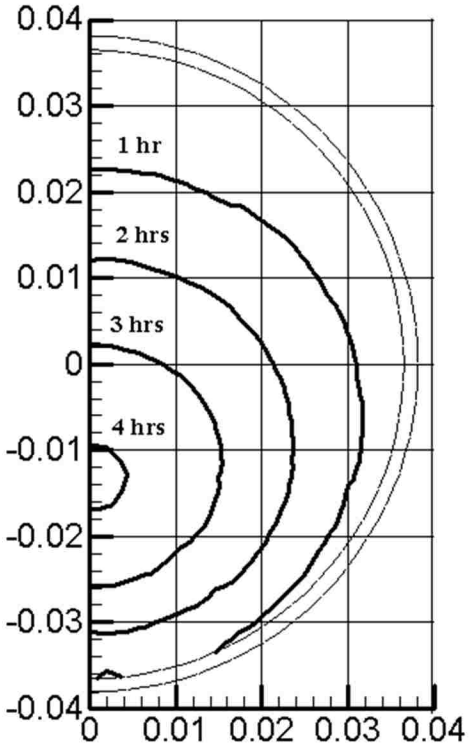

Figure 13. Interface location at various times during the melting process. Air is used as HTF.

Similarly, the location of the interface at various times during the melting process predicted for 76.2 mm diameter EPCM capsule is illustrated in figure 14 for Therminol/VP-1 as a HTF and NaCl-MgCl2 as PCM. The phase change process is much faster compared to that for air as a HTF since the rate of heat transfer at the surface of capsule is much higher.

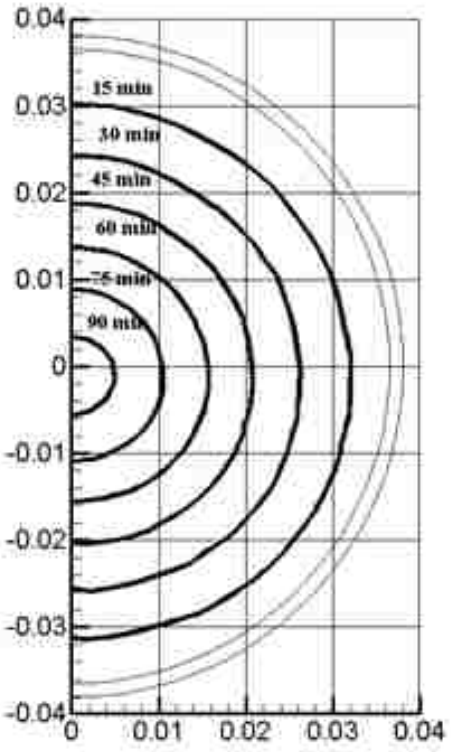

Figure 14. Interface location at various times during the melting process. Therminol/VP-1 is used as HTF.

Tables (6) – (9) illustrate the total heat transfer times of the energy storage and the retrieval for horizontally placed capsules of 25.4 mm and 76.2 mm diameter using air and liquid Therminol/VP-1 as HTFs. Obviously, the heat transfer time is much longer for larger size of capsule, and the liquid heat transfer fluid significantly shortens the heat transfer time in capsules.

Table 6. Energy storage times for 25.4 mm and 76.2 mm diameter NaCl-$MgCl_2$ eutectice capsule. Air is used as HTF.

Diameter of Capsule	Conduction Process Time (min)	Melting Process Time (min)	Total Charging Time (min)
1 inch (25.4 mm)	86.67	45	131.67
3 inches (76.2 mm)	310.0	288.33	598.33

Table 7. Energy storage times for 25.4 mm and 76.2 mm diameter NaCl-$MgCl_2$ eutectice capsule. Therminol/VP-1 is used as HTF.

Diameter of Capsule	Conduction Process Time (min)	Melting Process Time (min)	Total Charging Time (min)
1 inch (25.4 mm)	8	12	20
3 inches (76.2 mm)	48.2	83.17	180.0

Table 8. Energy retrieval times for 25.4 mm and 76.2 mm diameter NaCl-$MgCl_2$ eutectice capsule. Air is used as HTF.

Diameter of Capsule	Conduction Process Time (min)	Solidification Process Time (min)	Total Discharging Time (min)
1 inch (25.4 mm)	53.5	28.2	81.7
3 inches (76.2 mm)	238.8	221.6	460.4

Table 9. Energy retrieval times times for 25.4 mm and 76.2 mm diameter NaCl-$MgCl_2$ eutectice capsule. Therminol/VP-1 is used as HTF.

Diameter of Capsule	Conduction Proces Time (min)	Solidification Process Time (min)	Total Discharging Time (min)
1 inch (25.4 mm)	6.2	8.3	14.5
3 inches (76.2 mm)	46.4	72.5	118.9

3.5. Conclusions

The encapsulated phase change material studied is NaNO3 and the eutectic of NaCl and $MgCl_2$ encapsulated by a stainless steel. Transient two dimensional heat transfer analysis is performed using the enthalpy-porosity method. The interface dynamics, the temperature distribution and the time of energy storage and retrieval predicted by the enthalpy-porosity methods have been presented. Energy and retrieval predicted by the enthalpy – porosity method and the front-tracking method agree very well. The present study clearly proves that enthalpy methods are valuable tools to study the transport phenomena in phase changing systems. Results predicted by the transient heat transfer simulations conducted for paraffin wax n-octadecaneas a PCM using the enthalpy-porosity method agree well with previous experimental and numerical results reported in the literature. The heat transfer process inside the EPCM capsule is impacted by the sizes of capsules, types of heat transfer fluids. Storage/retrieval times into/out of EPCM are strongly influenced by the flow characteristics of HTF near EPCM. Storage of energy from a solar field is governed by the rate at which the energy can be brought to the EPCM by the heat transfer fluid and the discharging times will be governed by the rate at which the stored energy is used.

CHAPTER 4 – The Effects of Natural Convection and Void on the EPCM Storage

4.1. Motivation

The natural convection and the presence of void in encapsulated phase change materials could affect the charging – discharging process. The dynamics of the interface and the temperature profiles in EPCM will be influenced by the natural convection in the molten PCM and the presence of void in EPCM. Likewise, the thermal expansion and the volume expansion due to phase change would generate vortices that have different shape compare to capsule without void. The natural convection is expected to decrease melting/solidification time. In contract, the void is probable to reduce the rate of heat transfer from/into EPCM and then increased storage and retrieval time. Thermal analysis of high temperature phase change materials (PCM) is conducted with the consideration of buoyancy-driven convection with/without a 20% void in a stainless steel capsule. The effects of the thermal expansion and the volume expansion due to phase change on the energy storage and retrieval process are investigated as well.

Sodium nitrate is considered as potential PCM for simulation. The charging and discharging into and from the capsule wall is simulated for different boundary conditions and is applied with both laminar and turbulent flow conditions.

4.2. Mathematical model

A cylindrical shaped EPCM capsule or tube is considered in simulations using both Air and liquid, Therminol/VP-1, as the heat transfer fluid in a cross flow arrangement. Mathematical model based on the enthalpy – porosity meyhod. The buoyancy–driven

convection is modeled using Bousseinseq approximation. The volume of fluid, VOF, models multiphase flows of air and the molten PCM. Air in the void is modeled as an ideal gas. The computational domain in the PCM will be divided to different regions as shown in figure 15.

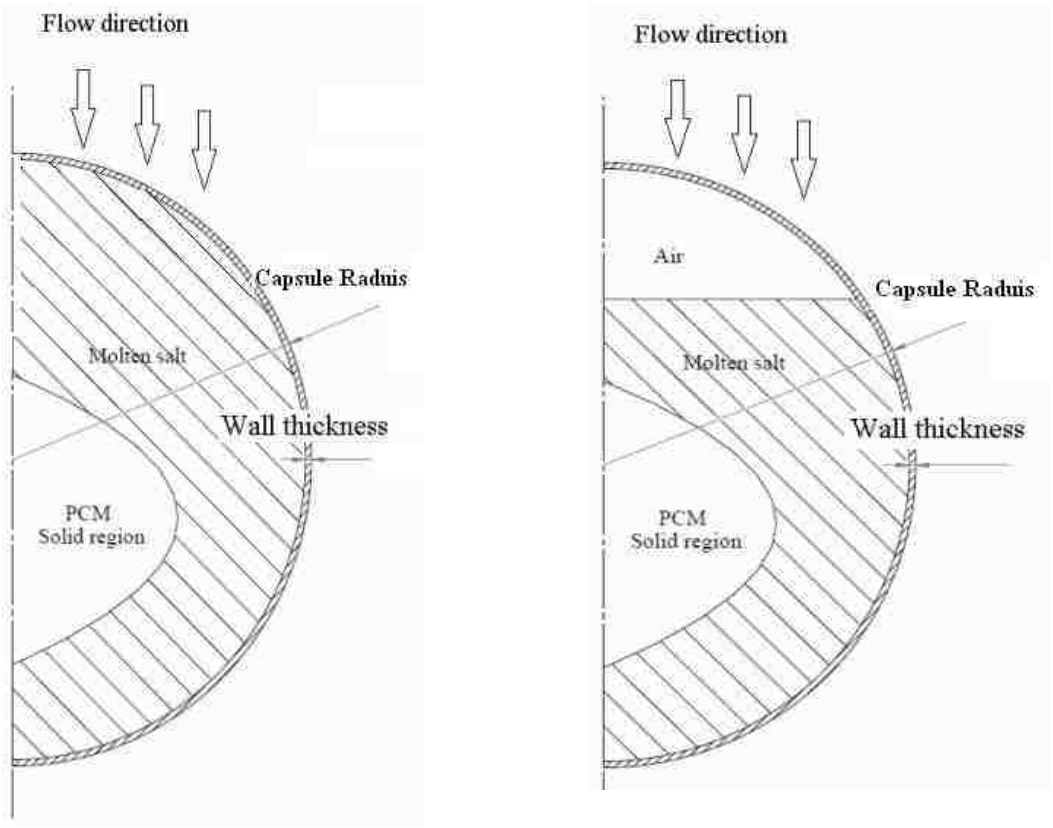

a) Without void **b) With void**

Figure 15. Schematic of the computational domain in an EPCM capsule

4.3. Boundary and initial conditions

A cross flow arrangement of the HTF around the capsule is considered. The temperature of the HTF is 773K for a charging process while it is 523K for a discharging process. The initial temperature of the capsule is at 523K for the charging process and 773K for a discharging process. The HTF flows from the top to the bottom of the cylinder during both the charging and discharging process. Based on the local Nusselt number, the heat transfer coefficients around the capsule is calculated using the correlations as described in chapter 3.

4.4. The effect of buoyancy-driven convection in the EPCM

The buoyancy-driven convection in the molten PCM is considered first without presence of void. According to Bossiness approximation, it is assumed that the density is constant except in the body force term of the momentum equation. There is no volume change in the PCM during the phase change process.

4.4.1. Validation of the computational model

Simulations are conducted for the paraffin wax n-octadecane as PCM. The melting point of the PCM is 28.2 $^{\circ}$C. The PCM is encapsulated by a glass [27] spherical capsule of 101.66 mm diameter. The density of n-octadecane is 772 kg/m^3; its kinematic viscosity is 5×10^{-6} m^2/s; the specific heat is 2,330 J/kg·K; thermal conductivity is 0.1505 W/m·K; its latent heat of fusion is 243.5 kJ/kg; the thermal expansion coefficient of molten n-octadecane is 0.00091 K^{-1} [27]. The initial capsule temperature is around 27 $^{\circ}$C while the

temperature of the surface of the sphere is maintained at 40 °C. Figure 16 illustrates the simulation results for the paraffin wax n-octadecane model as a PCM. The temperature contours and the streamlines in the EPCM during the phase change process are similar to those reported by Tan, F.L. et al. (2009) [27]. The present simulation predicts that it takes 91 minutes to complete the melting process for the 101.66 mm diameter paraffin wax n-octadecane in a spherical capsule. The reported value of the melting time is 90 minutes for the melting process. Our prediction of the melting time agrees well with that reported by Tan, F.L. et al. (2009) [27]. Thus, it proves that the mathematical model and numerical methods employed are valid.

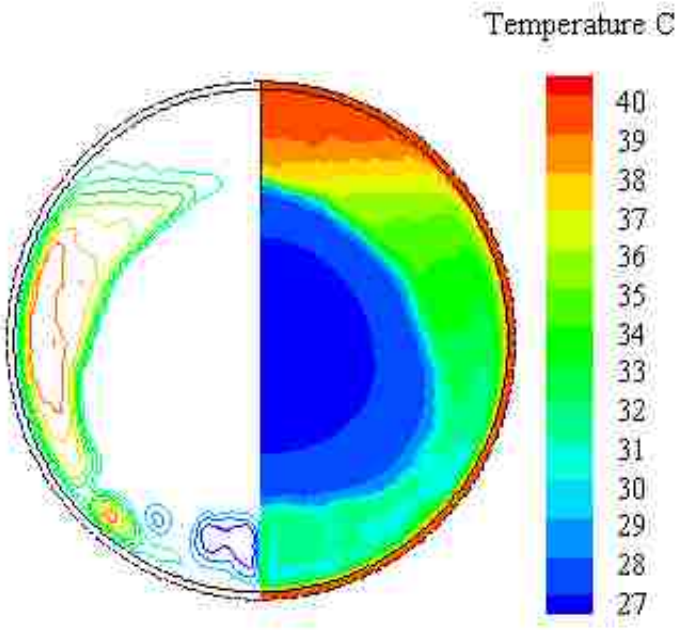

(a) 2400 sec

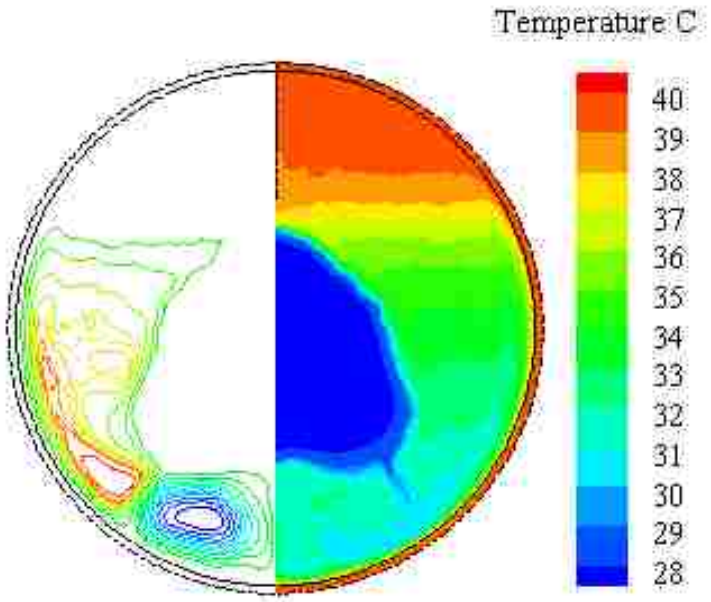

(b) 3600 sec

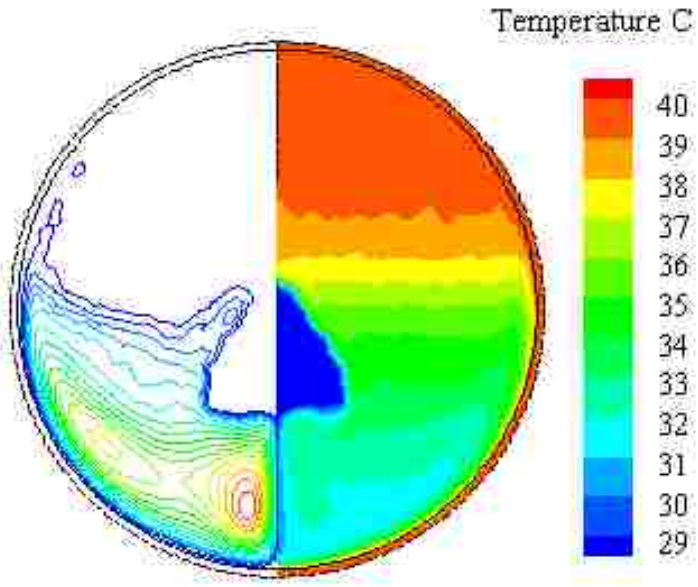

(c) 4800 sec

Figure 16. Isotherms and streamlines in the EPCM during the melting process Paraffin wax n-octadecane is used as PCM.

Many investigators have experimentally studied the phase change process for low melting PCMs. The present study focuses on the high melting temperature PCM (above 300 $^{\circ}$C). It is difficult to conduct experiment with high temperature EPCM capsule. So, an accurate thermal analysis is necessary to better understand energy storage using PCM.

4.4.2. Results and discussions

A 76.2 mm diameter cylinder is horizontally placed in the cross flow. Liquid VP-1 is used as the HTF. Figure 17 displays the liquid/solid interface movement in the EPCM during the melting process when considering the natural convection in the molten PCM. The interface is first formed near the encapsulation shell, and then moves inwards as shown in figure 17. The convection in the liquid phase affects the dynamics of the melting front.

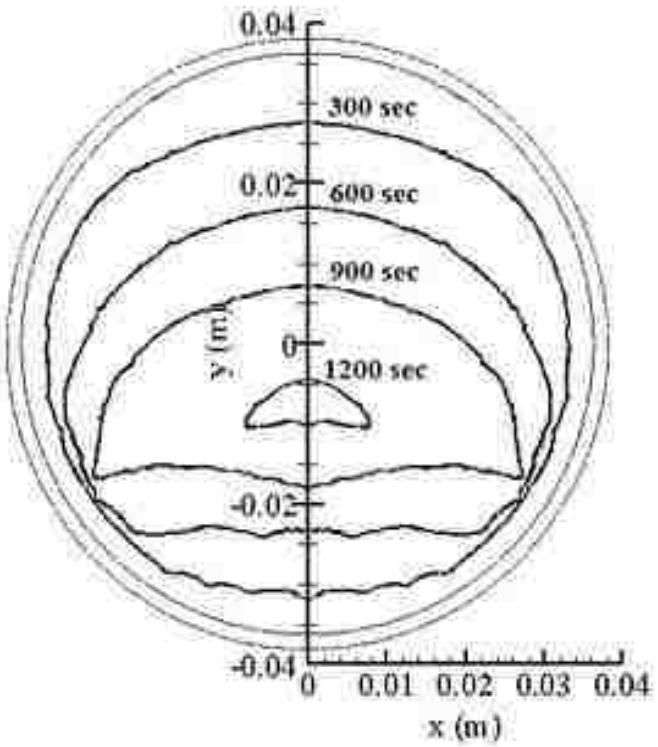

Figure 17. Location of the liquid/solid interface in $NaNO_3$ EPCM at various times during the melting process.

Figure18 (a - d) illustrate the temperature profiles and the streamlines in the EPCM capsule during the melting process. The temperature is higher at the top area of the cylinder since the highest local heat transfer coefficient occurs at the front stagnation point around the cylinder. The molten PCM temperature increases rapidly to HTF temperature while the temperature of solid PCM always maintains below the melting point of $NaNO_3$. The streamlines indicates the natural convection in the molten $NaNO_3$ during the melting process. At the early stage of melting process, the vortices are small as indicated in Figure 18 (a). As time goes on, the vortices at the bottom of the solid PCM become larger due to the temperature difference between the melting front and the

encapsulation shell. The vortices around the solid PCM would help to increase the melting rate of the solid $NaNO_3$, shorten the total phase change times.

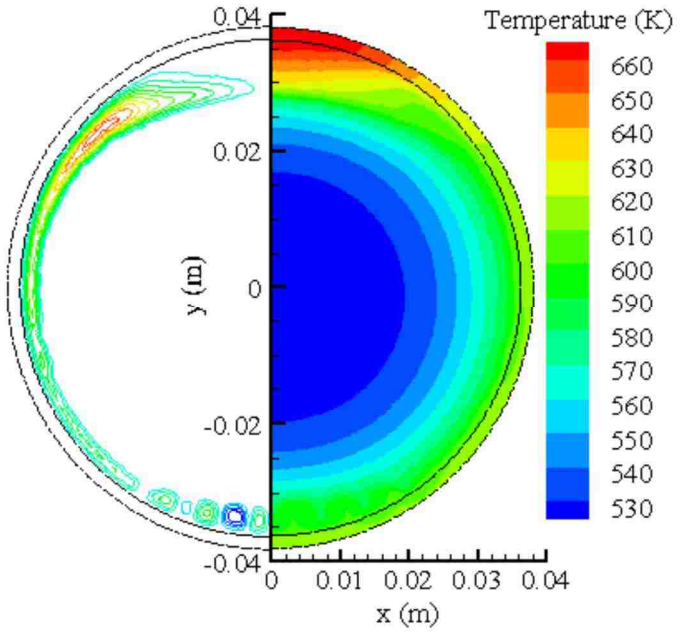

(a) 300 sec

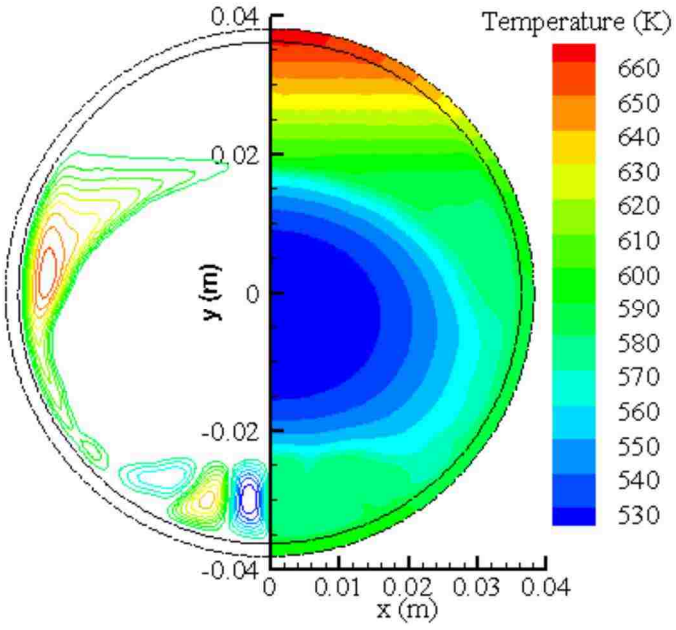

(b) 600 sec

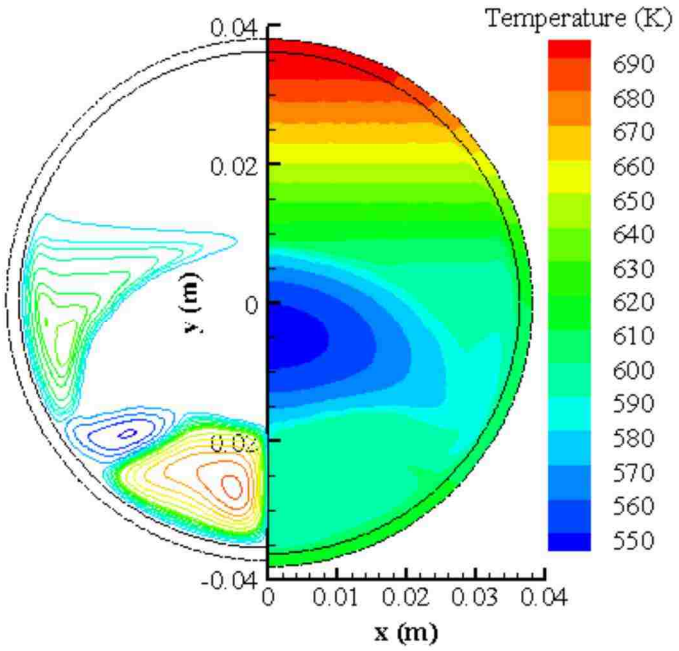

(c) 900 sec

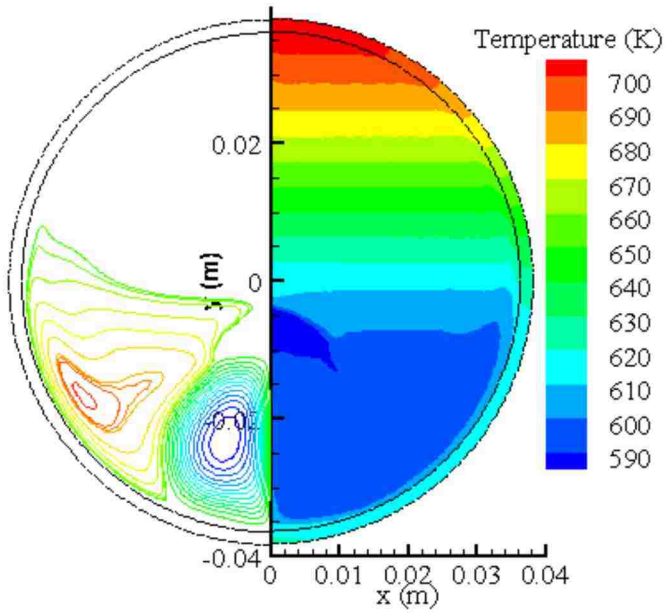

(d) 1200 sec

Figure 18. Isotherms and the streamlines in $NaNO_3$ EPCM at various times during the melting process.

For the current simulation, it is assumed that the density is the same for both liquid and solid PCM. However, the density of molten PCM would change when the phase change occurs, which causes the volume expansion of PCM in the capsule. Therefore, there must be certain void space inside the EPCM capsule for the volume expansion of the molten PCM. Furthermore, the solid PCM would sink to the bottom of the capsule due to its higher density comparing to the liquid phase. These effects will be discussed in the next section.

4.5. Thermal analysis of EPCM with void

A two dimensional transient simulation of a cylindrical capsule is presented for two capsule diameters, 25.4mm and 76.2mm, with both having a shell thickness of 1.5875 mm. Physical properties such as the specific heat, the thermal conductivity, the melting temperature, and the density of both materials are listed in Tables 2, 3, and 4 in chapter 3. The enthalpy – porosity and the VOF methods are applied to predict the charging and discharging process of the stainless steel-$NaNO_3$ EPCM capsules with an internal air void. The buoyancy – driven convection, the gravitational effects, and the variable density NaNO3 with thermal expansion during melting are considered as presented in the mathematical model as described in Chapter 2.

4.5.1. Validation of the computational model

In order to validate the present model and approach, numerical simulations are conducted for RT27_Rubitherm GmbH as the PCM and compared against the predicted and

measured results reported by Assis at el [53] using the same properties and boundary conditions mentioned in the documented in the same reference. A spherical shaped plastic EPCM of 40 mm in diameter is used. As the PCM does not have a constant melting temperature, therefore a melting interval is used, with the solidus and liquids temperatures set at 28°C and 30°C, respectively. In the simulation, the initial temperature of the computational model is 32°C, however, the boundary condition is a specific temperature of 15°C.

Figure 19 (a) and (b) depict the location of the liquid/solid interface at various times. The interface locations are predicated by using the present methods of enthalpy – porosity and volume of fraction simultaneously. These results are similar to the experimental results reported. It is shown that the solidification process at various times agree wells with reported results [53], as shown in figures 19 (a) and (b) The agreement between the numerical model and the reported results proves that both the models and numerical methods used in the present study are accurately predicting the heat transfer and the phase change processes in an EPCM capsule.

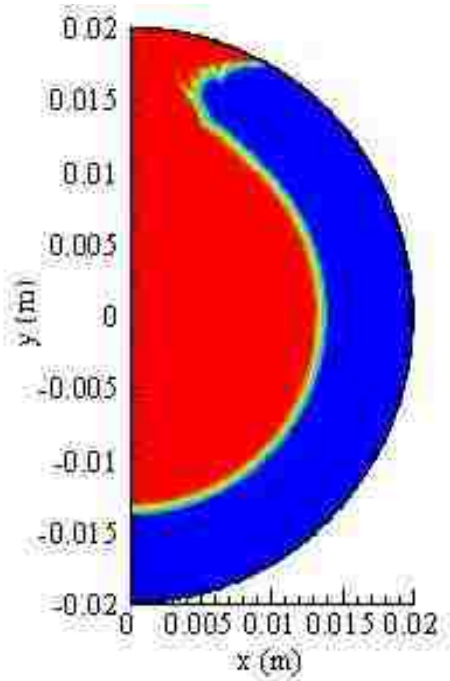

a) 600 sec

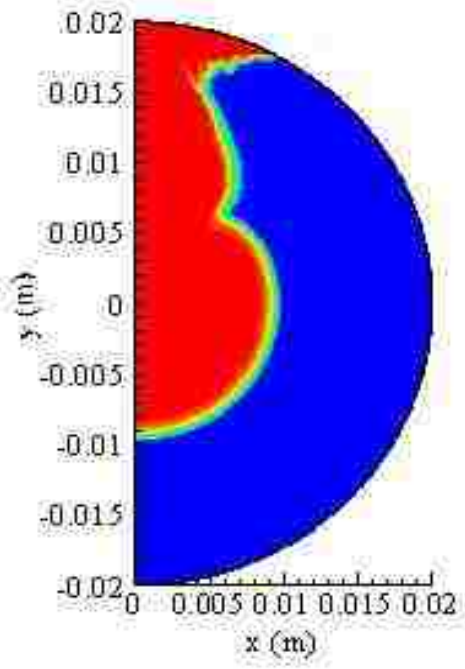

b) 1500 sec

Figure 19. The location of the solid/liquid interface at a) t = 600 sec and b) t = 1500 sec

4.5.2. Convergence test

The spatial and the temporal convergence test is conducted. Figure 20 (a-c) depicts the spatial convergence of the solid/liquid interface at the same time instant for a 25.4 mm capsule $NaNO_3$ - PCM with a 773K uniform temperature boundary condition and a 523K initial temperature for a varying number of nodes: 2290, 4276 (chosen), and 8736. The co-centered blue region is solid zone; molten salt is referred to by the red color, and the blue boundary refers to the stainless steel shell. Furthermore, the total melting time for all three cases is the same; 49.5 seconds with time step 0.02 sec.

Simulation results with the 4276 node using time steps of 0.01, 0.02, and 0.03 show insignificant differences, implying that time step of 0.01 is sufficient to satisfy the temporal convergence for the system.

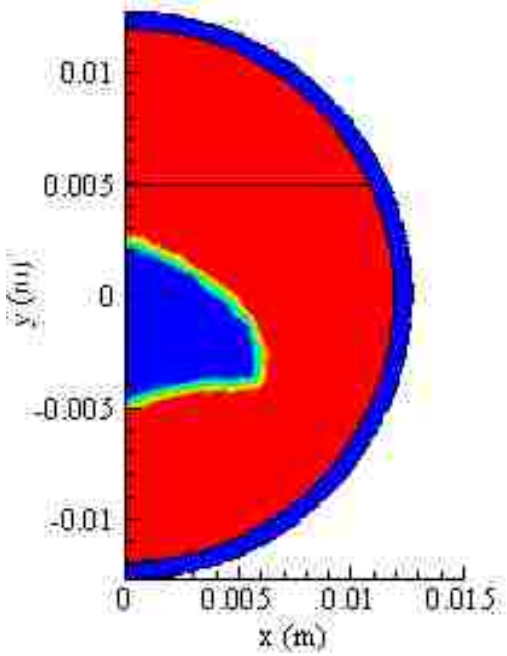

a) 2290 nodes

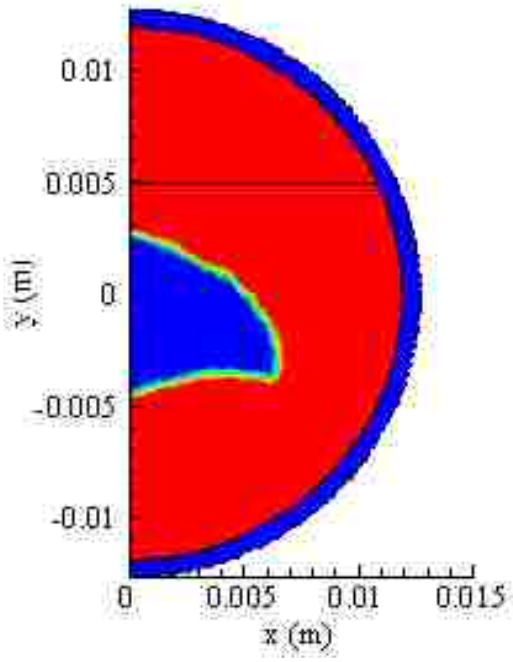

b) 4276 nodes

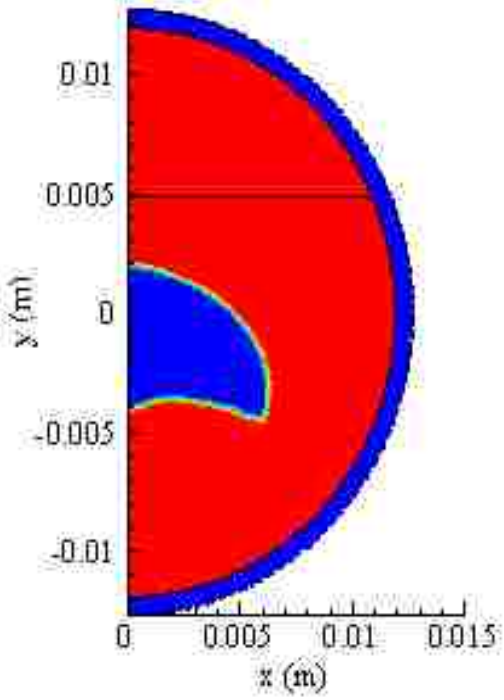

c) 8736 nodes

Figure 20. The location of the liquid/solid interface with 20% void. Simulations are conducted with a) 2290 nodes, b) 4276 nodes, and c) 8736 nodes.

4.5.3. Results and discussions

First, the results of two dimensional heat transfer analysis for a diameter 25.4 mm are presented. Figure 21 (a-d) shows the instantaneous contours of the velocity magnitude and the temperature distributions for a 25.4 mm cylindrical capsule with two different heat transfer fluids, air and VP-1. The right half of the EPCM capsule represents the temperature contours and the left side represents the velocity magnitude. Although the rate of heat transfer is smaller at the top of the EPCM capsule, the temperature gradient is larger compared to the rest the PCM. The poor thermal conductivity of the air at the top (void region) reduces the rate of heat transfer, as shown in figure 21 (a) and (b).

The temperature of the molten $NaNO_3$ salt increases rapidly as the melting process progresses, while the temperature of solid $NaNO_3$ remains nearly constant. The velocity magnitudes are very low in both the air and the molten PCM; however, it still affects the melting process. The rate of heat transfer has a significant influence on the temperature and velocity contours during the melting process. The higher rate of heat transfer with VP-1 as the HTF enhances buoyancy – driven convection which creates small vortices at the bottom of the solid PCM and accelerates the temperature reaching the melting point in a shorter time as compared to with air as the HTF. These results are illustrated in figure 21 (c - d).

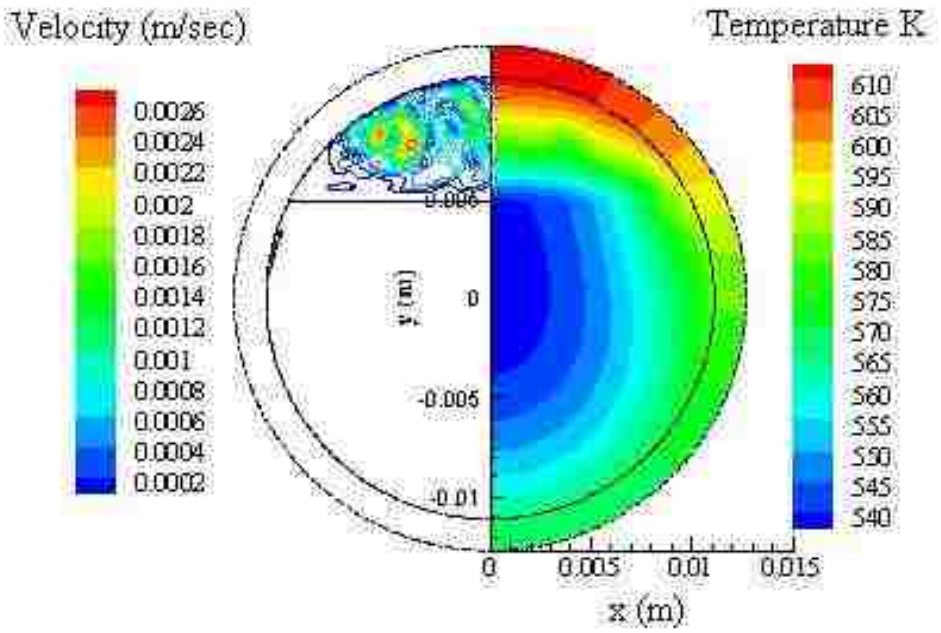

(a) Air as HTF (Re = 1230) at 200 s

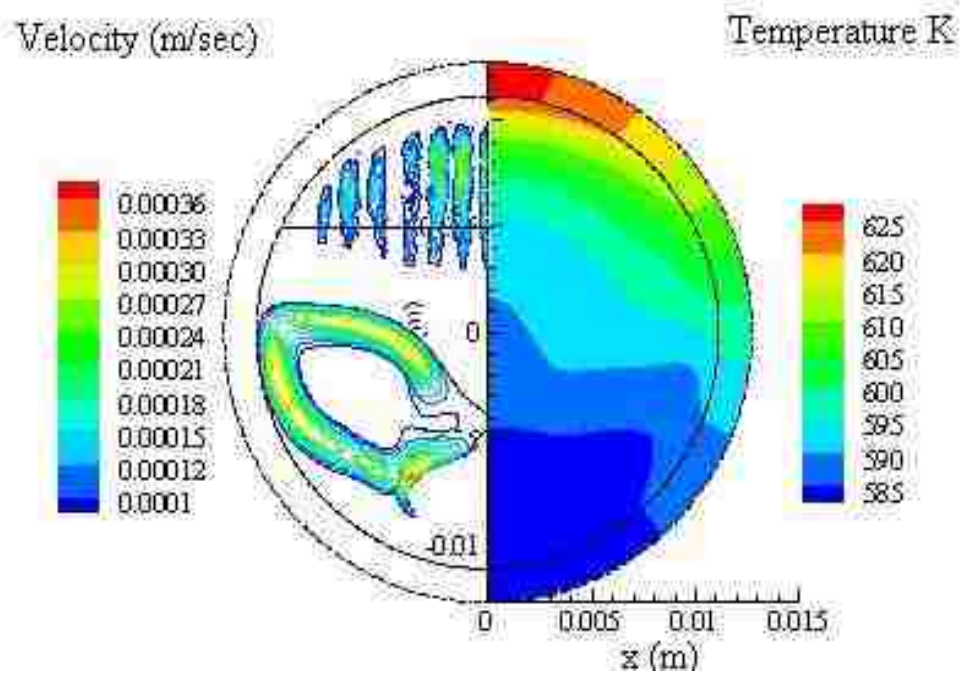

(b) Air as HTF (Re = 1230) at 3600 s

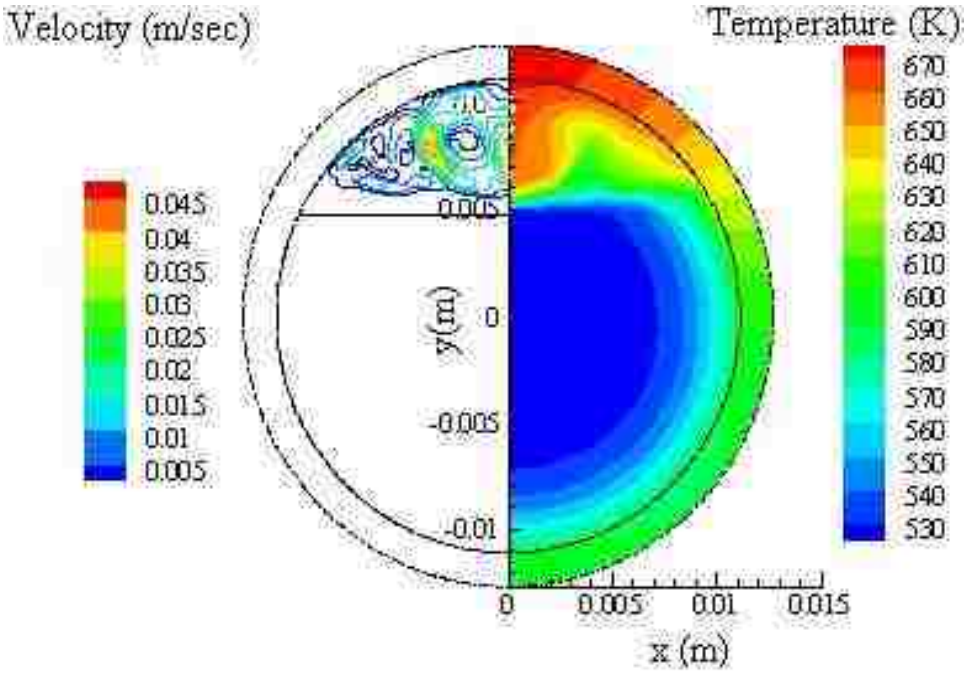

(c) VP-1 as HTF (Re=29,752) at 25 s

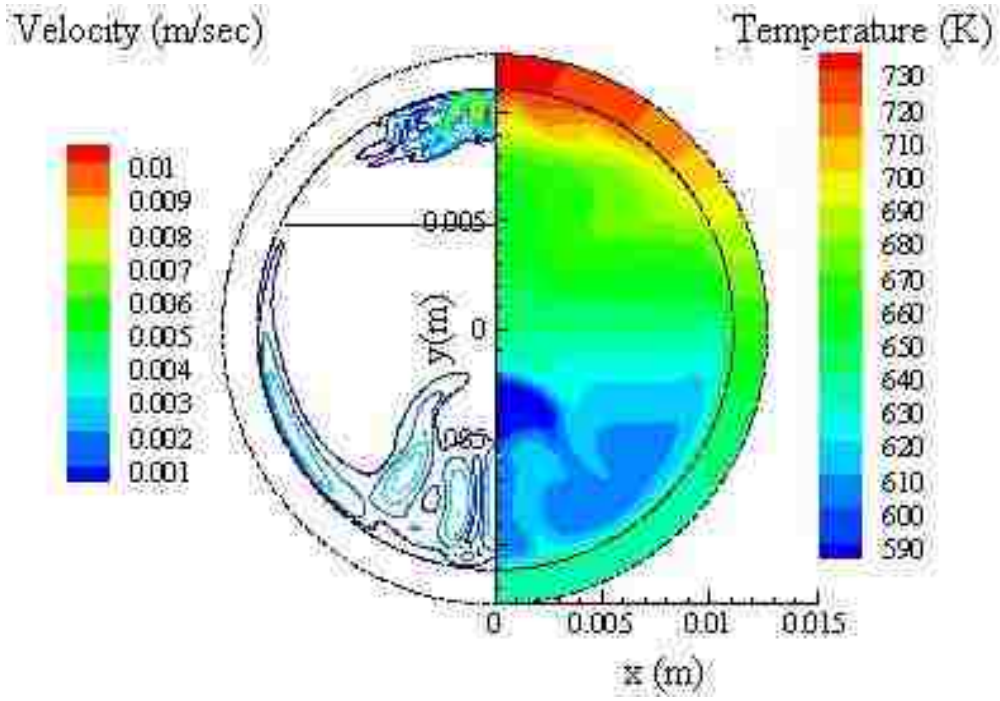

(d) VP-1 as HTF (Re=29,752) at 180 s

Figure 21. The isotherms and the contours of the velocity magnitude in the $NaNO_3$ EPCM with 20% void.

Figure 22 (a) – (g) shows the location of the liquid/solid interface at various times. The liquid/solid interface is shown on the left side for a 25.4 mm cylindrical EPCM capsule while density variations are shown on the right side. The location of the liquid/solid interface and the interface separating air from PCM are identified by the density of each phase. During the charging process, the volume expansion due to phase change and the thermal expansion of the salt drive the molten salt region to occupy 20% of the initial void space. The air becomes compressed at the top of the capsule.

As shown in figure 22 (b), and 22(f), the solid PCM region is shaped with regard to the rate of the surface heat transfer. Additionally, figure. 22 (c) shows that buoyancy – driven convection with air as the HTF is not strong enough to create clear vortices at the bottom of the capsule and the solid PCM is sinking close to the bottom wall of the capsule. In contrast, with VP-1 as the HTF the solid PCM is bounced up as shown in figure 22 (g) due to the increased heat transfer enhancing the vortices to increase the melting process at the bottom of the PCM.

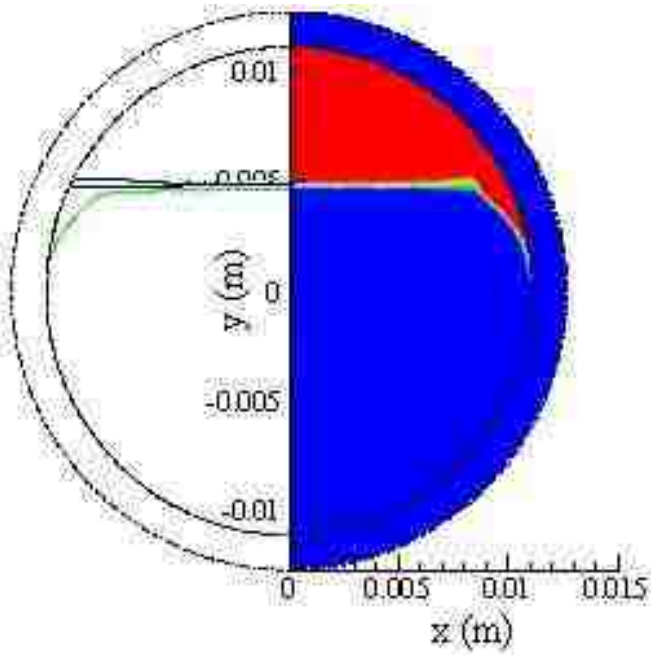

(a) t =200s (19% void) for air as HTF

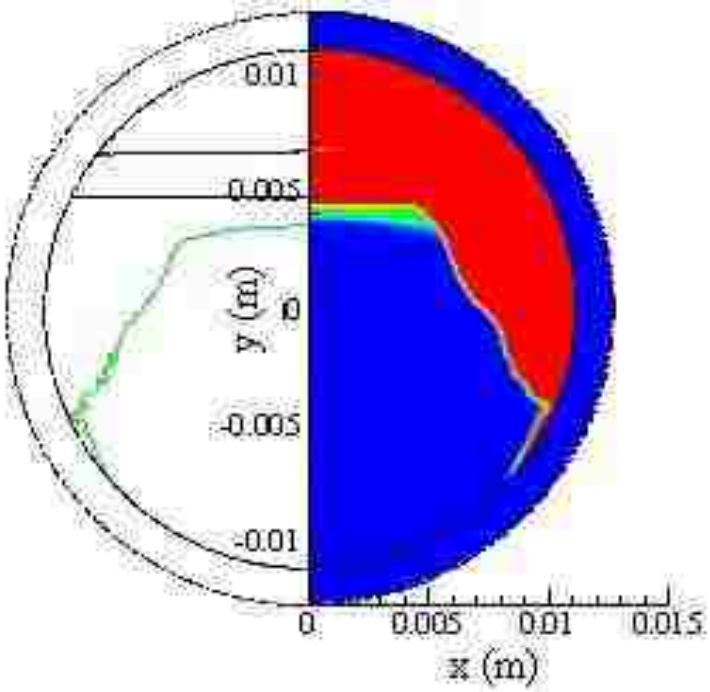

(b) t = 1200s (10% void) for air as HTF

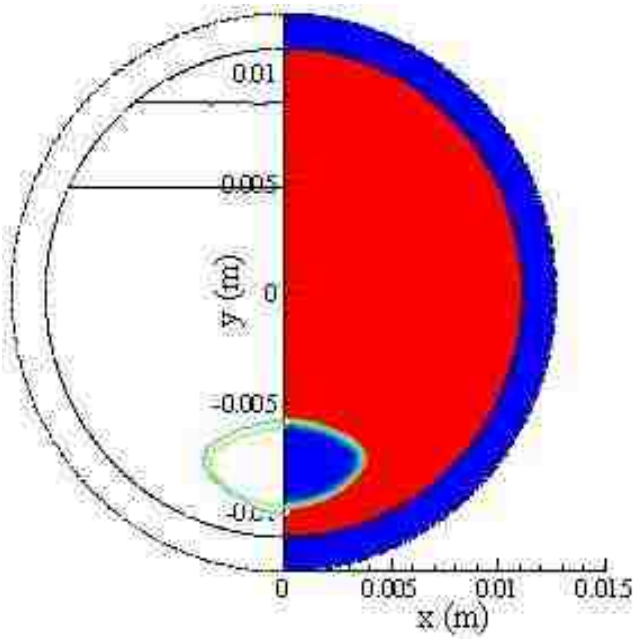

(c) t = 3600s (7% void) for air as HTF

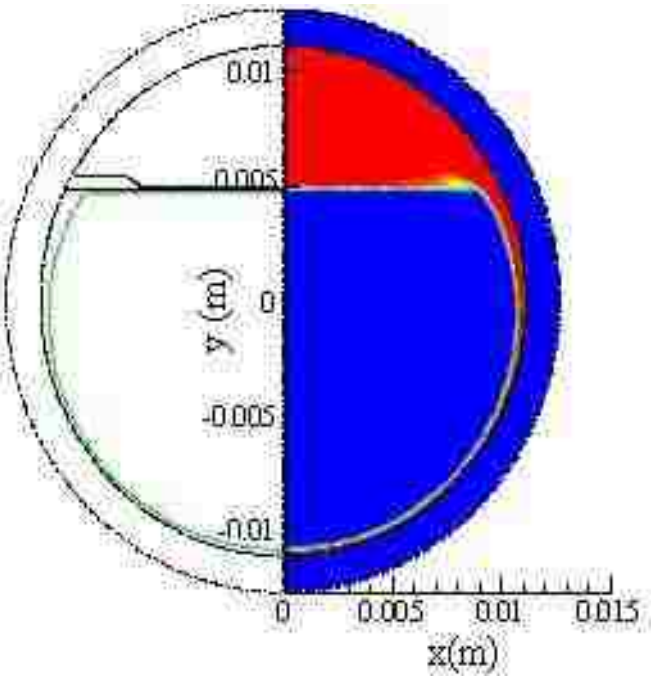

(d) t = 25s (19% void) for VP-1 as HTF

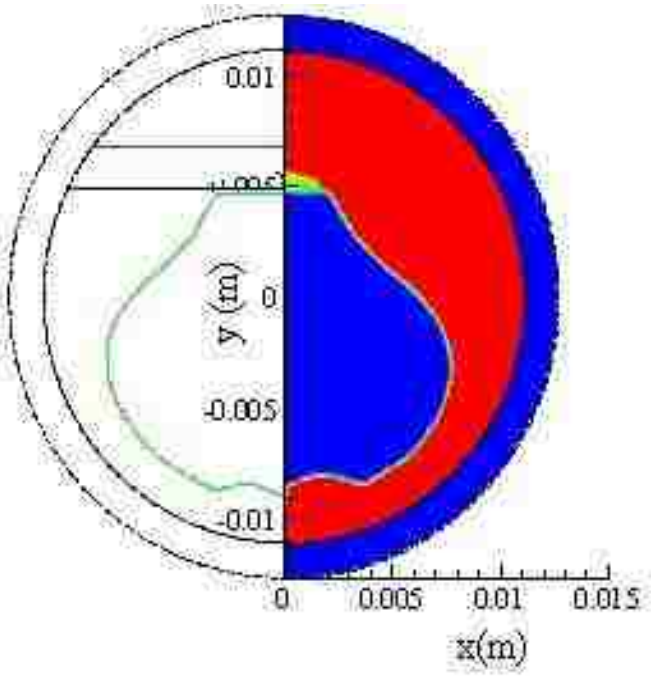

(f) t = 95s (10% void) for VP-1 as HTF

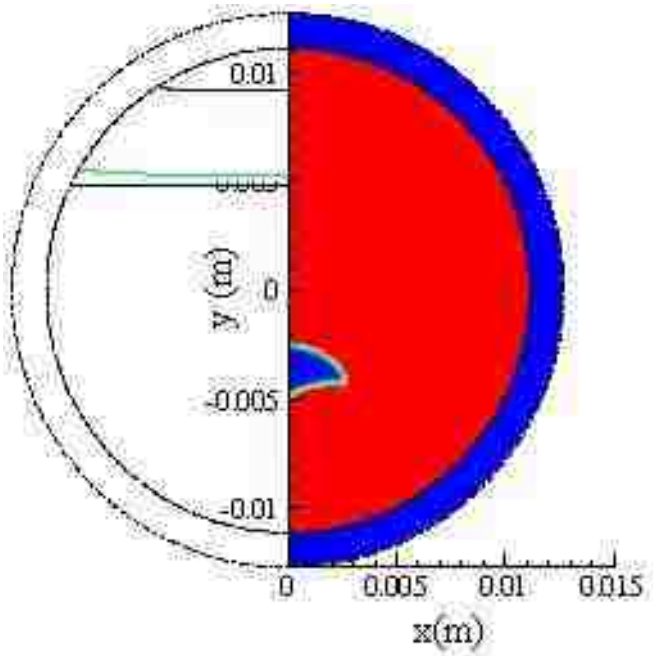

(g) t = 182s (5% void) for VP-1 as HTF

Figure 22. Density distribution and the location of the liquid/solid interfaces in $NaNO_3$ EPCM with 20% initial void.

Figure 23 (a-c) shows that temperature distributions and velocity magnitudes in the 76.2 mm NaNO3 EPCM capsule are similar to that of a 25.4mm capsule. The intensity of eddies formed near the bottom of the capsule are greater and the characteristics of the flow in the molten salt is different in the larger size capsule. Small vortices at the bottom of the solid PCM are formed at the early stage and they become larger as melting progresses and assist to increase re-circulation of the molten salt to accelerate propagation of the solid/liquid front, as shown in figure 23 (a)

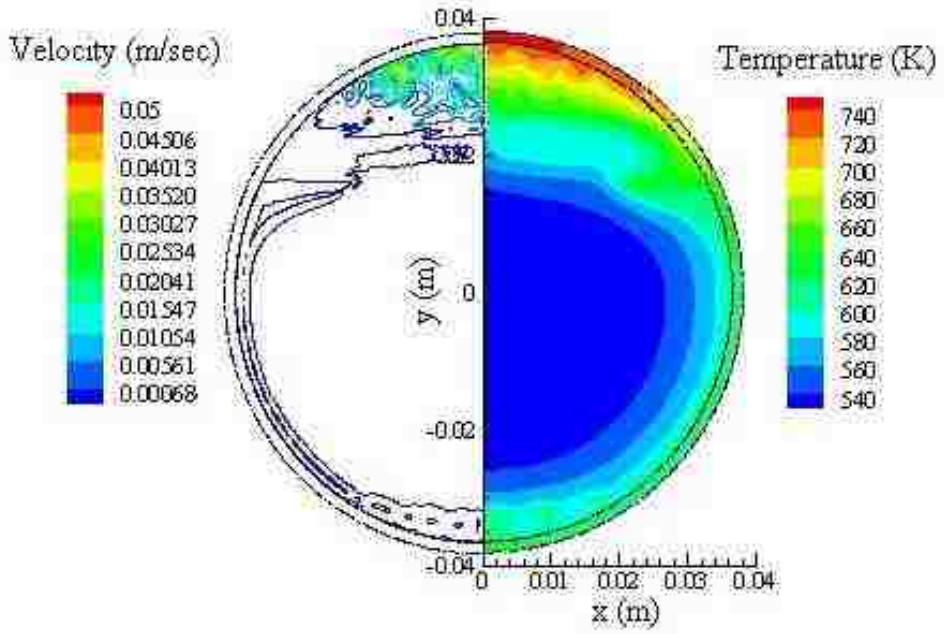

a) 300 sec

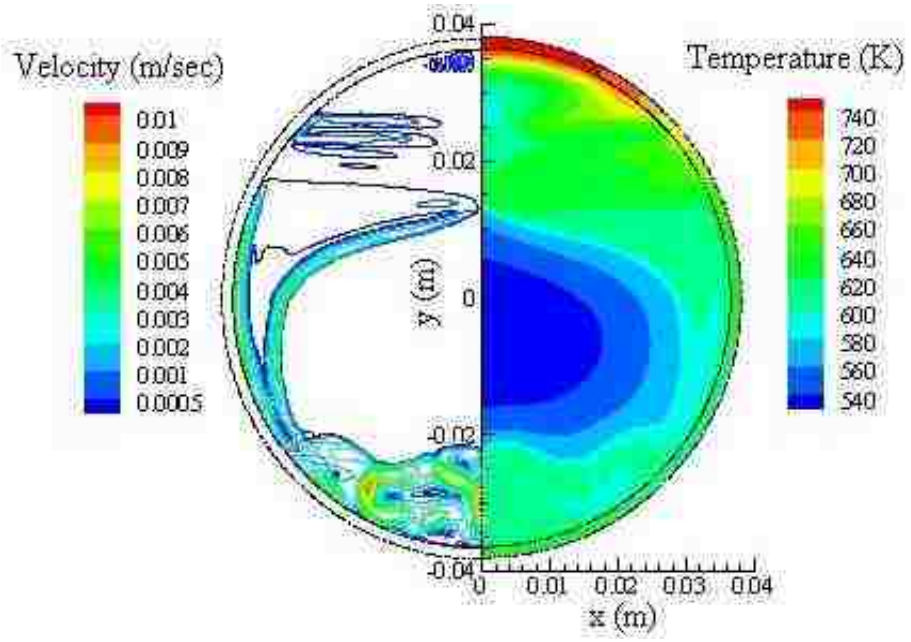

b) 600 sec

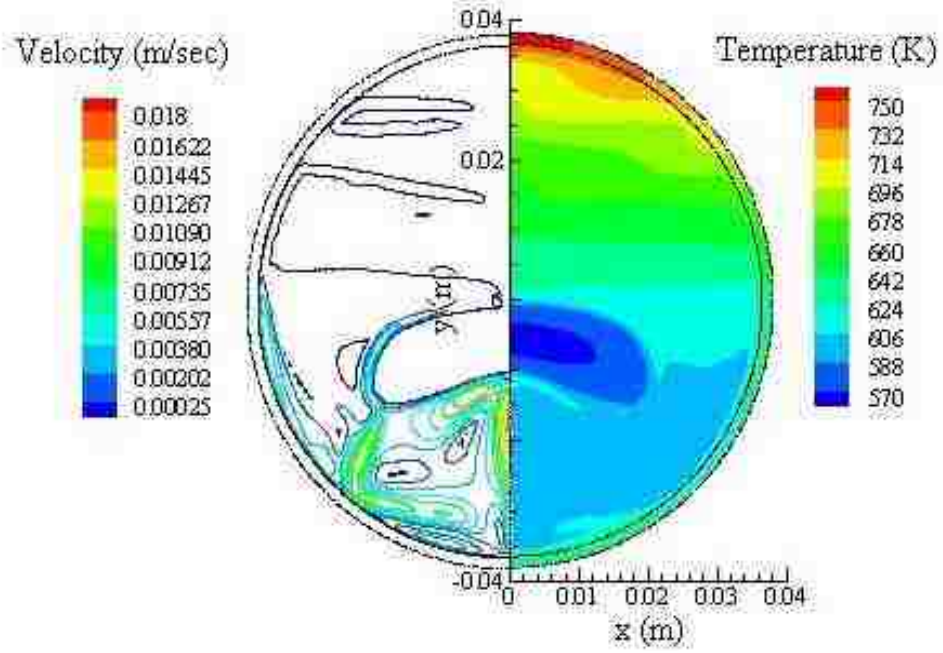

c) 900 sec

Figure 23.The isotherms and the contours of the velocity magnitude in $NaNO_3$ EPCM with 20% void. VP-1 is used as HTF.

Figure 24 (a-c) show the evolution of the liquid/solid interfaces is also similar to that of the smaller capsule for both air and VP-1 as HTF.

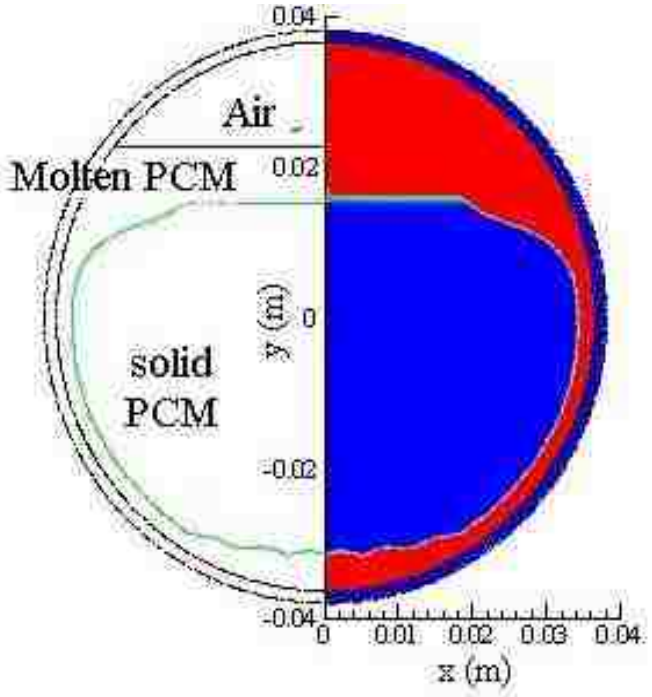

a) 300 sec

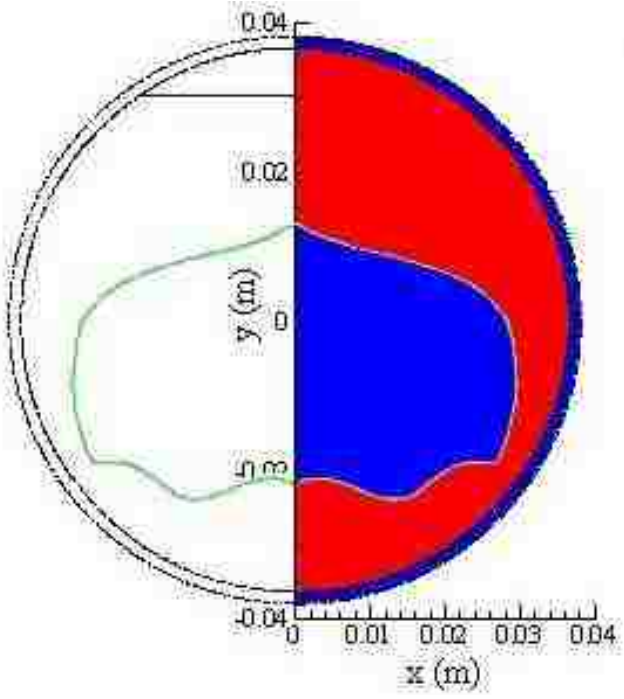

b) 600 sec

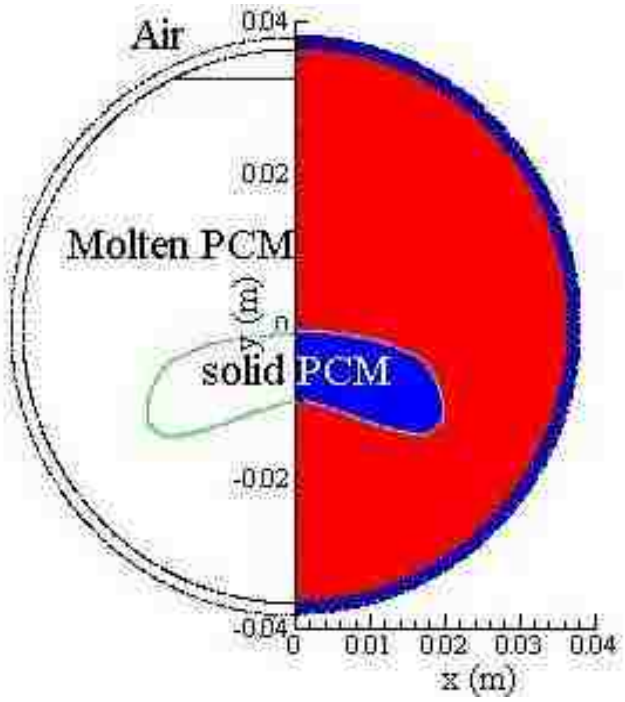

c) 900 sec

d) Figure 24. Density distribution and the location of the liquid/solid interfaces in $NaNO_3$ EPCM with 20% initial void.

4.6. Heat transfer analysis of the EPCM capsule with and without a void

Figure 25(a) and 25(b) show a comparison of the location of the propagating liquid/solid interface between an EPCM capsule with and without a void at various times for a longer capsule. The results are predicted by the enthalpy – porosity method with VOF for a 76.2 mm diameter cylindrical $NaNO_3$ capsule during a charging process using liquid VP-1 is used as the HTF. The dynamics of the interfaces in both the capsule with and without the void are different. In figure 25(a), the re-circulating vortices reshape the liquid/solid interface from concentric rings to a mushroom shape. The vortices become larger at the bottom of PCM after 600 seconds. However, in the figure 25(b) at the top of the capsule

the liquid/solid interface slowly moves because air plays the main role in reducing the melting progress along the air/PCM interface. The motion of vortices at the bottom of the capsule causes the solid PCM to separate into two parts.

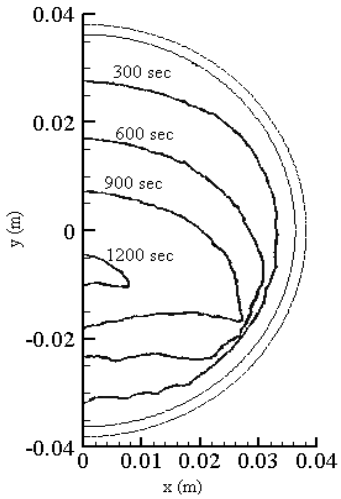

a) Without void

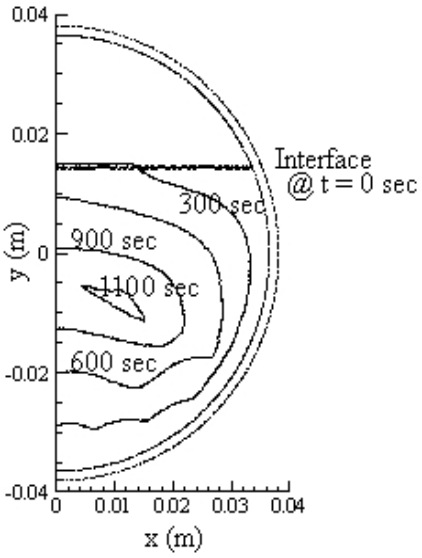

b) With void

Figure 25. The location of the propagating liquid/solid interface at various times for: (a) without void, and (b) with 20% void (air).

Figure 26(a) and 26(b) show contours of temperature and streamlines for a capsule with and without a void. Here, the temperature contours in the capsule without a void at 600 seconds shows a nearly concentric ring pattern with a slight distortion at the bottom due to the accelerated melting by the eddies. These effects are amplified in the capsule with the void as shown in figure 26(a). Streamlines and temperature contours become slightly different in both cases. Figure 26(b) shows that in a PCM capsule with a void, buoyancy – driven convection drives to create much bigger vortices than in a capsule without void. In the capsule with a void, the melting progress is much faster at the center of the capsule.

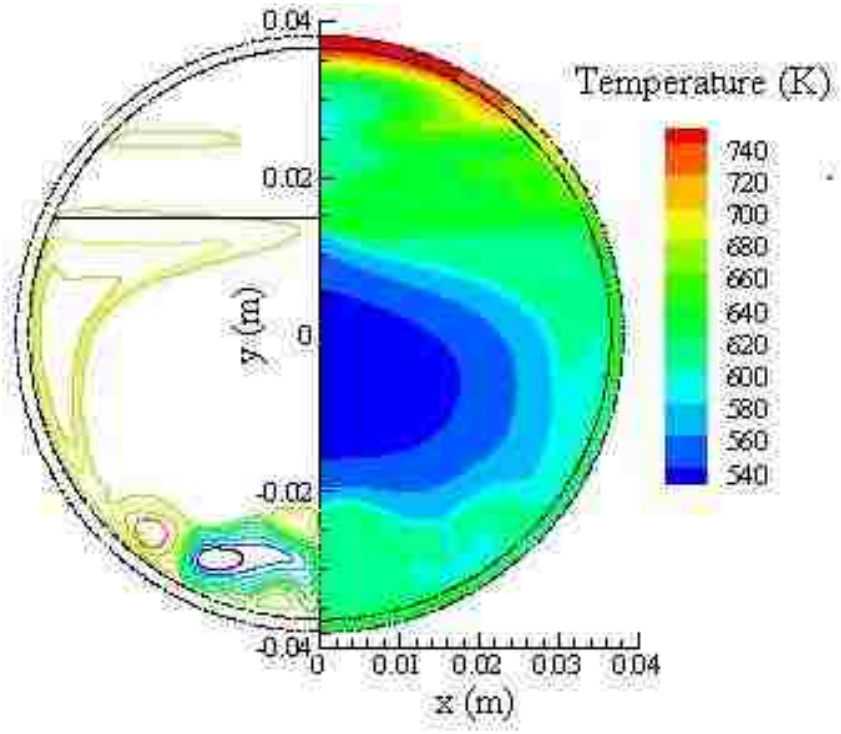

a) With void at 600 sec

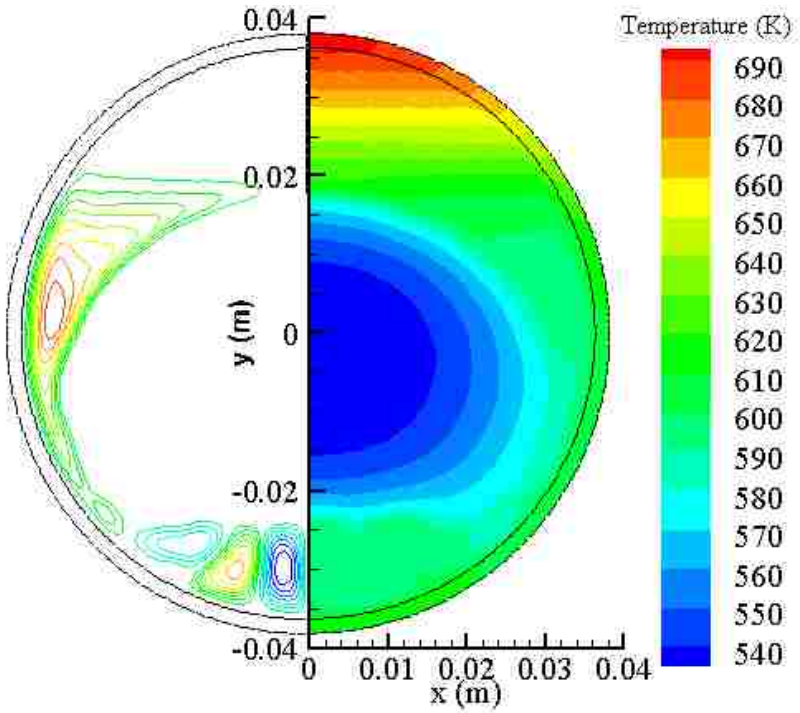

b) Without void at 600 sec

Figure 26. The isotherms and the streamlines in $NaNO_3$ EPCM at 600 sec: a) with void, and b) without void.

4.7. Conclusions

A heat transfer analysis of the melting and solidification of a $NaNO_3$-stainless steel EPCM capsules is performed using ANSYS FLUENT. Two-dimensional simulations of a 25.4 and 76.2 mm cylindrical EPCM capsules are conducted. The buoyance–driven convection inside the capsule generates vortices in the molten salt (liquid – PCM) and around the rest of solid – PCM. These vortices enhance the rate of heat transfer inside the capsule, thus, decreasing the melting/solidification time. It takes approximately 21 minutes to complete the whole phase change process while it takes about 46.2 minutes for the phase change process without considering the natural convection in the molten

$NaNO_3$. The natural convection with diffusion aids the charging and discharging process. EPCM with void is conducted using two different heat transfer fluids: air and VP-1. The shape of the solid/liquid interface is influenced by the rate of heat transfer inside the capsule. The higher rate of heat transfer achieved with VP-1 as the HTF increases natural convection within the molten salt, thus reducing the total melting time. Additionally, the presence of the air void at the top of the capsule reduces the heat transfer at the top of the capsule. The void also affects the shape of the solid/liquid interface, changing it from a circular shape to a mushroom shape. During the solidification process, the lack of natural convection in the liquid PCM and the low thermal conductivity of the PCM results in a solidification time that is 10 times longer than the melting time. Regarding to capsule configurations, the total melting time of the 76.2 mm diameter EPCM capsule with VP-1 as the HTF is 1260 seconds, which is 6.8 times longer than that of the 25.4 mm capsule.

Chapter 5 – Thermal analysis of HTF and EPCM

5.1. Motivation

Unsteady two dimensional Navier - Stokes and energy equations are solved to simulate flow passed a long EPCM rod by using SIMPLE algorithm. Enthalpy method is employed to model the phase change and heat transfer of the EPCM capsule. RANS and LES methods are used to model turbulent HTF flow passed the EPCM rod for two different values of blockage ratio. Flow past a capsule confined in a channel and the phase change heat transfer inside the EPCM pose coupled problems that need to be solved simultaneously. Sodium nitrate $NaNO_3$ is considered as the phase change material (PCM). PCM is encapsulated by a stainless steel in a long cylindrical shaped capsule. Therminol/VP-1 are used as heat transfer fluids.

5.2. Mathematical model

Transient two – dimensional simulations are conducted by employing the enthalpy–porosity method to model melting and solidification in the EPCM and by employing RANS and LES to model turbulent flows of HTF . Following assumptions are used:

- Properties are constant.
- Diffusion only process inside the EPCM.

- No volume change due to the phase change of the PCM.
- No natural convection - the buoyancy-driven in the molten PCM is neglected.
- HTF is an incompressible fluid.

As mentioned in the chapter 3, the enthalpy equation is modified to calculate for energy absorption through phase change just for diffusion term and eliminate the convection and source terms, and it could be written as:

$$\frac{\partial}{\partial t}(\rho H) = \nabla \cdot (k \nabla T) \tag{5-1}$$

where

$$H = H_s + H_{latent} \tag{5-2}$$

$$H_s = H_{s_{ref}} + \int_{T_{ref}}^{T} c dT \tag{5-3}$$

Here H is the total enthalpy, H_s is the sensible enthalpy, H_{latent} is the latent enthalpy, $H_{s_{ref}}$ is the reference enthalpy, T_{ref} is reference temperature and T is the temperature. The region of either solid or liquid could be defined as the fraction of liquid as represented in the chapter 3. In this chapter, unsteady two - dimensional Navier-Stokes and energy equations are solved to simulate flow pass an EPCM rod by using ANSYS FLUENT SIMPLE algorithm. RANS and LES [54] turbulence modeling are applied to model turbulent flows of the heat transfer fluid pass an EPCM. Predicted results from these models are compared to determine how small and large size eddies near the EPCM affects the heat transfer in the capsule and charging and discharging processes. RANS turbulent model is applied for two different values of blockage ratio.

5.3. Numerical setup

Figure 27 shows the schematic of EPCM rod placed in the channel. The mesh in the EPCM and in the flow domain of HTF is also shown in figure 27. Physical properties of all materials are considered to be constant as listed: Tables 2 and 3. Dimensions of the EPCM capsule are 76.2 mm outer diameter (D) with 1.5875 mm thickness for the stainless steel layer. However, in the channel case, the length between the center of the EPCM capsule and the inlet is 8D and the length between the center of the EPCM and the outlet is 40×D. The blockage ratio is represented by $\zeta = D/Dw$. For $\zeta = 0.7$ the number of mesh of 131,737 is sufficient to provide a converged results while the number of mesh of 320,483 is needed for $\zeta = 0.9$ to satisfy the convergence criterion. In addition, channel walls are considered to be well-insulated.

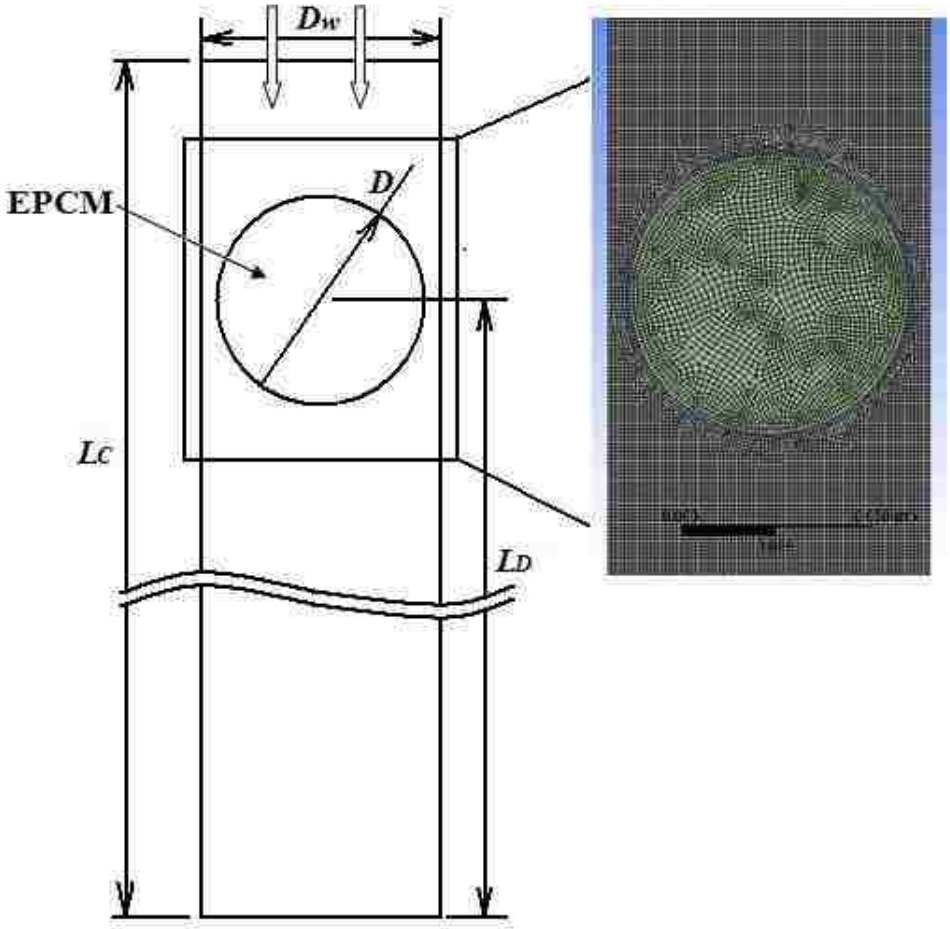

Figure 27. Schematic of the computational domain and meshing strucutre. An EPCM rod is placed in the channel.

5.4. Boundary and initial conditions

The temperature of heat transfer fluid is 550 ˚C for the charging process and 300 ˚C for the discharging process. Heat transfer fluid flows from the top to the bottom during the charging process. Therminol/VP-1 is used as the HTF in the channel. At the inlet the flow is set as a fully developed profile with the centerline velocity of U_{center} = 0.0001 m/sec for the laminar flow and U_{center} = 0.1 m/sec for the turbulent flow. The zero gage pressure

and the vanishing temperature gradient in the stream-wise direction are imposed on the velocity and temperature fields at the outlet.

5.5. Results and discussions

5.5.1. EPCM in confined wall with different blockage ratio - External flow on EPCM

Figures 28(a) and 28(b) show instantaneous stream functions for Reynolds, $Re = \rho U_{center} D/\mu$, of 38.3 in the channel for blockage ratio of $\zeta = 0.7$ and $\zeta = 0.9$. The vortices are very small and symmetric around the rear stagnation point of the cylinder when the flow is laminar for each blockage cases. Figure 28(c) and 28(d) show instantaneous stream functions for Re = 38,334 in the channel. For the turbulent flow the counter-rotating vortices becomes larger and the wake region extends downstream several times diameter of the cylinder. The vortices become asymmetric as well.

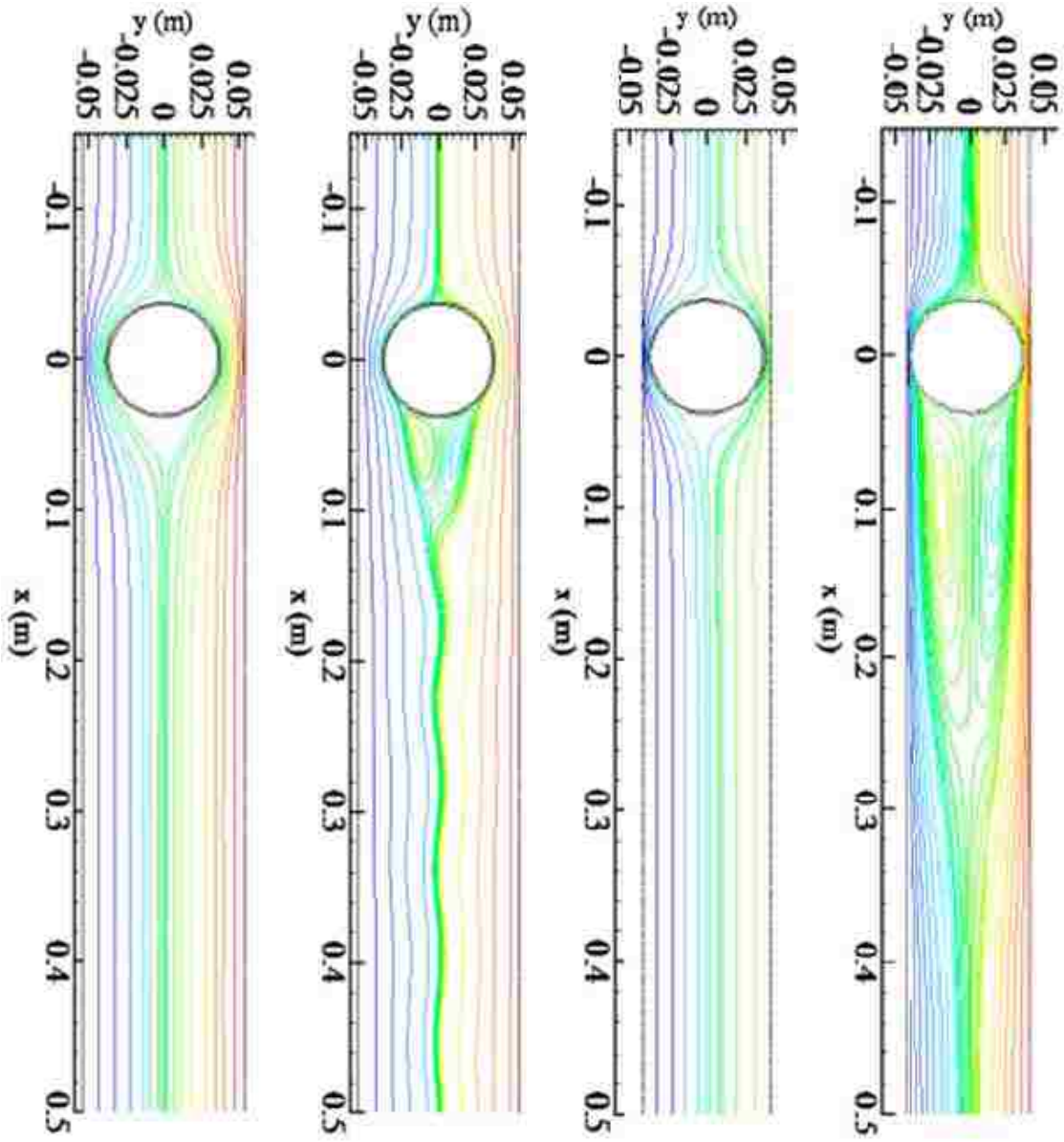

*a)*The laminar for ζ= 0.7 *b)* The laminar for ζ = 0.9 *c)* The turbulent for ζ = 0.7 *d*) The turbulent for ζ = 0.9

Figure 28. Instantaneous streamlines of HTF near the EPCM.

Figure 29 and 30 show isotherm in the HTF and inside the EPCM for the laminar flow in the channel for blockage ratio of ζ = 0.7 and ζ = 0.9 at various times. $NaNO_3$ is

considered as the PCM and the Therminol/VP-1 as HTF for all cases. The confined wall affects the shape of the temperature contours, changing it from elliptic shape at 9762 seconds to circular shape at 13562 seconds, as shown in figure 29. The temperature contours are symmetric around the rear stagnation point of the EPCM. Figure 30 shows the temperature contours around the stagnation point of the EPCM for ζ = 0.9 is quite higher than the ζ = 0.7. The solid and liquid phases of the PCM can be identified from the temperature distribution.

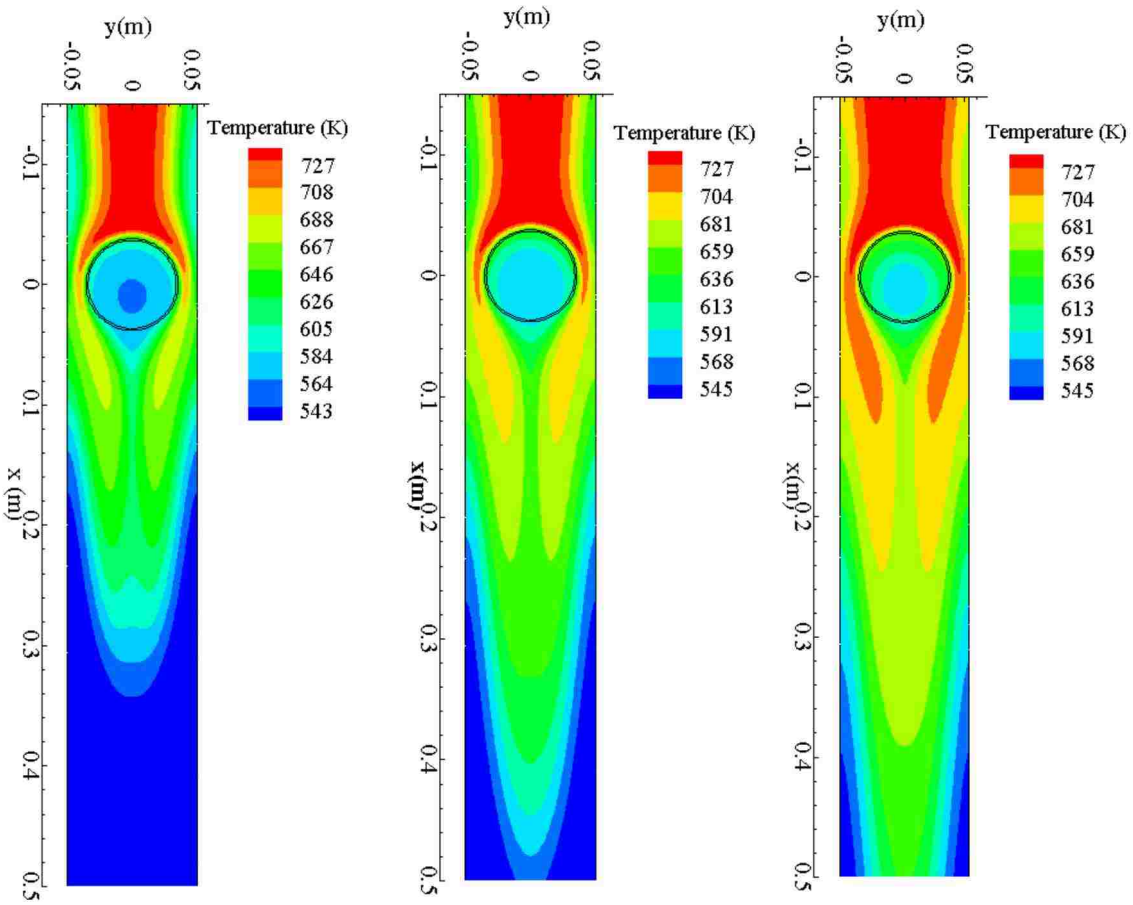

9762 seconds 11562 seconds 13562 seconds

Figure 29. Isotherms of HTF and isotherms in the $NaNO_3$ EPCM for ζ ($\equiv D/D_w$) = 0.7. The flow is laminar.

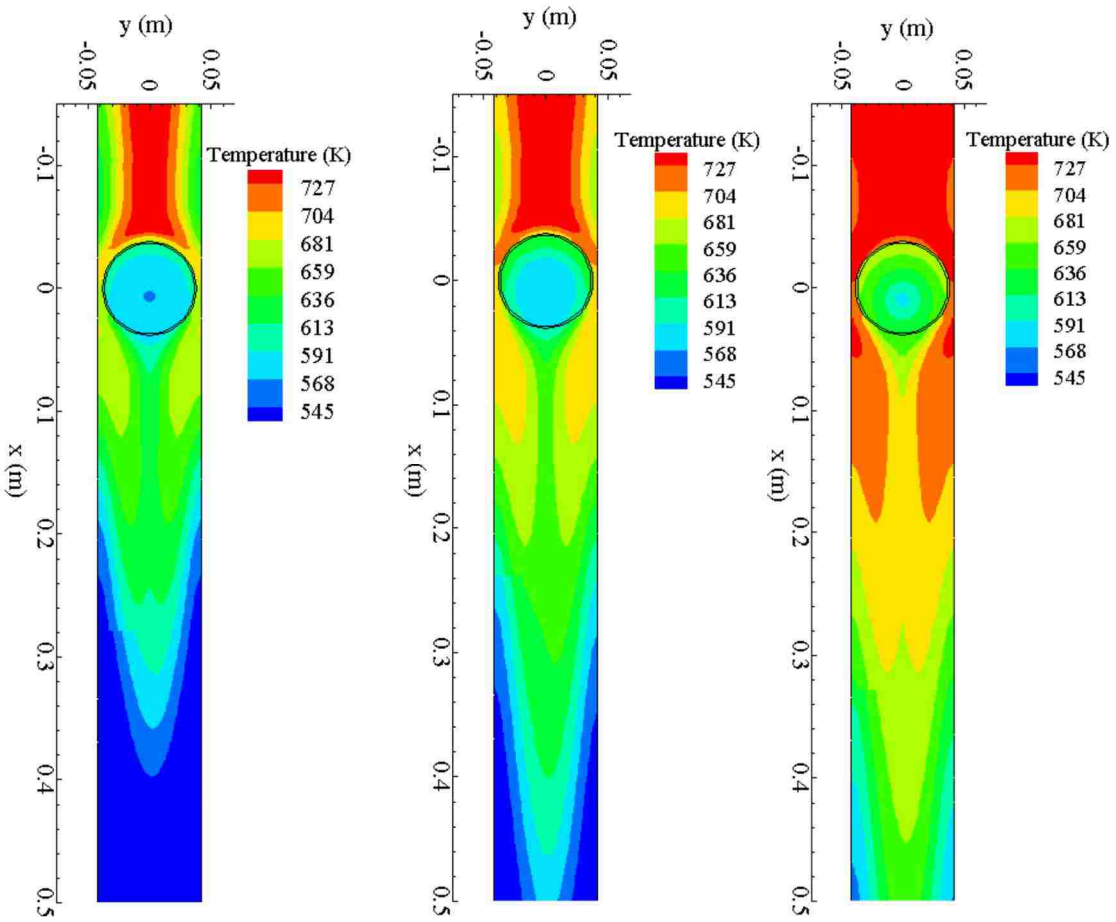

at 9342 seconds at 11147seconds at 12942 seconds

Figure 30 Isotherms of HTF and isotherms in the $NaNO_3$ EPCM for ζ ($\equiv D/D_w$) = 0.9. The flow is laminar.

Figures 31 and 32 show isotherms in the HTF and inside the EPCM for the turbulent flow in the channel for blockage ratio of ζ = 0.7 and ζ = 0.9 at various times. $NaNO_3$ is considered as the PCM. The confined wall does not affect the shape of the temperature contours inside the EPCM. For the laminar flow, the interface temperature propagates much slower compared to that when the flow is turbulent. For all cases, the temperature is below the melting temperature in the region near the center of PCM and this region

remains as the solid phase and the region outside of that PCM is melted. During this process the PCM store energy in the form of latent heat as well as the sensible heat. Energy storage by the EPCM (by the latent heat and the sensible heat) is strongly influenced by the dynamics of the flow near the EPCM capsule.

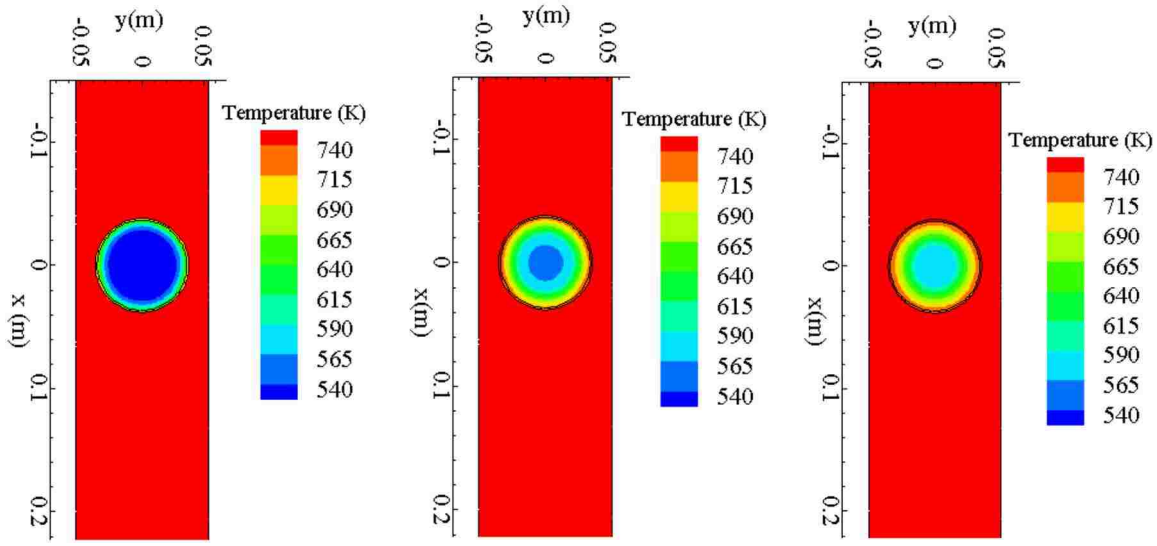

100 seconds 900 seconds 1800 seconds

Figure 31. Isotherms of HTF and isotherms in the $NaNO_3$ EPCM for ζ ($\equiv D/D_w$) = 0.7. The flow is turbulent.

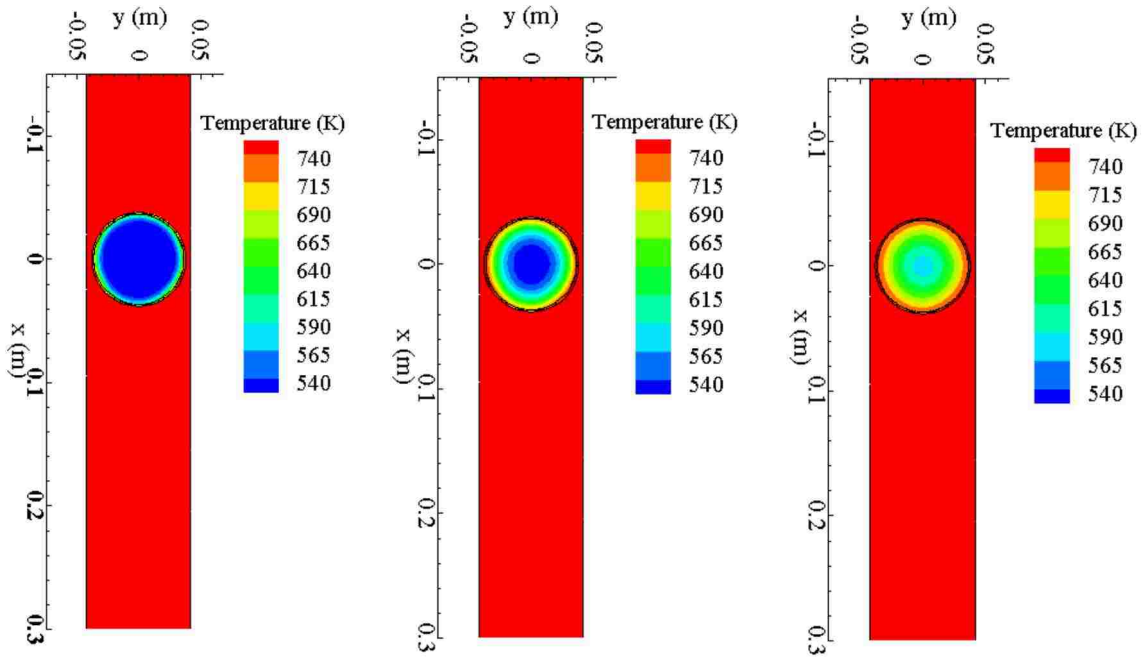

90 seconds 400 seconds 900 seconds

Figure 32. Isotherms of HTF and isotherms in the $NaNO_3$ EPCM for ζ ($\equiv D/D_w$) = 0.9. The flow is turbulent.

Figures 33 and 34 show the location of the propagating liquid/solid interface predicted by the enthalpy – porosity method at various times for the laminar flows in the channel for the blockage of 0.7 and 0.9. At 9762 seconds, the shape of dynamic liquid/solid interface is shaped as elliptic profile. Additionally, heat transfer in the wake of the EPCM is slowest so the bottom part of the EPCM melts much slower. Also the solid PCM sinks to the bottom of the capsule, as shown in figure 33(b). However, the melting process is much faster when the blockage ratio is larger, as shown in figure 34(b) and (e).

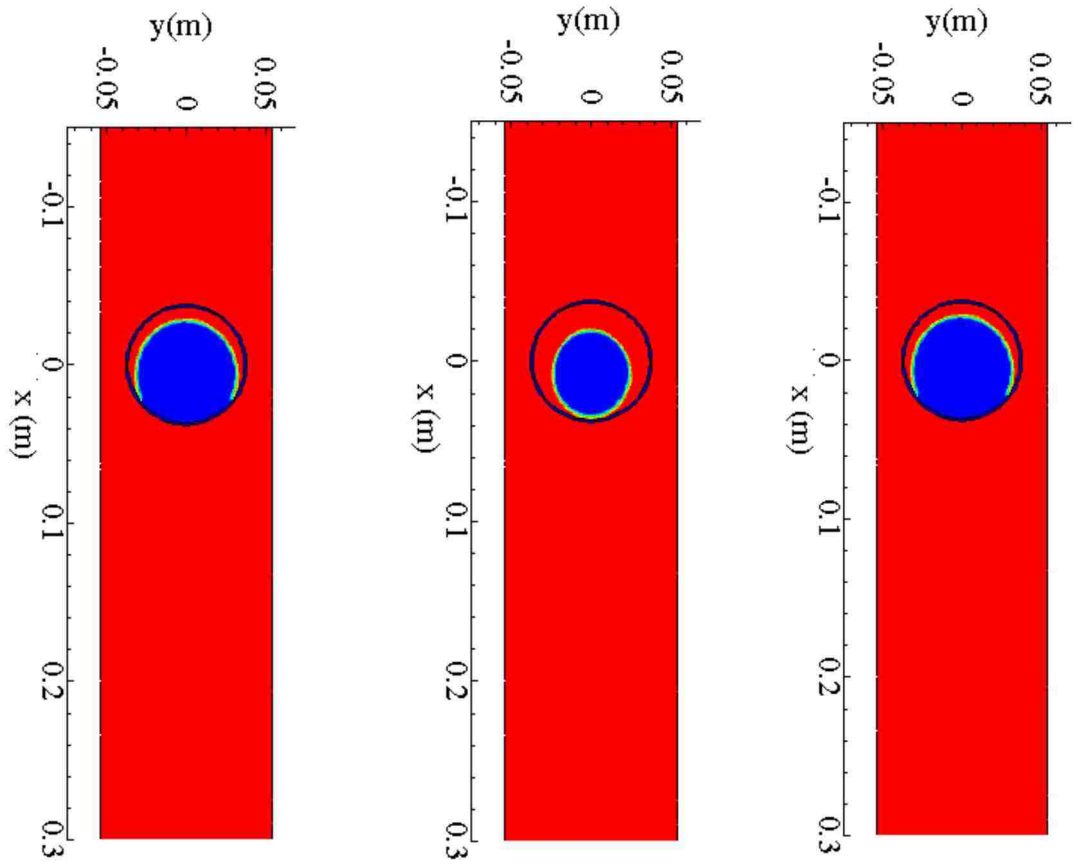

9762 seconds 11562 seconds 13562 seconds

Figure 33. The location of the solid/liquid interface in the $NaNO_3$ for ζ ($\equiv D/D_w$) = 0.7. The flow is laminar.

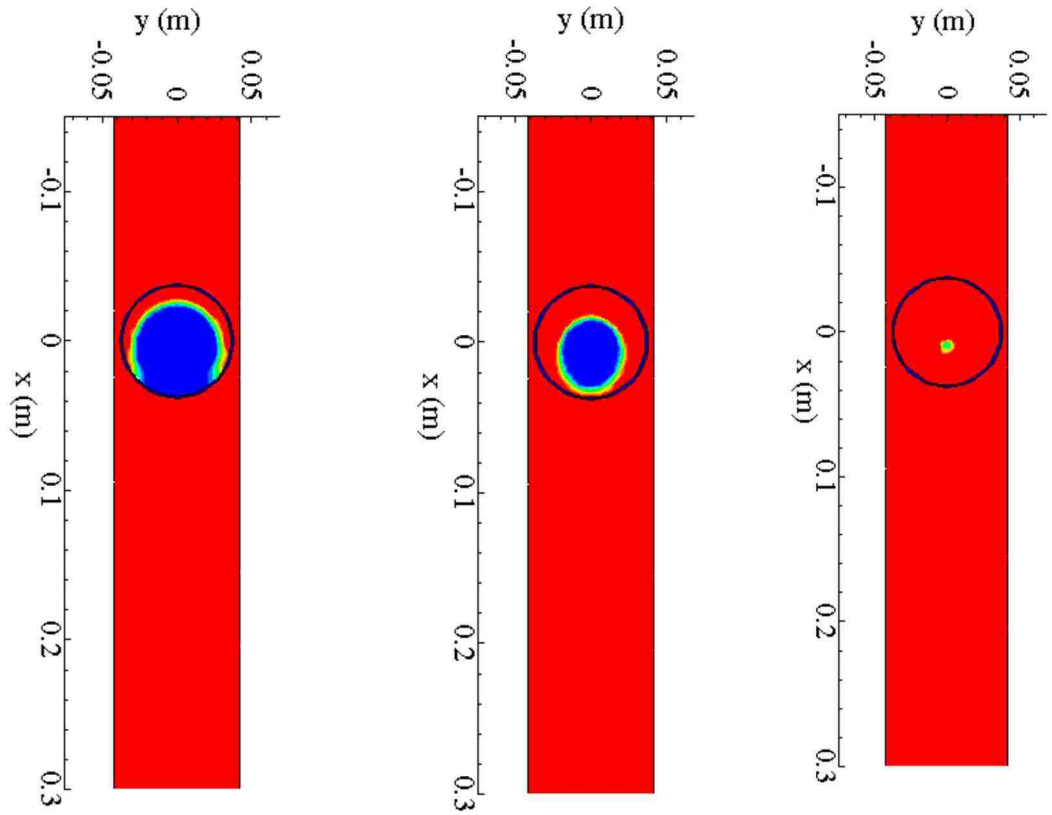

Figure 34. The location of the solid/liquid interface in the $NaNO_3$ for ζ ($\equiv D/Dw$) = 0.9. The flow is laminar.

Figures 35 and 36 show the location of the propagating liquid/solid interface predicted by the enthalpy – porosity method at various times for the turbulent flows in the channel for the blockage of 0.7 and 0.9. The dynamics of the interface is strongly influenced by the nature of the flow around the EPCM. The liquid/solid interface is nearly circular at all times, as clearly seen in Figures 35(b) and 36(b). Melting process is an order of magnitude faster when the flow is turbulent inside the channel compared to that when the flow is laminar.

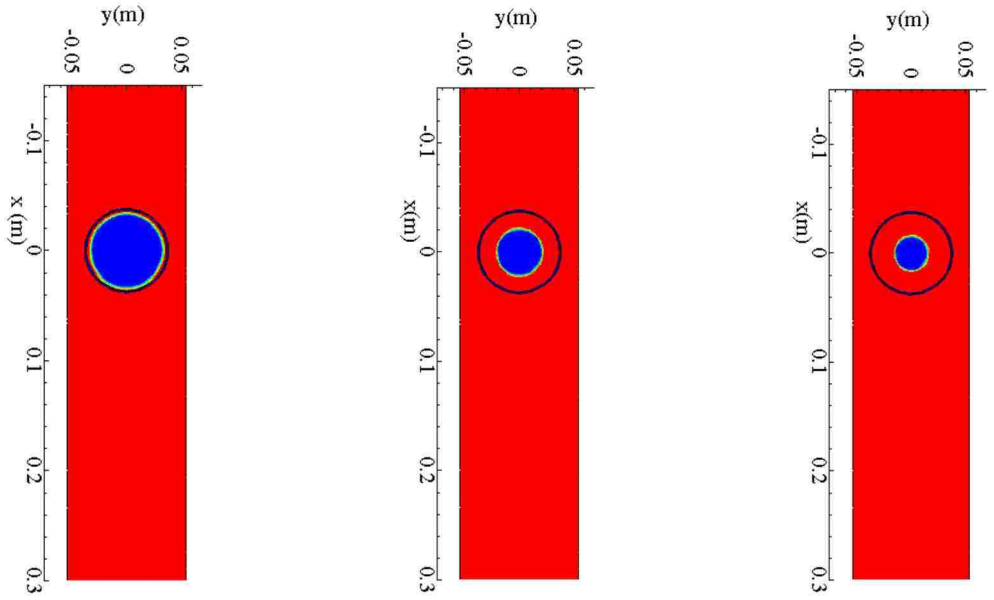

a) 100 seconds b) 900 seconds c) 1800 seconds

Figure 35. The location of the solid/liquid interface in the $NaNO_3$ for ζ ($\equiv D/Dw$) = 0.7. The flow is turbulent.

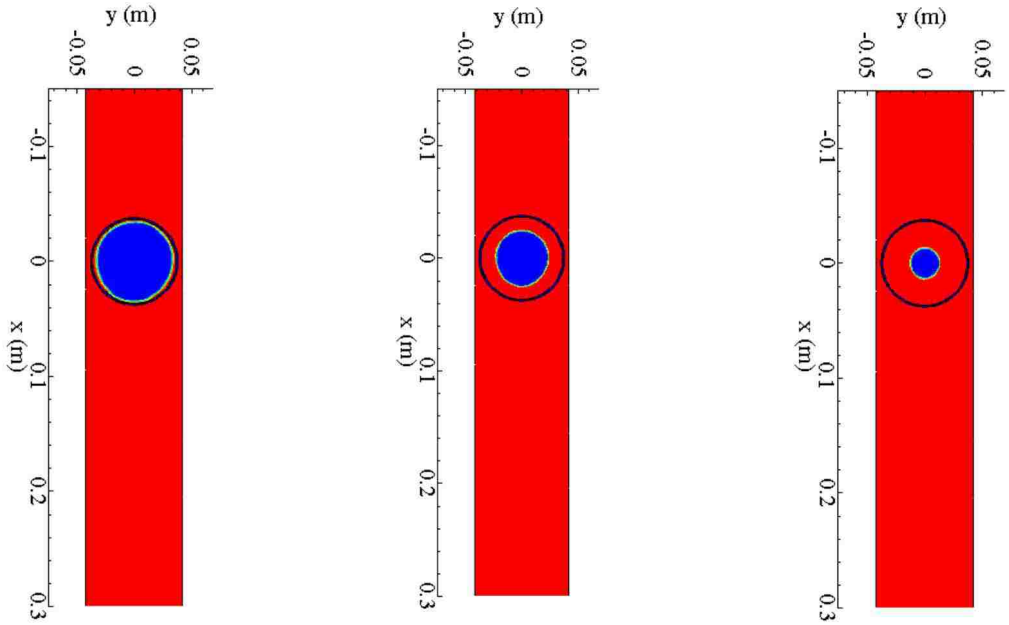

a) 90 seconds b) 400 seconds c) 900 seconds

Figure 36. The location of the solid/liquid interface in the $NaNO_3$ for ζ ($\equiv D/Dw$) = 0.9. The flow is turbulent.

Similarly, Figure 37 the location of the interface at various times during melting process predicted by the enthalpy methods for 76.2 mm diameter. EPCM capsule is illustrated in figure 37 (a) and figure 37 (b) for blockage ratios $\zeta = 0.7$ and $\zeta = 0.9$. For $\zeta = 0.9$, the phase change process is much faster compared to the blockage ratio $\zeta = 0.7$. Since the rate of heat transfer at the surface from the HTF to the EPCM is much higher. The melting process is also significantly faster when the blockage ratio is larger since the heat transfer from HTF to the EPCM increases as the gap between the EPCM and the channel wall becomes smaller.

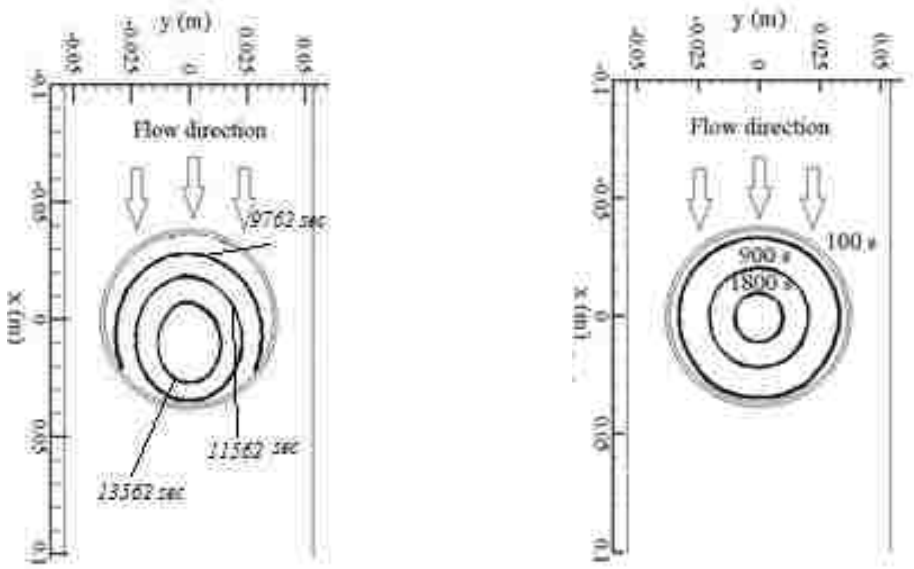

a) Laminar for $\zeta = 0.7$ b) Turbulent for $\zeta = 0.7$

Figure 37. The location of the liquid/solid interface at various times.

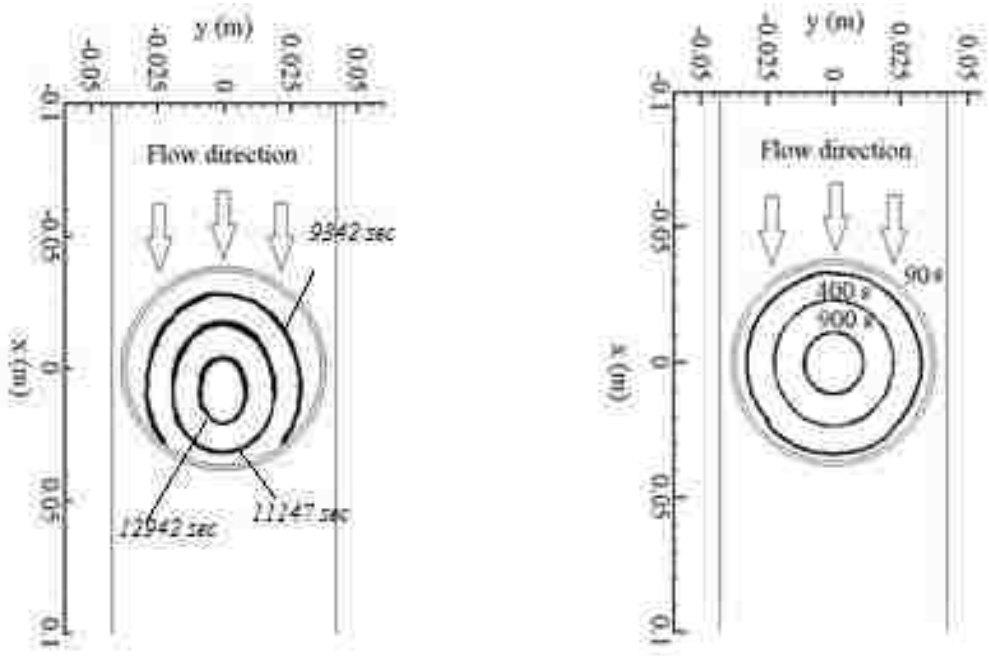

a) Laminar for $\zeta = 0.9$ b) Turbulent for $\zeta = 0.9$

Figure 38. The location of the liquid/solid interface at various times.

5.5.2. Large eddy simulation

A large eddy simulation (LES) method is employed to investigate more detailed flow structure and more accurate dynamics of the flow near the EPCM. 131,426 nodes and the time step of 10^{-6} seconds are used to simulate the HTF flow and the phase changing heat transfer in the EPCM. The LES filters the small eddies and identifies the dynamics and the spatial structures of the large eddies explicitly in the flow [33, 35]. Detailed description of the method is given in chapter 3. The contours of the vortices and the stream function for *Re* = 38,334 illustrates the presence of the vortex shedding in the wake of the EPCM as shown in figure 38. In order to determine the shedding frequency

the lift coefficient [55] is calculated and plotted in figure 39. It clearly indicates that the vortex formation and shedding are perfectly periodic with the dominant frequency of 0.48 1/s as depicted by the power spectral density of the lift coefficient shown in Figure 39(b). The Strouhal number of the vortex shedding is calculated to be $St = 0.36$ for the blockage ratios of $\zeta = D/D_w = 0.7$. The frequency of the vortex shedding predicted here ($St = 0.36$ for $\zeta = 0.7$) agrees with the date reported by other investigators [55].

The LES provides more detailed flow characteristics, but it requires much more CPU time [35].In many practical applications acquiring detailed flow structure may not be necessary. To understand the effect of the eddy dynamics on the thermal energy storage into the EPCM the average value of the heat transfer coefficient along the surface of the EPCM predicted by the LES and the RANS are calculated. Figure 40 shows the comparison of the heat transfer coefficient predicted by RANS and LES for Re = 38,334 and $\zeta = 0.7$. The heat transfer coefficient along the surface of the EPCM predicted by the LES is compared against that predicted by the RANS. The heat transfer coefficient along the capsule is calculated at t = 50 seconds by employing both methods. LES prediction is higher along the surface except in the region close to the rear stagnation point, as illustrated in Figure 41. This can be attributed to the effect of vortex shedding or the difference in turbulence modeling.

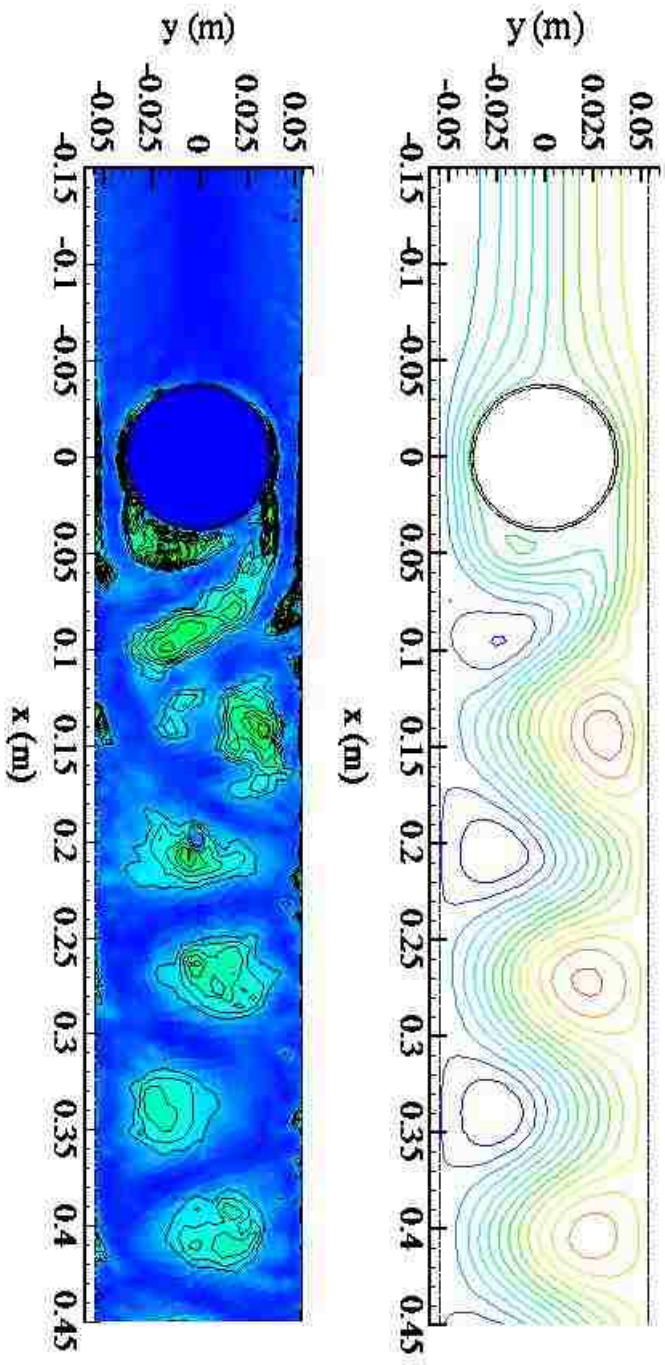

Figure 39. Vorticity contours and the function stream predicted by LES turbulence model.

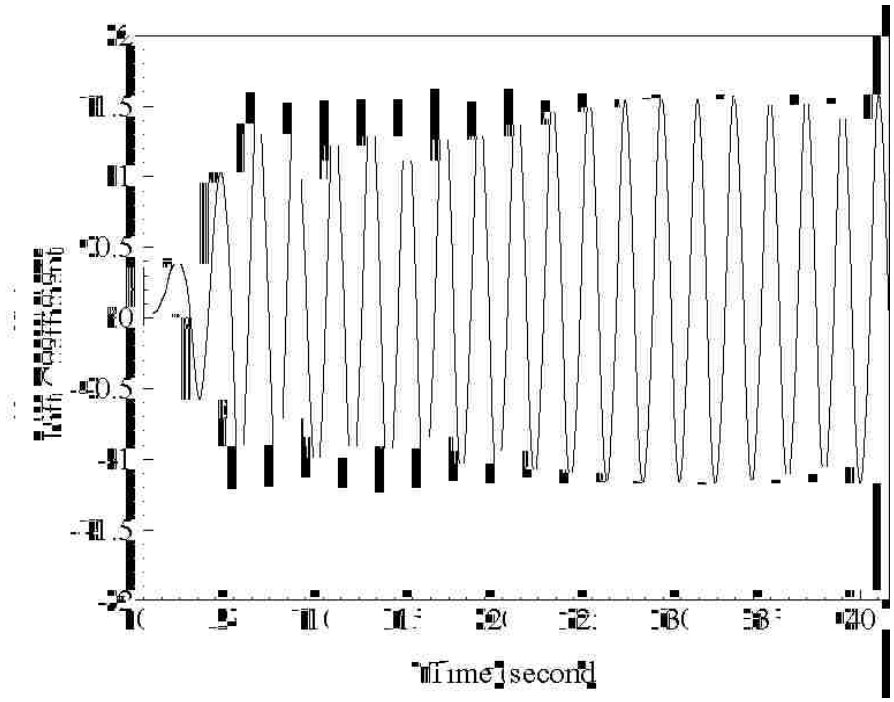

a) lift coefficient

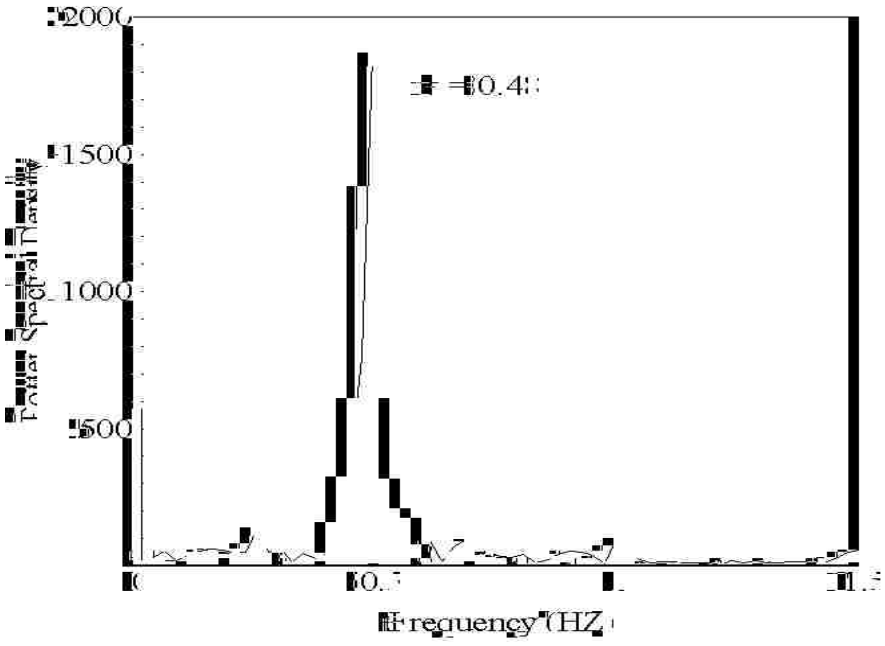

b) frequency

Figure 40. LES turbulence model: a) lift coefficient, and b) frequency.

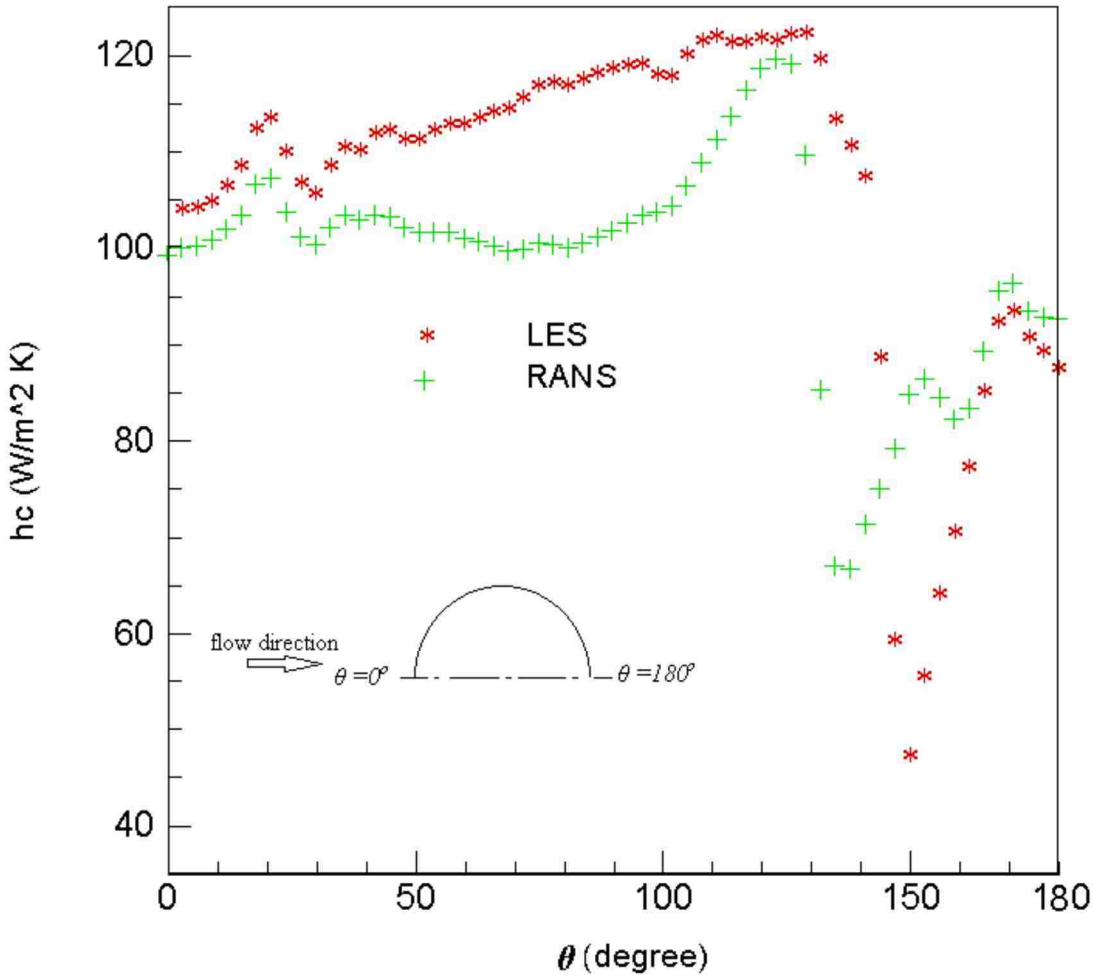

Figure 41. Heat transfer coefficient along the surface of the EPCM at t = 50 seconds predicted by LES and RANS

This will ensure that the phase change phenomenon and the heat transfer inside the EPCM will hardly be influenced by the vortex shedding or other smaller scale flow structure. Moreover, the storage times are in the order of 1,000 or even 10,000 seconds, the vortex shedding with 0.45 1/s frequency will have a little influence on the dynamics of the energy storage into the EPCM.

Table 10 depicts the energy storage and the retrieval times predicted by the enthalpy-porosity method/RANS using Therminol/VP-1 as the HTF. The energy storage and the retrieval times are significantly shorter for the turbulent flow inside the channel compared

to those for the laminar flow. Obviously, the tighter confinement of the cylinder inside the channel shortens the total time for the charging and the discharging for the same size of the EPCM.

Table 10. Heat transfer times for the EPCM in the channel using liquid Therminol/VP-1 as HTF. Re = 38.3 for the laminar flow and Re = 38,334 for the turbulent flow for ζ = 0.7 and 0.9 .

	Total times (seconds) for ζ = 0.7		Total times (seconds) for ζ = 0.9	
	Laminar flow	Turbulent flow	Laminar flow	Turbulent flow
Charging Process	15,762	2,030	14,747	1,176
Discharging Process	30,427	2,155	---	---

5.6. Conclusions

The enthalpy-porosity method is employed to simulate the melting/solidification progress and RANS and LES methods are applied to model the HTF passes the single EPCM. $NaNO_3$ is used as PCM and Therminol/VP-1 as HT. Melting process is an order of magnitude faster when the flow is turbulent inside the channel compared to that when the flow is laminar. The phase change phenomenon and the heat transfer inside the EPCM is hardly be effected by the vortex shedding or smaller scale flow structure. The Strouhal number of the vortex shedding is calculated and is confirmed with reported results in the literature. One of the significant outcomes of the present work is that better understanding of the heat transfer from HTF to the EPCM as well as the heat transport inside the EPCM.

It will help design the high temperature thermal energy storage modulus in the concentrated solar power systems and in other industrial applications.

Chapter 6 – Thermal Analysis for EPCMs Thermocline

6.1. Motivation

Thermal analysis for a thermocline consisting of encapsulated phase change material capsules is conducted. $NaNO_3$ is used as PCM. Latent heat and sensible heat stored in EPCM capsules in the thermocline are predicted and compared against those measured at Lehigh University by Zheng et al. [56-58]. Following assumptions are used:

- Two - dimensional geometry for thermocline.
- No volume change due to the phase change of the PCM.
- No natural convection - the buoyancy-driven in the molten PCM is neglected.
- HTF is an incompressible fluid.

The copper capsule is used in experiments for calibration [56]. Simulation is conducted for thermocline with copper and $NaNO_3$ capsules [57]. Agreement between predicted and measured results validates the mathematical model and the numerical model. Figure 42 shows the direction of the flow in two dimensional geometry of the thermocline.

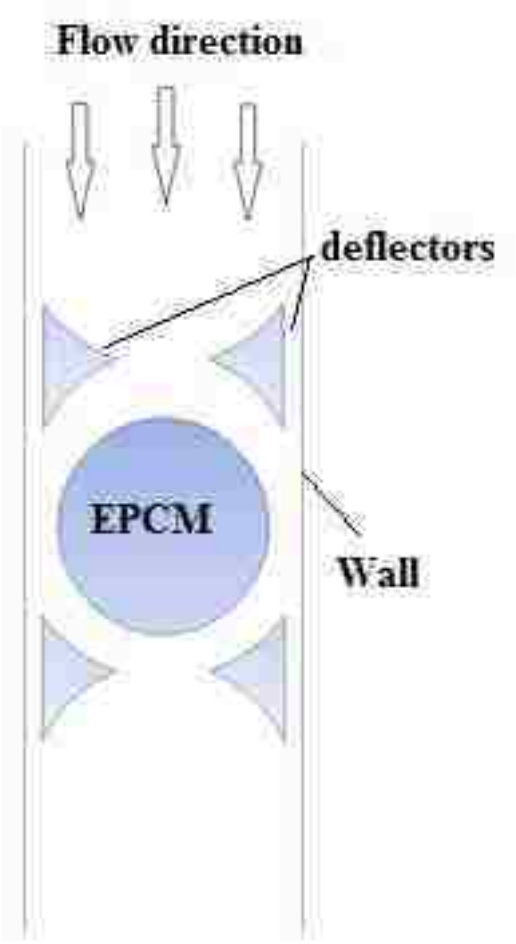

Figure 42. Schematic of an EPCM thermocline.

6.2. The thermocline description and material properties

The thermocline described and built at Lehigh University has the dimension of $0.26m \times 0.09m \times 1.2m$. The diameter of the EPCM is 0.0762 m and the length is 0.254 m. The latent heat thermocline contains capsules that include phase change materials. The vessel is well insulated to minimize heat loss, as shown figure 43. The total stored/retrieval energy (latent and sensible) are carried out to the test section using hot/cold air and stored/retrieval into/from the EPCM, walls, and insulation.

Figure 43. Thermocline model section with insulation [56, 58].

Figure 44 shows the schematic of the HTF that is driven to the thermocline from the top to the bottom as described by the layout as shown. During charging, heat transfer fluid, air, is heated by an electrical heater (36 kW). After air flows through the thermoclines

during the storage and retrieval process, it is cooled to reach the ambient temperature at a zero gage pressure.

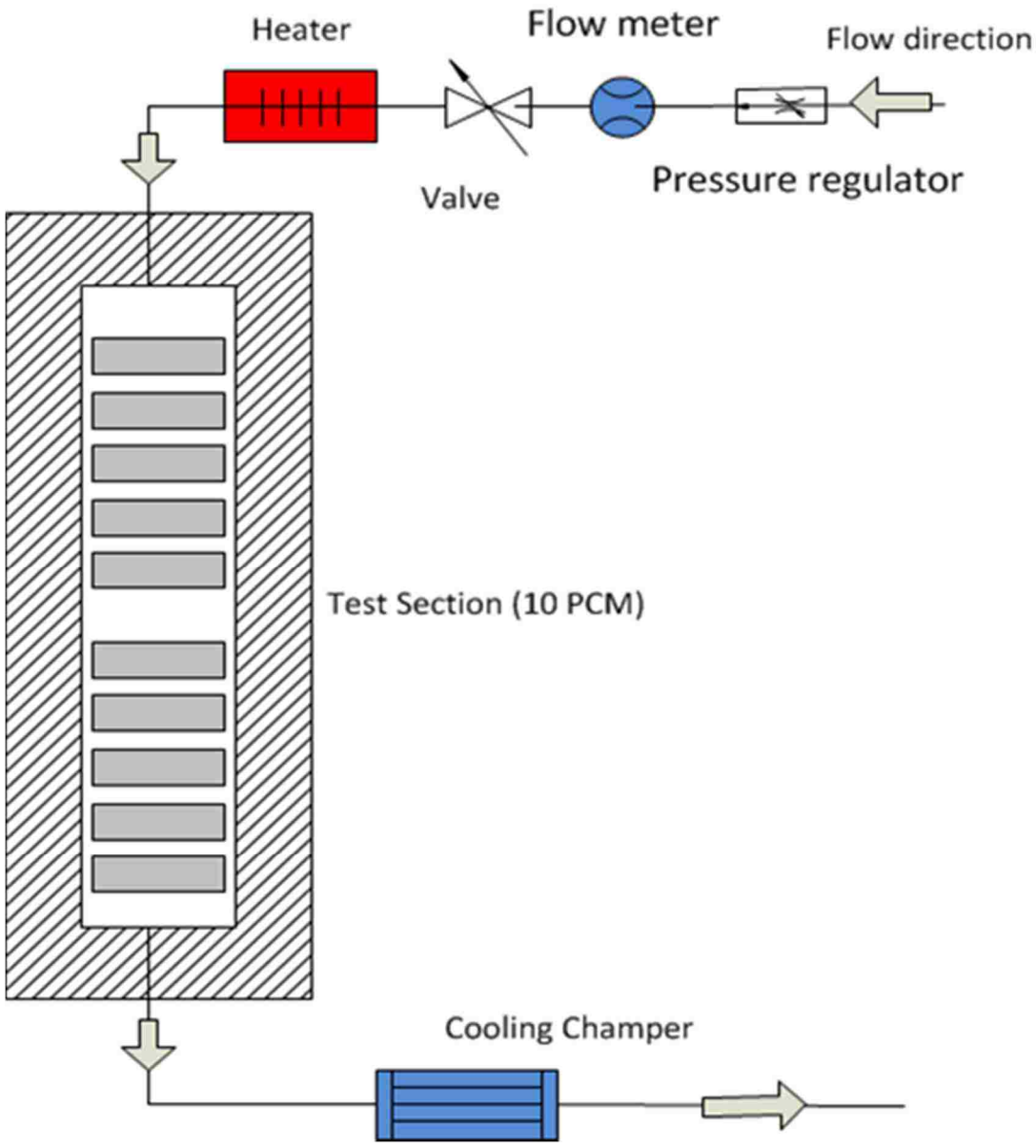

Figure 44. Schematic of layout of the test section.

Table 11. Material properties [56]

Material	Properties	Value of the property function in temperature (°C.)
Air	Density (kg/m^3)	$1.47 \times 10^{-11}T^4 - 2.117 \times 10^{-8}T^3 + 1.26 \times 10^{-5}T^2 - 4.511 \times 10^{-3}\,T + 1.29$
	Heat capacity($J/kg\,K$)	$3 \times 10^{-3}T^2 + 3 \times 10^{-2}\,T + 1005.1$
	Thermal conductivity(W/mm)	$2.201 \times 10^{-8}T^2 + 7.509 \times 10^{-5}\,T + 2.365 \times 10^{-2}$
	Viscosity ($kg/m\,s$)	0.001
Copper	Density (kg/m^3)	9105
	Heat capacity ($J/kg\,K$)	$0.0963\,T + 384.5$
	Thermal conductivity(W/mm)	400
Test section Wall	Density (kg/m^3)	11493
	Heat capacity ($J/kg\,K$)	$0.0002\,T^2 + 0.3009\,T + 473.49$
	Thermal conductivity	0.5
Insulation	Density(kg/m^3)	93
	Heat capacity ($J/kg\,K$)	$2 \times 10^{-6}T^3 - 2 \times 10^{-3}T^2 + 1.4 \times T + 735.7$
	Thermal conductivity	0.08

6.3. Mathematical model

The enthalpy – porosity method is employed to model the heat transfer and the phase change inside the capsule. RANS is used to characterize the heat transfer fluid flows inside the thermocline. Some of physical properties are taken as a function of temperature, as listed in Table 11. The buoyancy-driven convection and the volume changes in the EPCM are neglected. As mentioned in the chapter 3, the enthalpy equation is modified to calculate latent heat and the sensible heat storage. Only conduction heat transfer is included in the model:

$$\frac{\partial}{\partial t}(\rho H) = \nabla \cdot (k \nabla T) \tag{6-1}$$

where

$$H = H_s + H_{latent} \tag{6-2}$$

$$H_s = H_{s_{ref}} + \int_{T_{ref}}^{T} c dT \tag{6-3}$$

Here H is the total enthalpy, H_s is the sensible enthalpy, H_{latent} is latent enthalpy, $H_{s_{ref}}$ is the reference enthalpy, T_{ref} is reference temperature and T is the temperature.

The dimension of the thermocline, the insulation layer around it, and the inner structure of the thermocline are matched the thermocline built and tested at Lehigh University. The inlet and the outlet velocity and the thermal boundary conditions are selected to simulate the experiments conducted by Lehigh University scientists. The ambient air temperature is *300.7* K; the convection heat transfer coefficient at the outside wall of the thermocline is *5* $W/m^2 K$; the mass flow rate of air varies from 0.2 to 0.5 *kg/sec*.

Figure 45 (a) and (b) show the inlet temperature as a function of time for a charging and a discharging process for copper rods and $NaNO_3$, respectively.

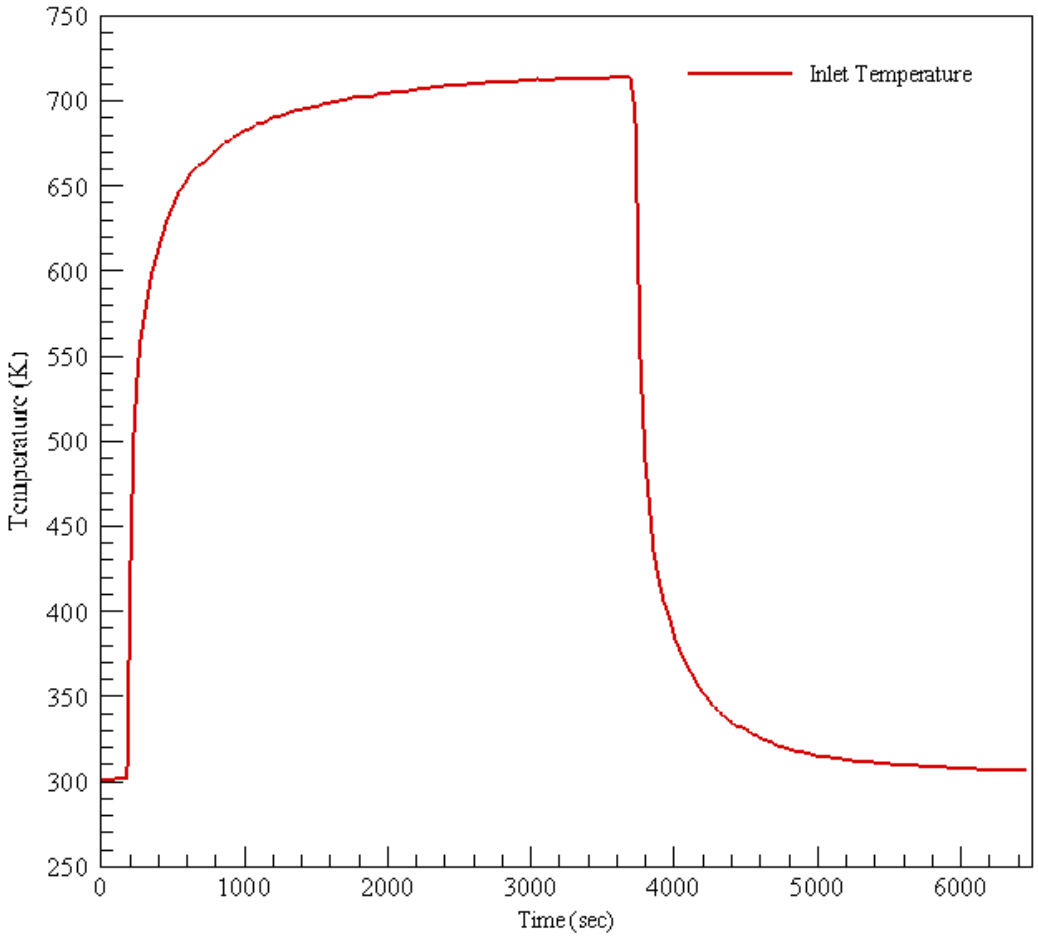

a) Copper capsules [58]

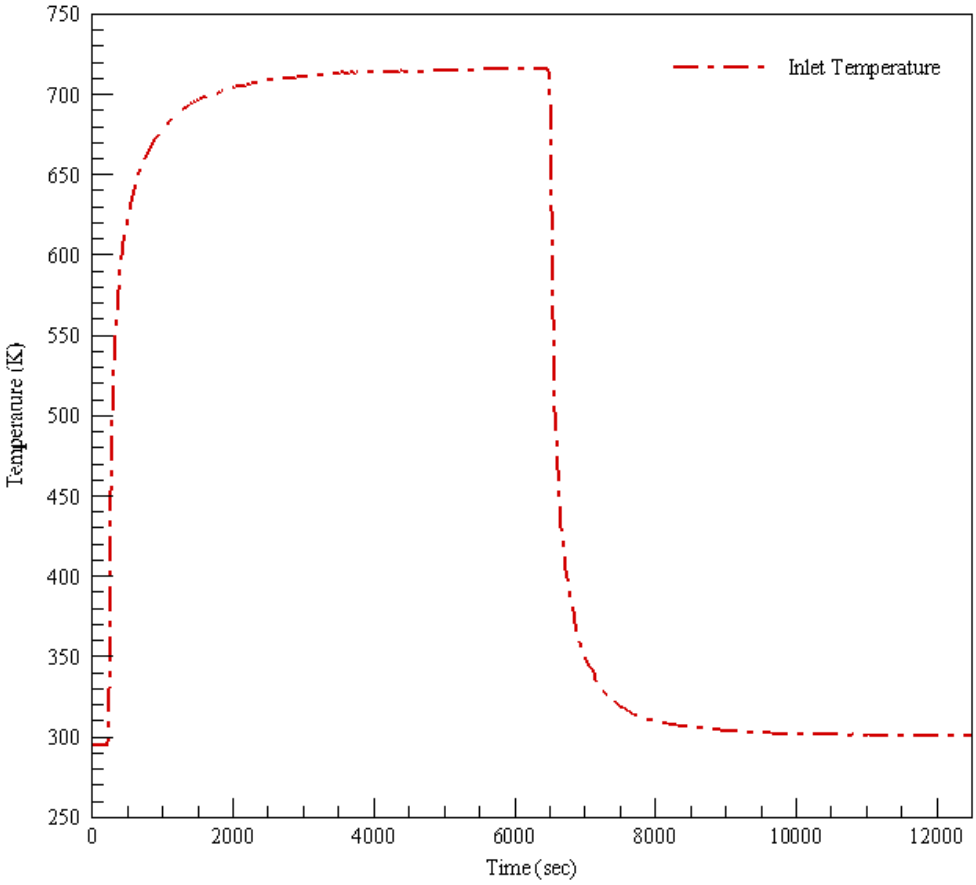

b) $NaNO_3$ Capsules [57]

Figure 45. The inlet temperature distribution for thermocline a) the copper rod thermocline b) the $NaNO_3$.

Unstructured meshes are generated for the computational domain as shown in figure 46. A triangular mesh is used. The interface of the different materials is conjugated very well, in order to accurately, determine heat transfer exchanges between different media.

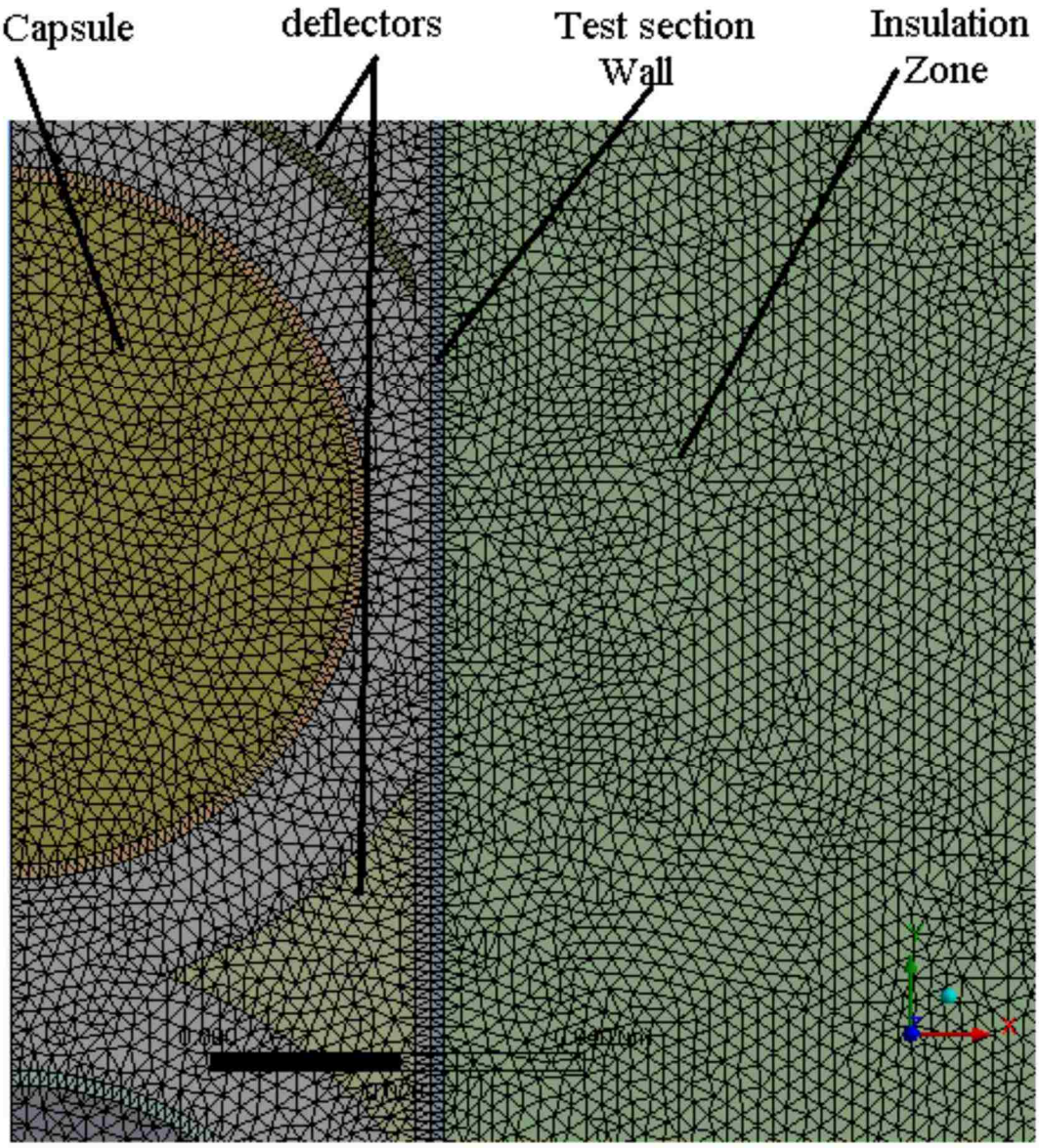

Figure 46. The cross section of the unstructual mesh for the test section.

Iteration at each time step continues for regions in HTF and in PCM until the residuals reach below 10^{-6} for the energy equation and 10^{-3} for both the continuity and the momentum equations at each node.

6.4. Validation of the numerical method

Charging and discharging process in the thermocline consisting of the copper rods are simulated for one thermal cycle. Temperature of each copper is determined and compared against the experiments conducted by Zheng et al. [56-58]. Figure 47 (a-j) shows the temperature distribution during one charging/discharging cycle for copper capsules. The results predicted by numerical solutions agree well with the experimental results in the first five copper rods as shown in figure 47 (a-e). There is a slight difference in the temperature signal predicted and measured for the last five copper rods. The maximum deviations between the predicated and measured temperature is still less than 10%. The deviation in temperature can be attributed to the experimental uncertainties in measuring temperature. It is also possible that the turbulent flow is not very accurate.

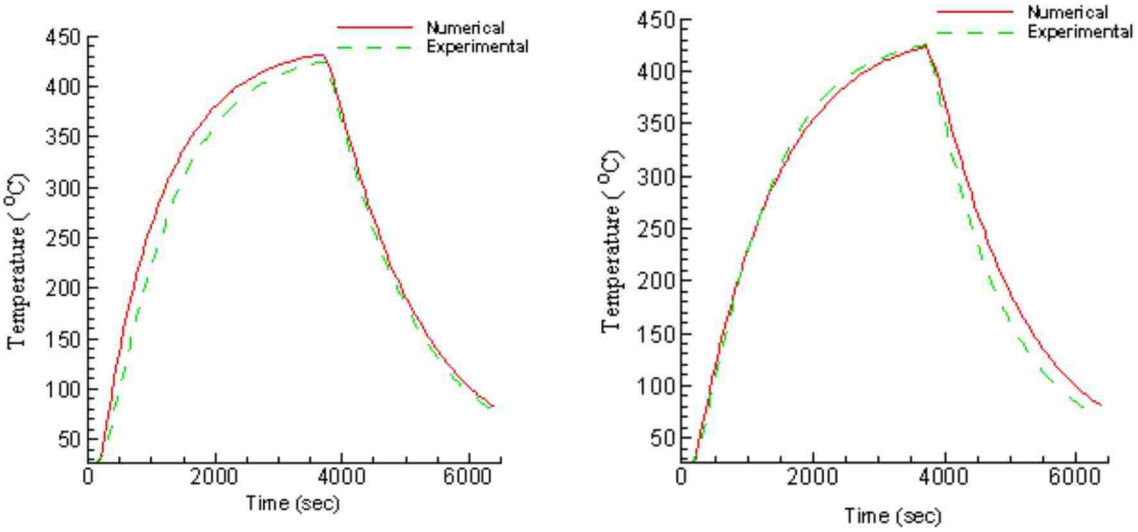

a) Capsule No. 1 b) Capsule No. 2

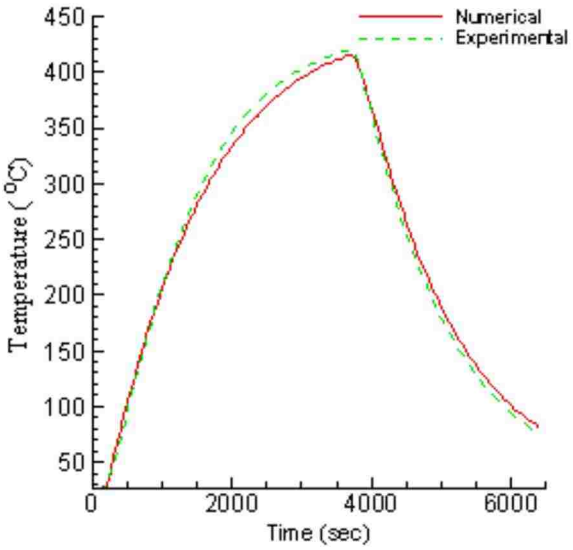

c) Capsule No. 3

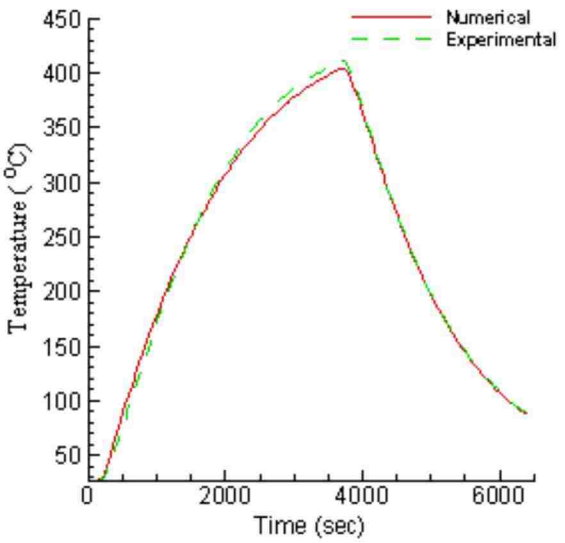

d) Capsule No. 4

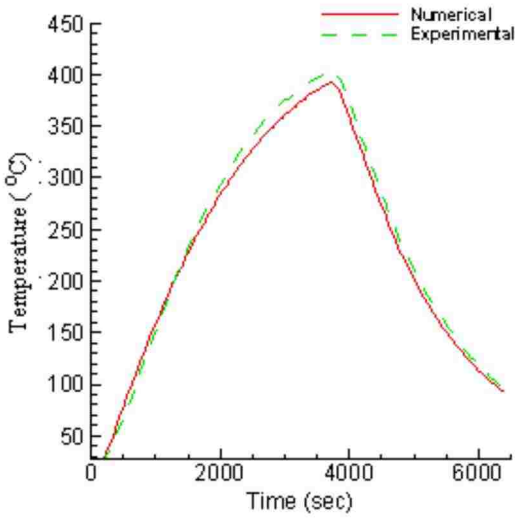

e) Capsule No. 5

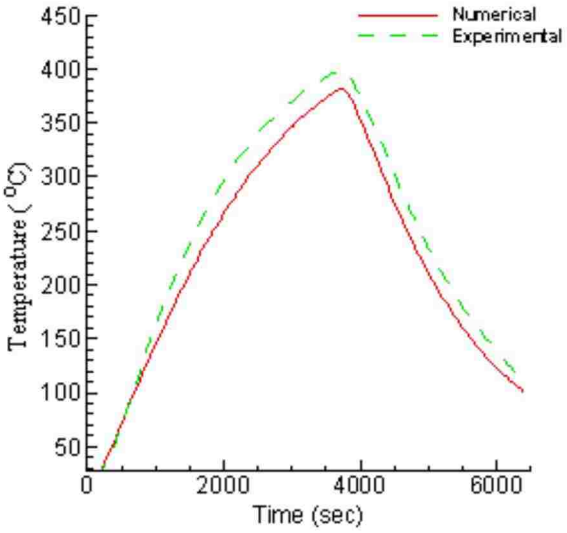

f) Capsule No. 6

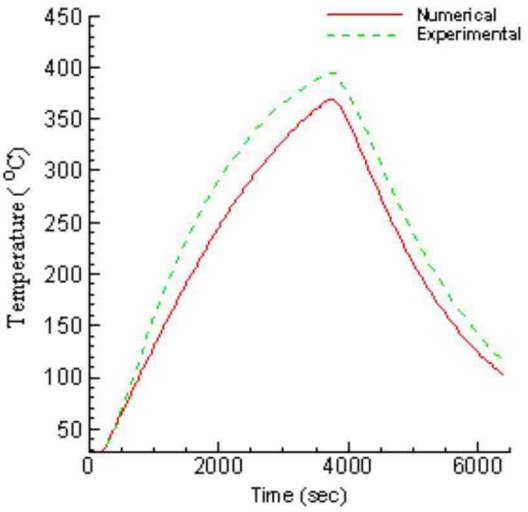

g) Capsule No. 7

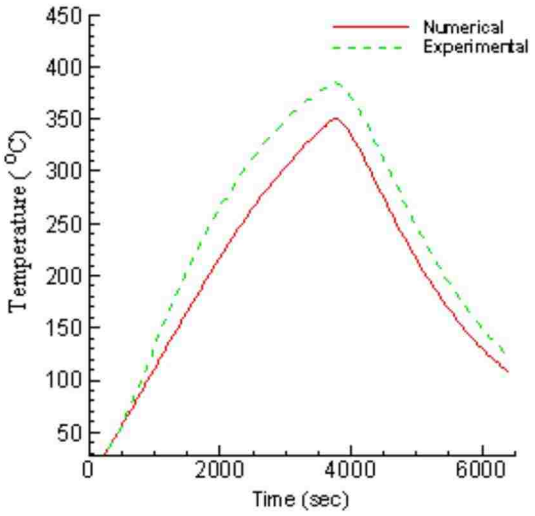

h) Capsule No. 8

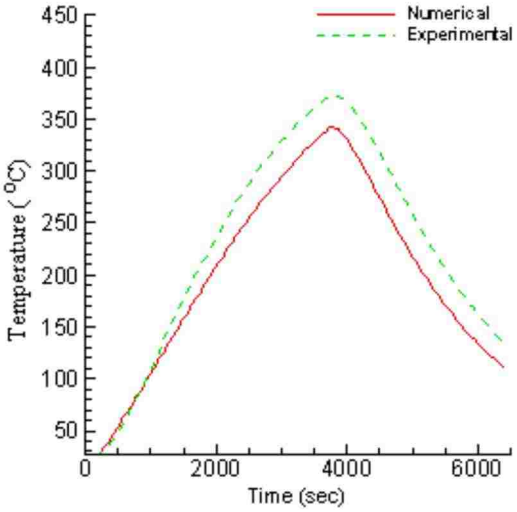

i) Capsule No. 9

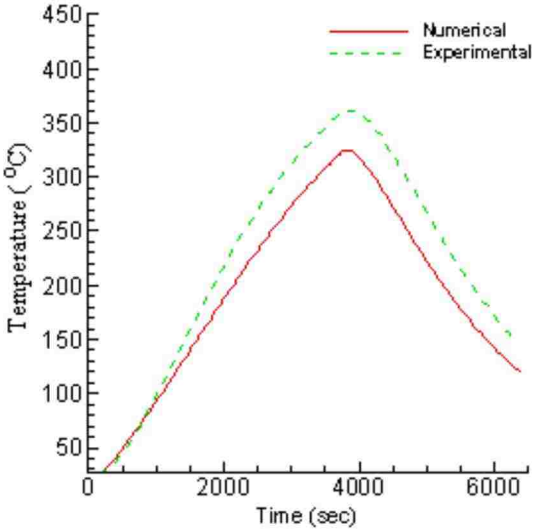

j) Capsule No. 10

Figure 47. The temperature of ten copper rods vs. time in the thermocline. Experiment is conducted by Zheng et al. [56].

Similarly, comparison between simulated and measured temperature of EPCM is made for $NaNO_3$ thermocline, as shown figure 48. The temperature in the last capsule is measured 6 mm above the bottom of the capsule. Temperature variation in time at this

point matches between experiments and simulation until the melting front reached the thermocouple. After the melting front passed, Predicted temperature is significantly below of the measured temperature. This can be attributed to the effect of natural convection. As presented earlier, the buoyancy – driven convection has profound effect during both charging and discharging processes. Thermocline simulation neglect the buoyancy driven – convection in the molten PCM.

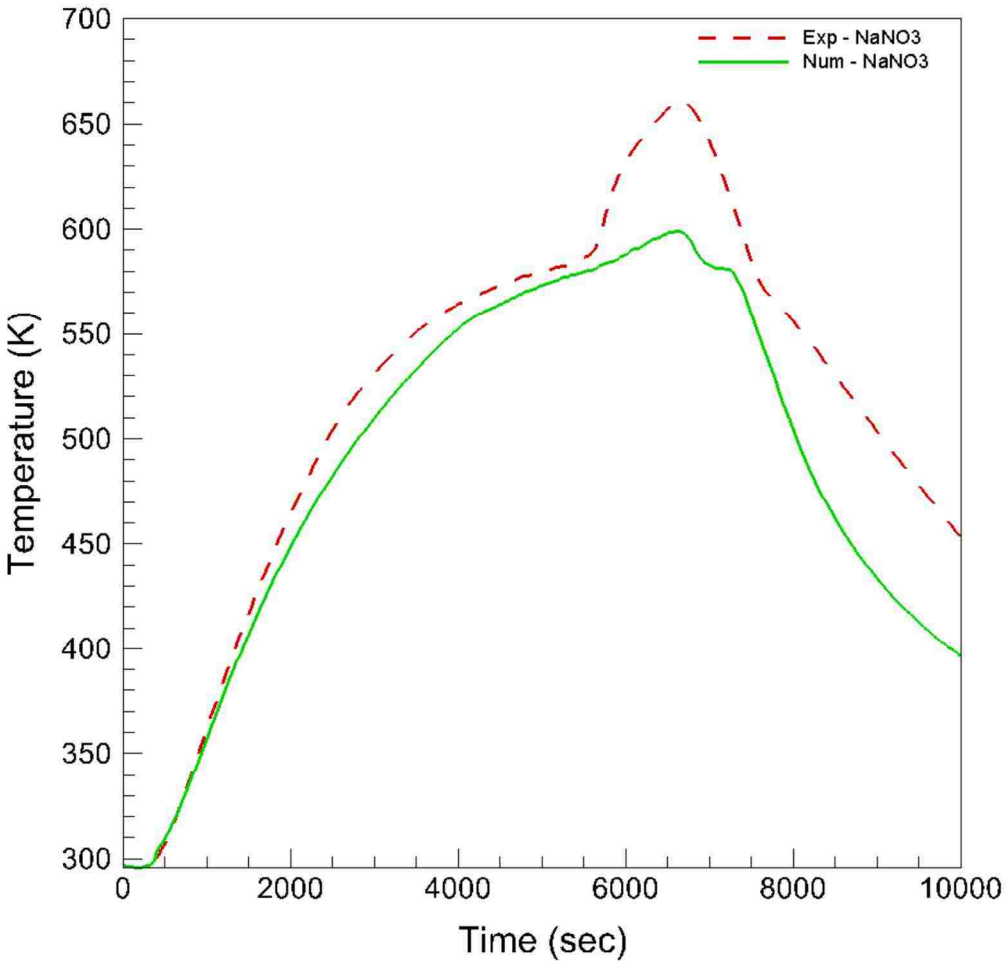

Figure 48. The temperature distribution for one cycle the charging and the discharging at 6mm from the bottom of the $NaNO_3$ capsule. Experimental observation is made by Zheng et al. [57]**.**

6.5. Results

Two dimensional transient heat transfer analysis is conducted for Copper and $NaNO_3$ thermocline. Charging and discharging are simulated using air as HTF. ANSYS FLUENT is employed to conducted simulation. Figure 49 (a – c) shows contours of the streamline at 4000 seconds. Thermocline contains several deflectors to direct the HTF around the EPCM in order to enhance heat transfer between HTF and EPCM.

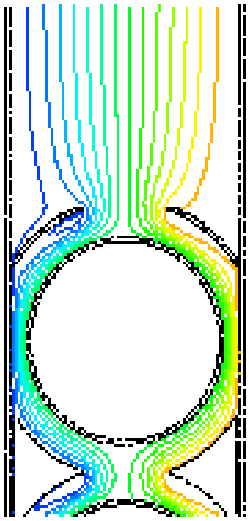

a) The streamlines around the first capsule

b) Streamlines in the middle section of the thermocline

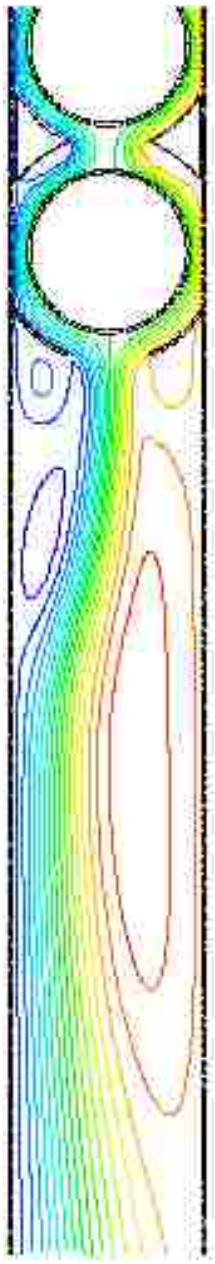

c) Streamline around the 10th capsule

Figure 49. Contours of stream lines in the thermocline at 4000 seconds.

6.5.1. Copper simulations

Figures 50 and 51 show the isotherms in the thermocline. Figure 50 illustrates the charging process at 1800 sec and at 3600 sec. Air enters thermocline at 700K.

Figure 51 depicts the isotherms during the discharging process at 4585 sec and 6200 sec. The cooling air enters at 300K.

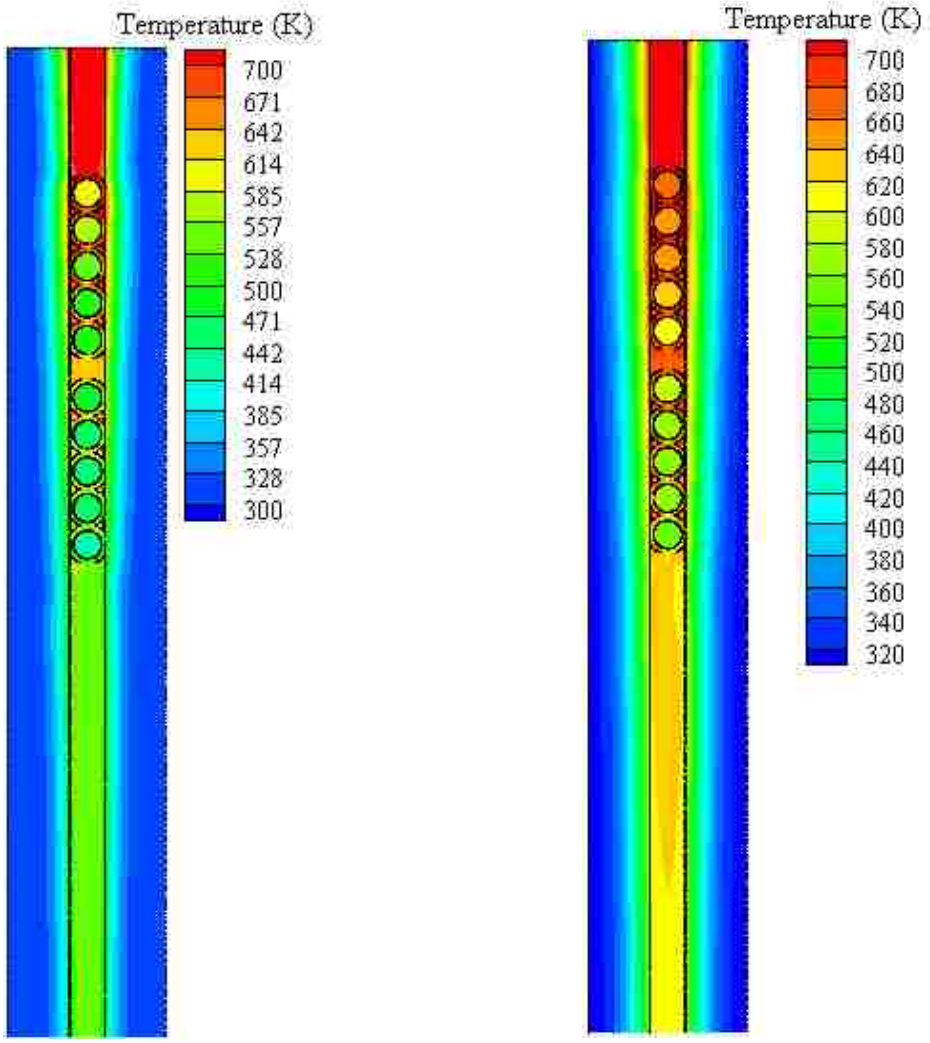

1800 seconds 3600 seconds

Figure 50. Isotherms in the thermocline during a charging process.

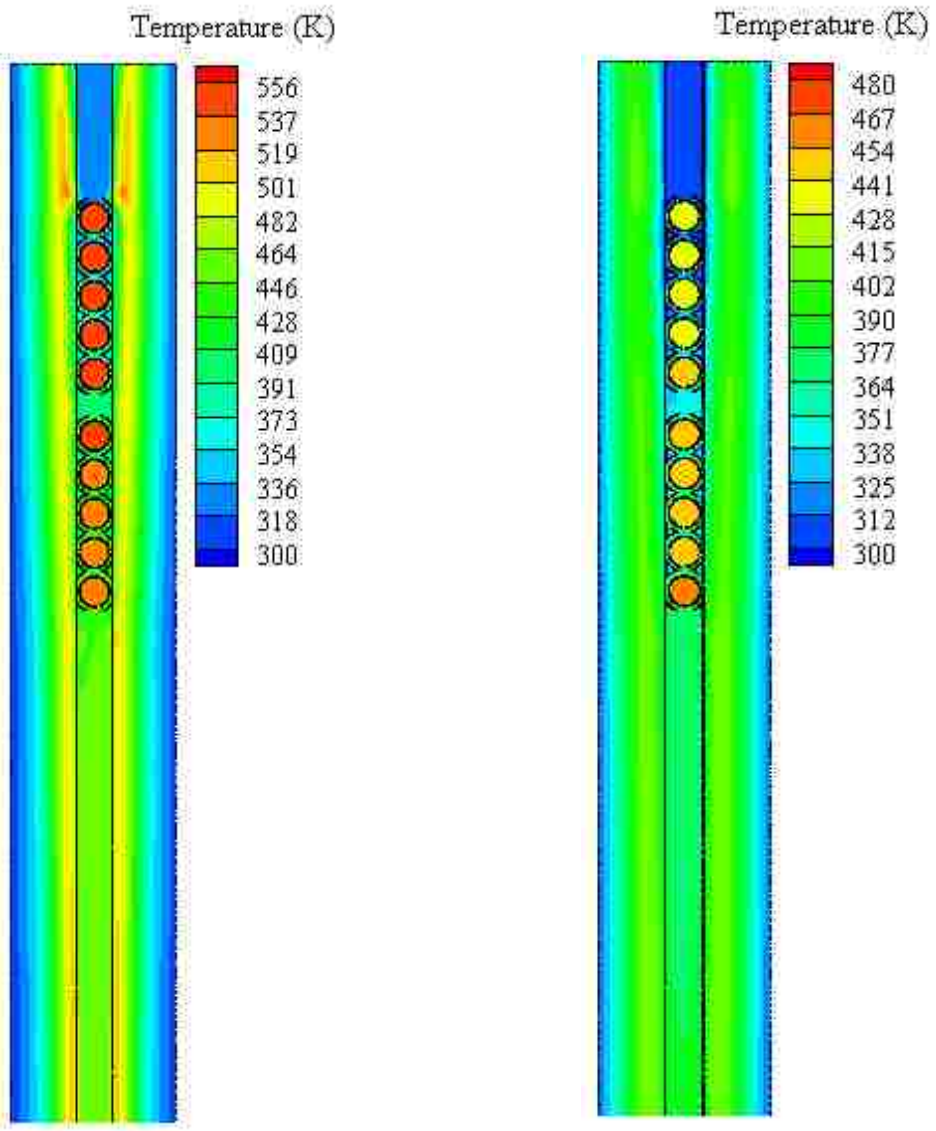

4600 seconds 6200 seconds

Figure 51. Isotherms in the thermocline during a discharging process.

Copper has very high thermal conductivity, thus it behaves as lump capacitance. It could only be very small temperature gradient in copper rods. The surface temperature of each rod is plotted during one thermal cycle consisting of a charging and a discharging process. The temperature of each rod increase in time during the charging process reaches maximum at the end of the charging process and decreases monotonically during the discharging process, as shown in figure 52. The temperature of the first rod is highest at all times during the charging process while the temperature of the last copper rod is the lowest at all times during the discharging process. The results agree well with experiments.

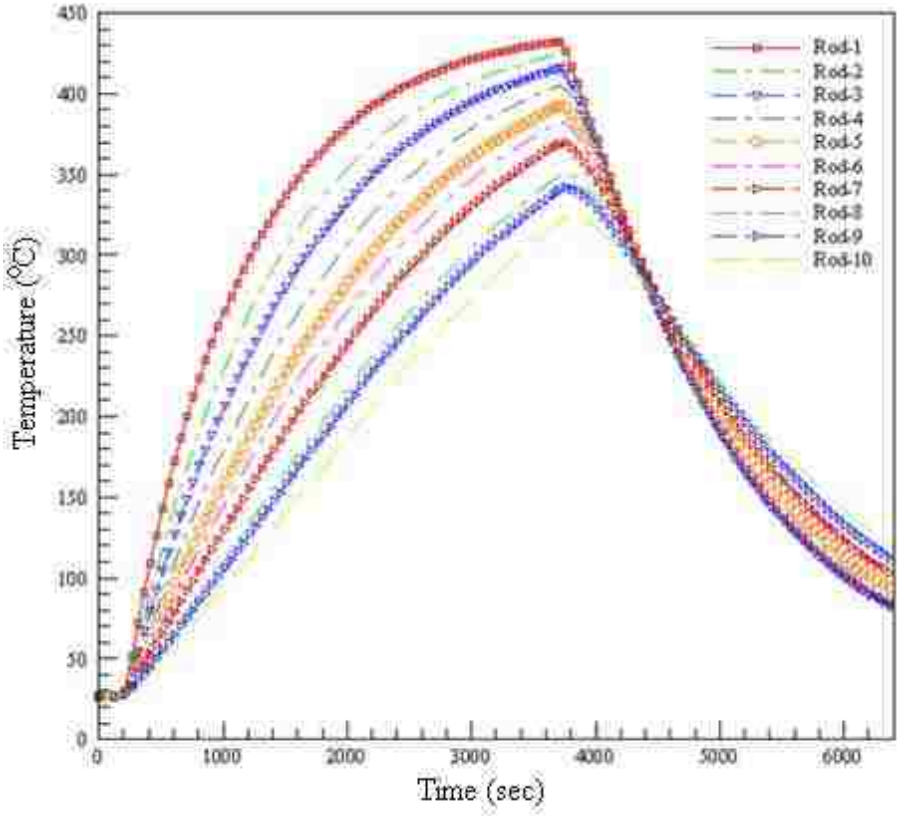

Figure 52. Temperature distribution for ten copper rods in the thermocline during one thermal cycle.

Figure 53 shows the total amount of energy released from air and the total amount of energy stored in copper capsules. Cumulative thermal energy storage in copper capsule is %72 of the energy released by the air. Other 28% of the energy includes energy stored at the wall of thermocline and insulations layers and heat losses from the thermocline.

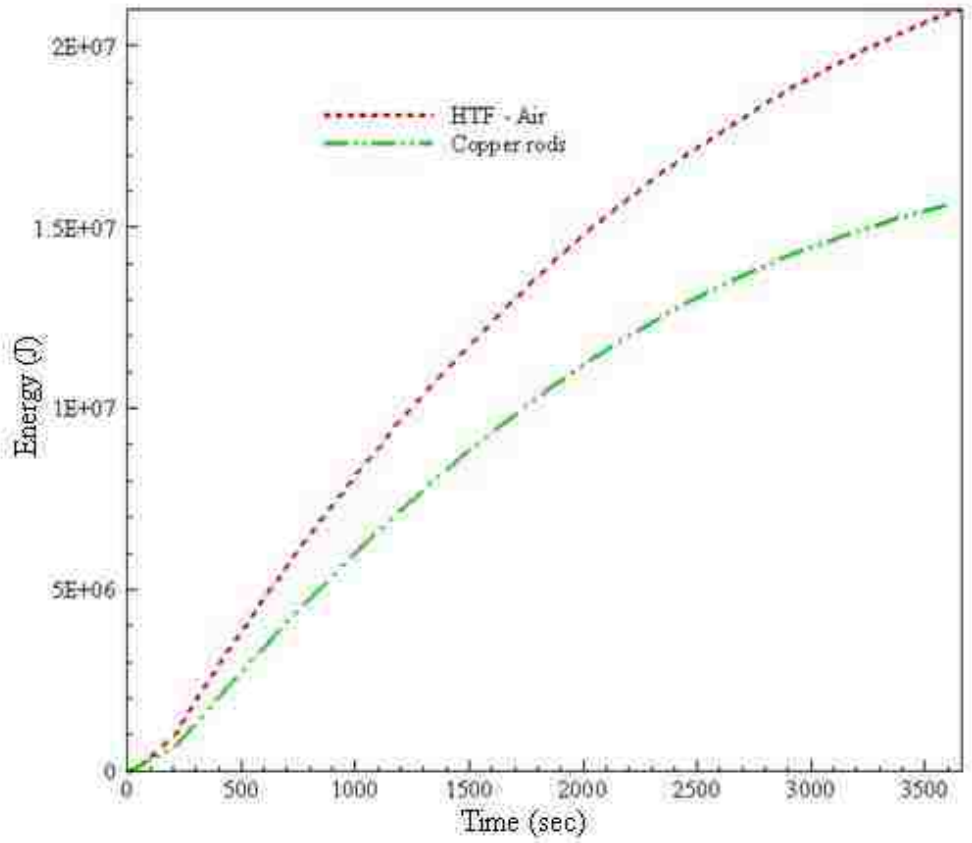

Figure 53. Energy released by HTF and energy stored in ten copper rods during the charging process.

6.5.2. $NaNO_3$ simulations

Figure 54 depicts the results of the simulation conducted for $NaNO_3$ in the thermocline. Figure 54(a) shows the isotherms at 4000 seconds during the charging process. Air,

HTF, flows from the top of the thermocline to the bottom. Air enters the thermocline at 700K. Figure 54(b) shows the melting front at 4000 seconds in each $NaNO_3$ EPCM. Since, the heat transfer to EPCM from HTF is nearly uniform along the surface of each EPCM tube the interface any instant is radially symmetric, as shown in figure 54(b). This is also due to the fact that the natural convection and the void in EPCM are neglected in the present simulation.

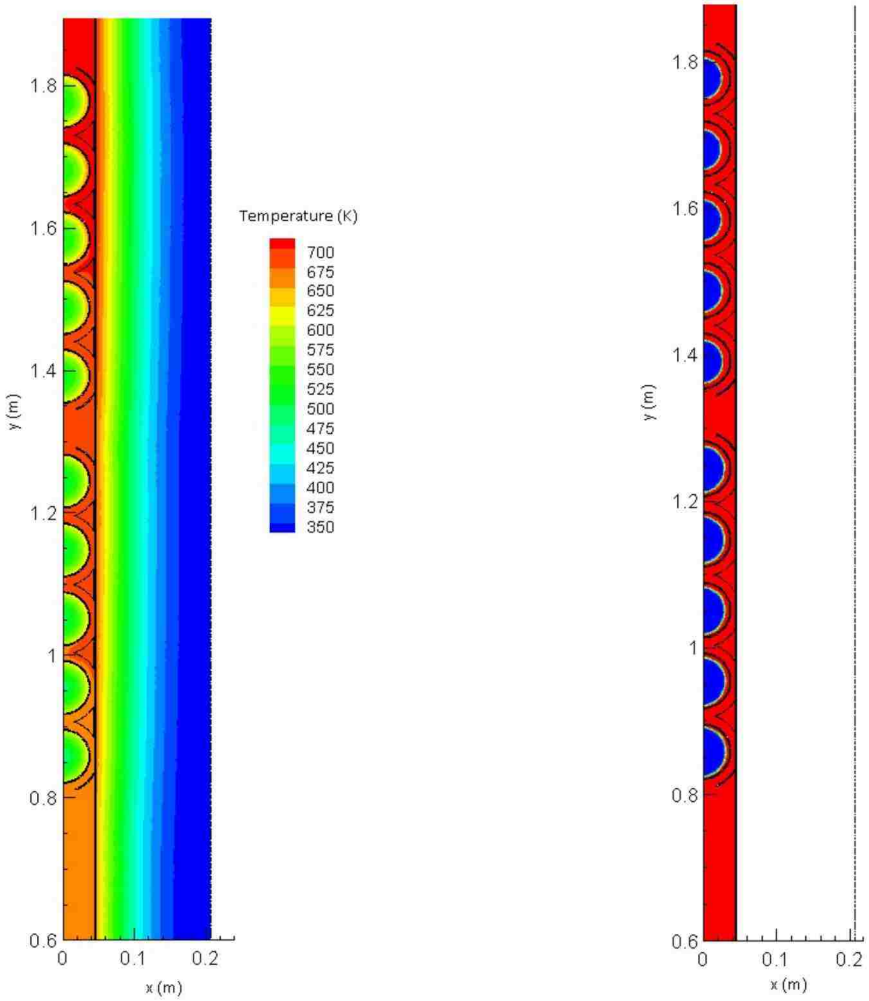

a) Contours of isothermal b) Contour of interface

Figure 54. Isotherms in the $NaNO_3$ thermocline at 4000 seconds during the charging process.

Figure 55 – 57 show the isotherms for different EPCMs in the thermocline at various times during the charging process. The temperature of first EPCMs is higher than that of last EPCMs. The isotherms are circulars inside the EPCM. Figure 56 shows that the temperature at the center of the first EPCM is 332K at 1200 seconds and it reaches to 570K at 8600 seconds.

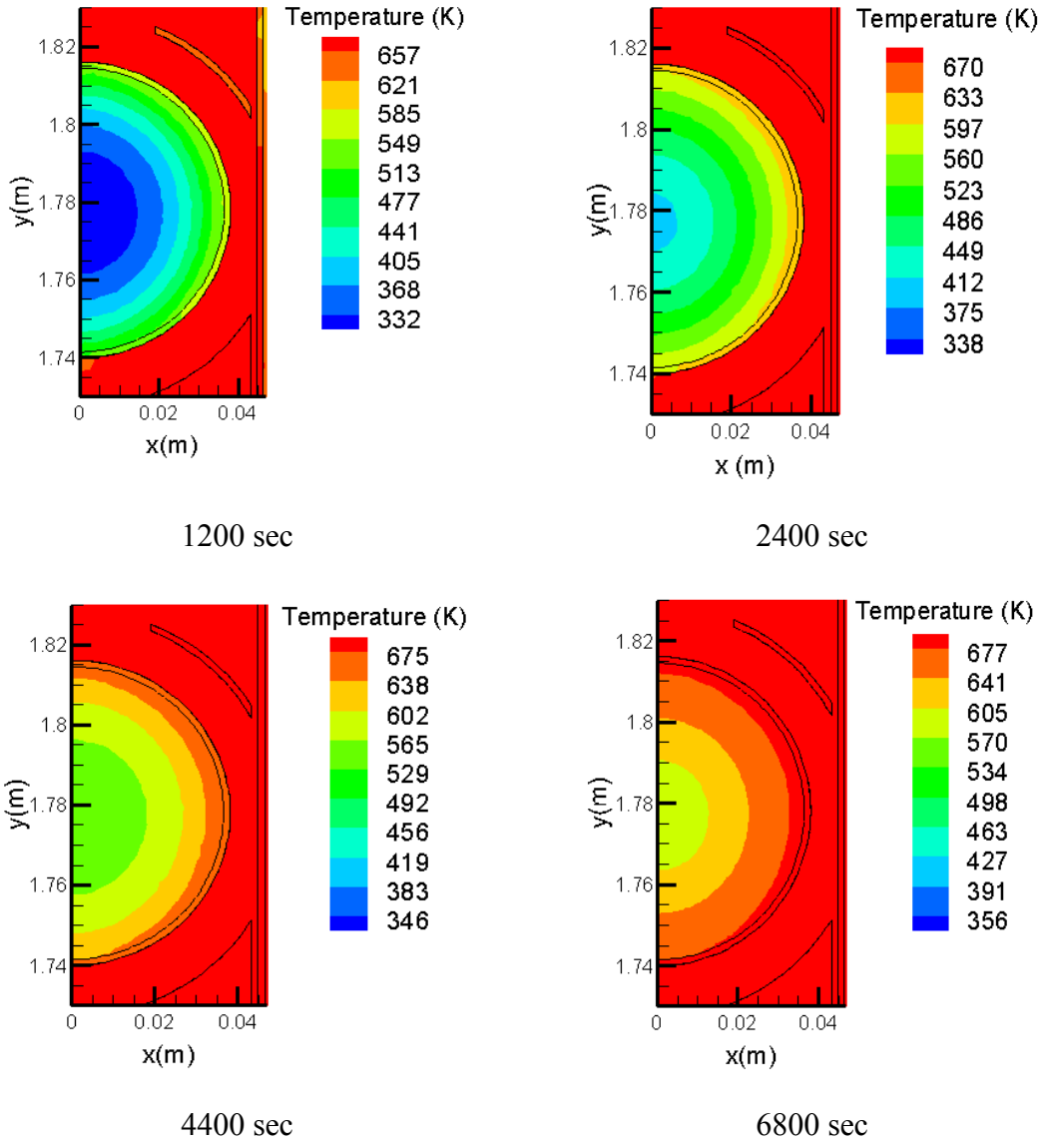

Figure 55. Isotherms around the 1st $NaNO_3$ EPCMs at varoius times during the charging process.

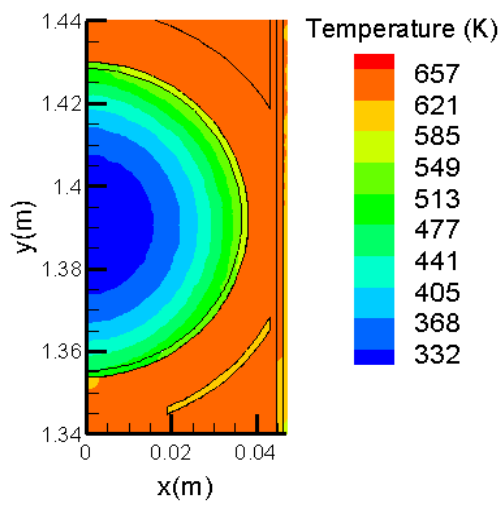

1200 sec

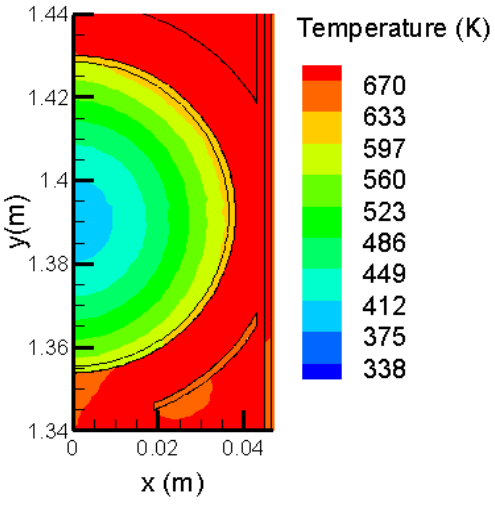

2400 sec

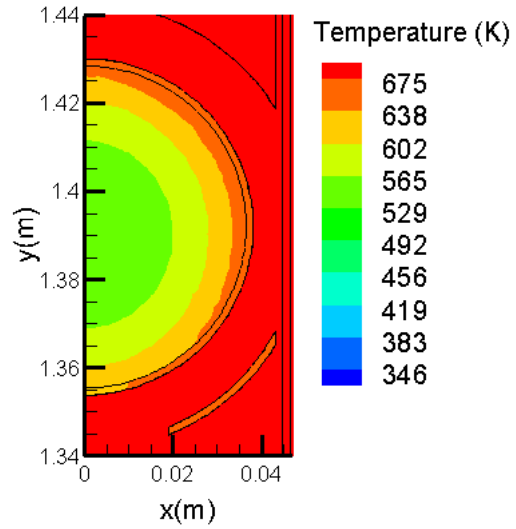

4400 sec

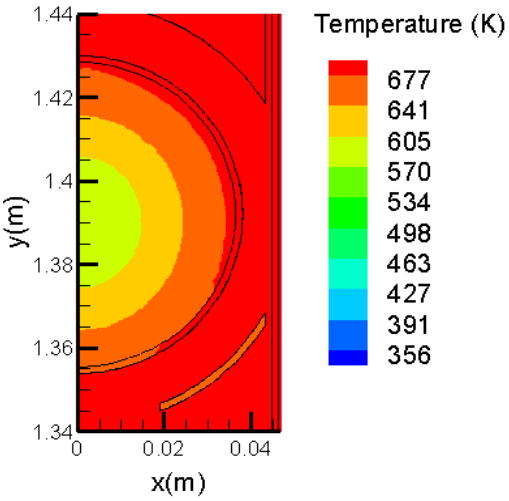

6800 sec

Figure 56. Isotherms around the 5th $NaNO_3$ EPCMs at varoius times during the charging process.

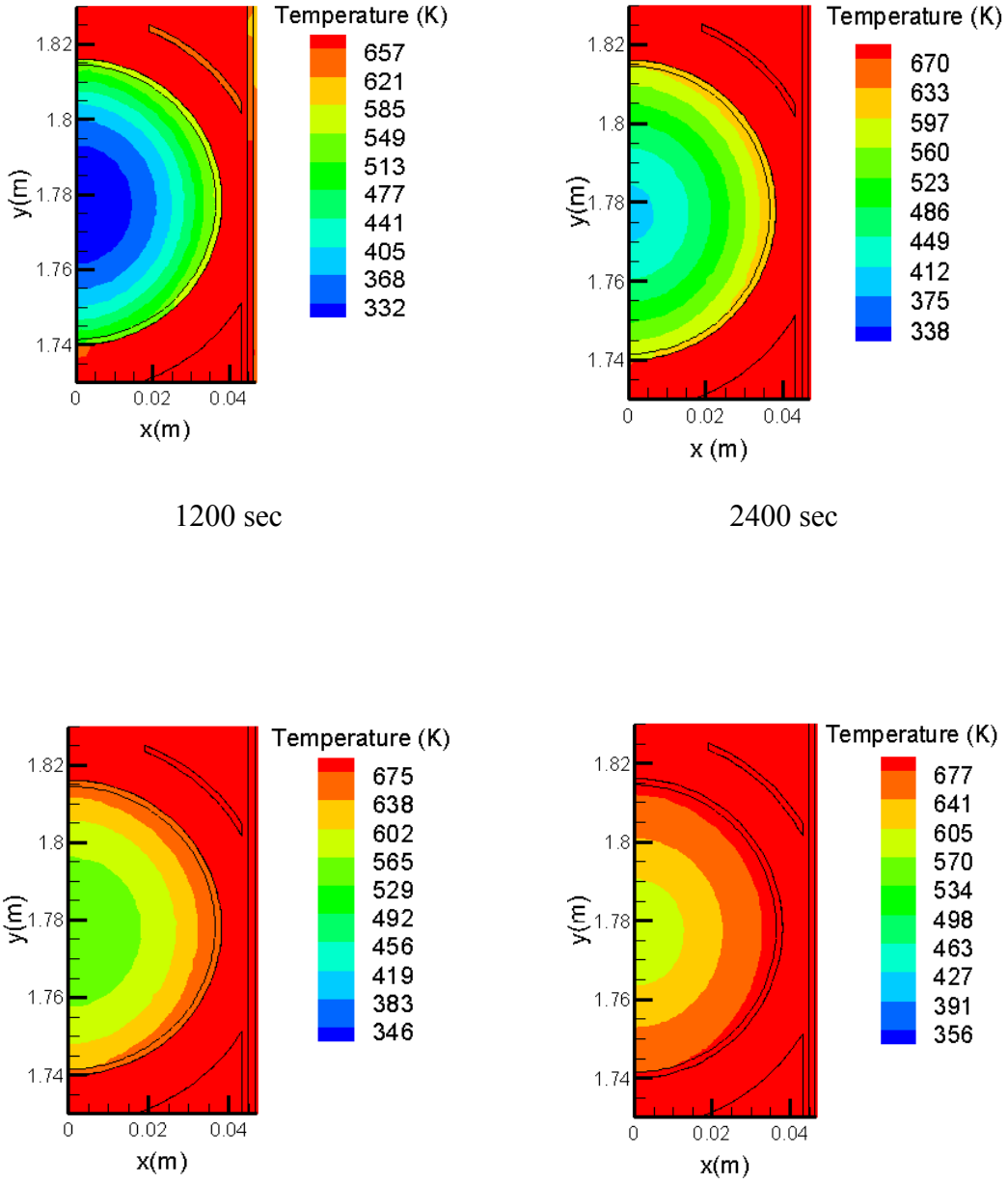

Figure 57. Isotherms around the 6th $NaNO_3$ EPCMs at varoius times during the charging process.

Figure 58 illustrates the isotherms of the last EPCM at various times during the charging process. The temperature of the last EPCM is lower than the others during the storing energy.

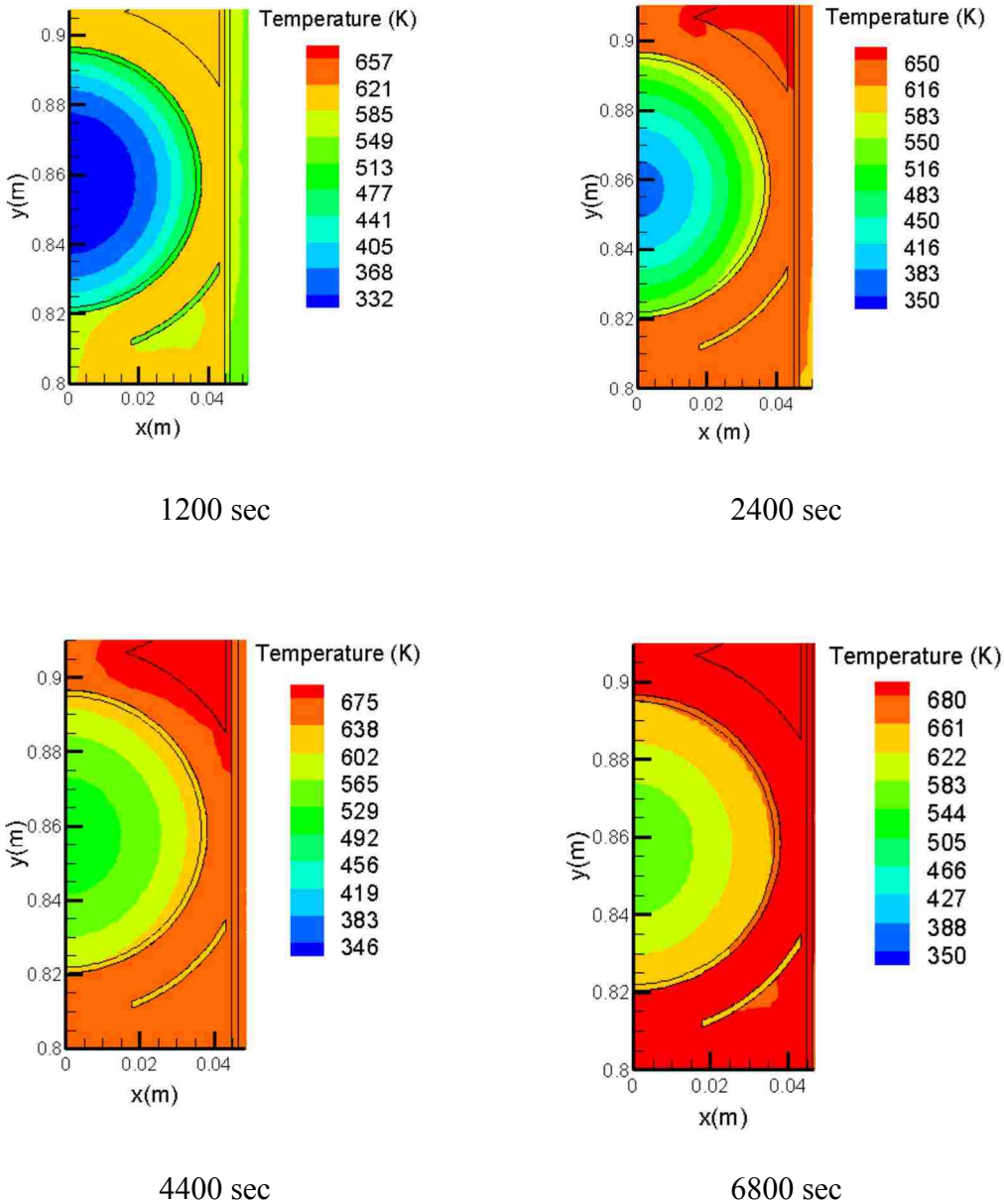

Figure 58. Isotherms around the 10th $NaNO_3$ EPCMs at varoius times during the charging process.

Figure 59 and 62 show the location of the propagating liquid/solid interface predicted by the enthalpy – porosity method at various times for the thermocline. The shape of the liquid/solid interface is nearly circular at all times. This is due to the fact that the HTF flow is turbulence and the heat transfer rate is high at the surface of EPCMs. The melting in the 9th EPCM has just started melting at 2400 seconds, as shown in figure 62.

Figure 63 has taken much longer to start melting.

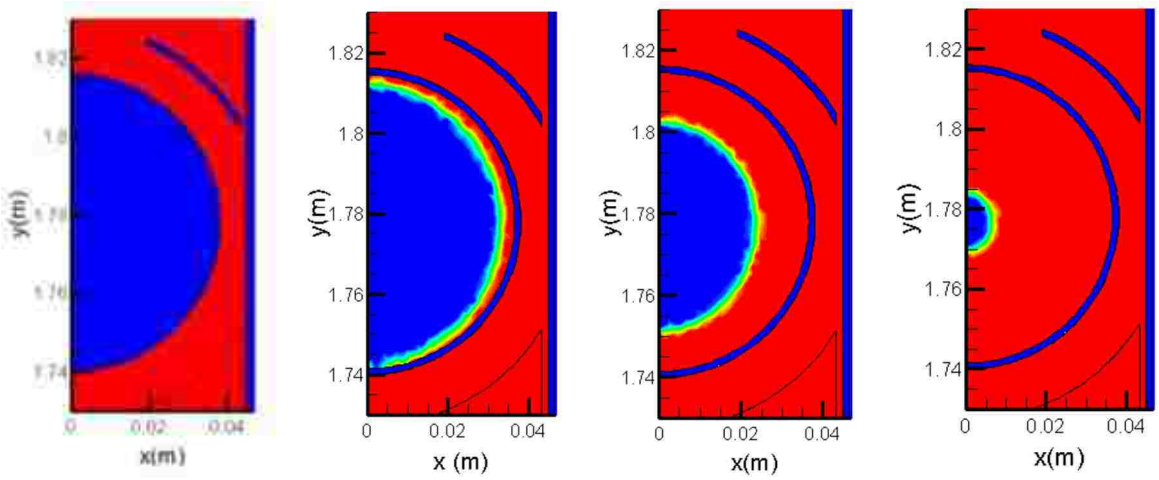

1200 sec 2400 sec 4400 sec 6800 sec

Figure 59. The location of solid/liquid interface in 1st $NaNO_3$ EPCMs at various times during the charging process.

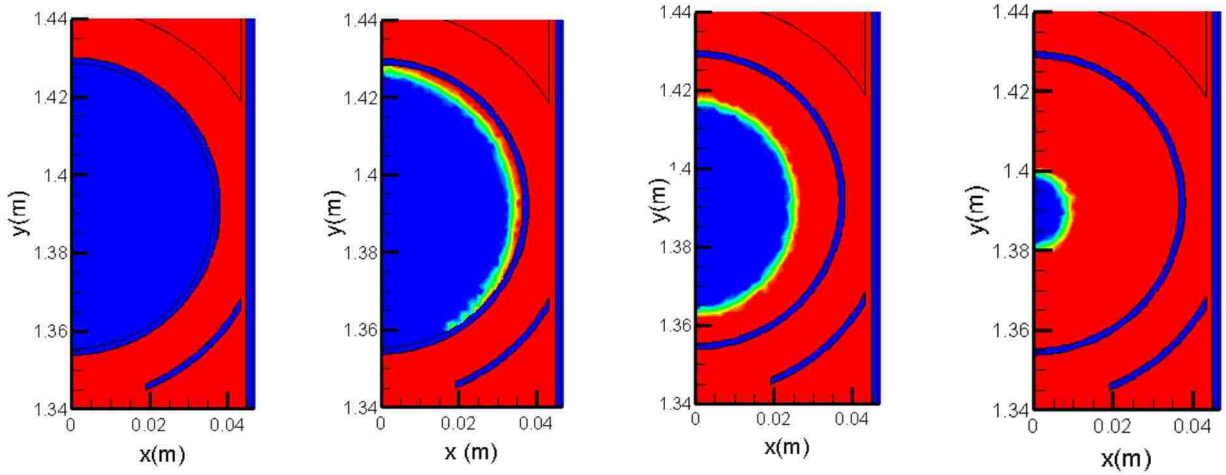

1200 sec 2400 sec 4400 sec 6800 sec

Figure 60. The location of solid/liquid interface in 5th $NaNO_3$ EPCMs at various times during the charging process.

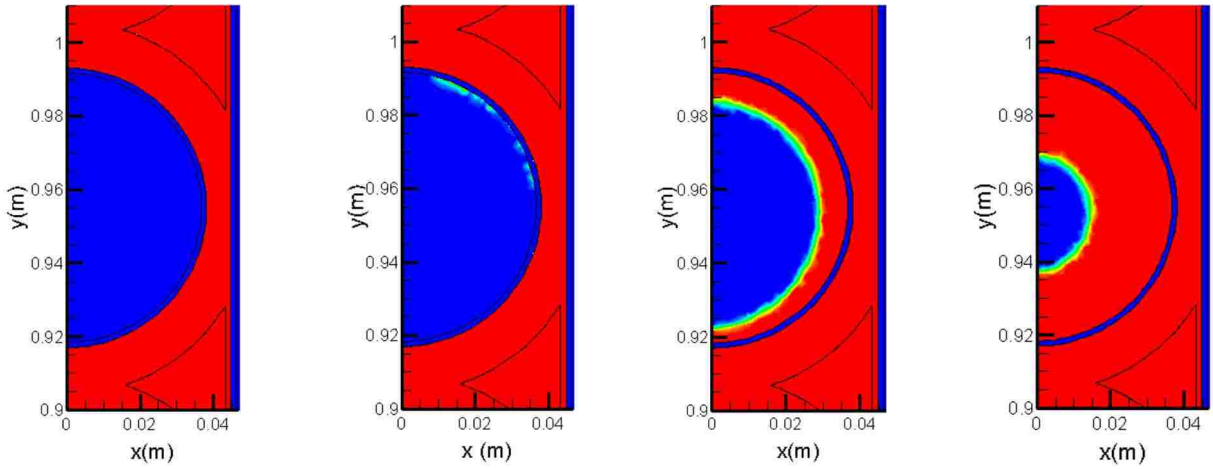

1200 sec 2400 sec 4400 sec 6800 sec

Figure 61. The location of solid/liquid interface in 9th $NaNO_3$ EPCMs at various times during the charging process.

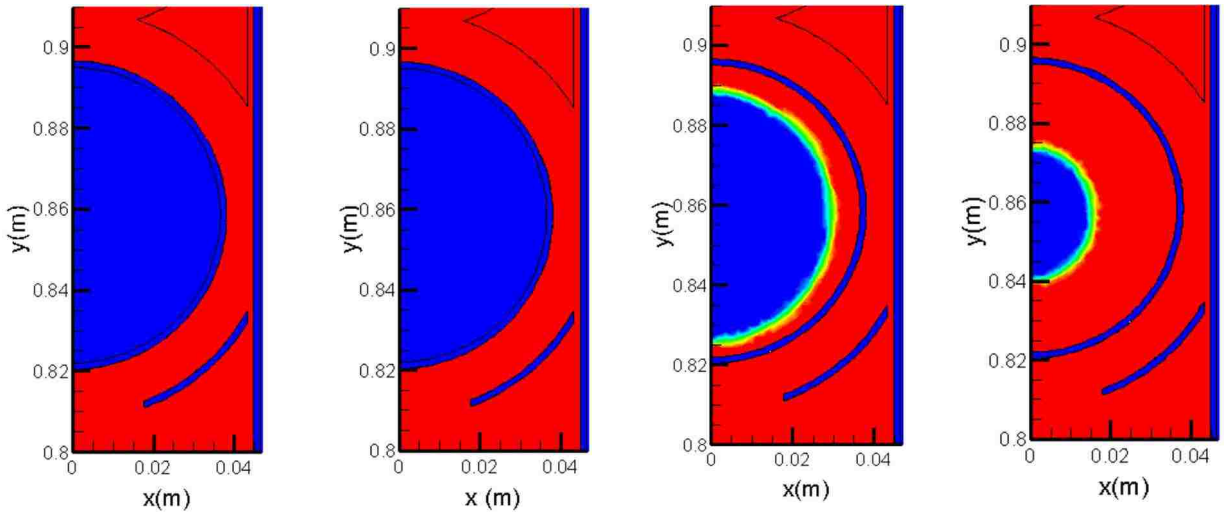

1200 sec 2400 sec 4400 sec 6800 sec

Figure 62. The location of solid/liquid interface in 10th $NaNO_3$ EPCMs at various times during the charging process.

Figure 63 shows the temperature evaluation in capsules #1, #5, #6, and #10 during one thermal cycle. Temperatures rise rapidly during the charging process in each capsule until the melting point is reached. Temperature in each rod a remains nearly constant as melting continues and decreases rapidly during the discharging process.

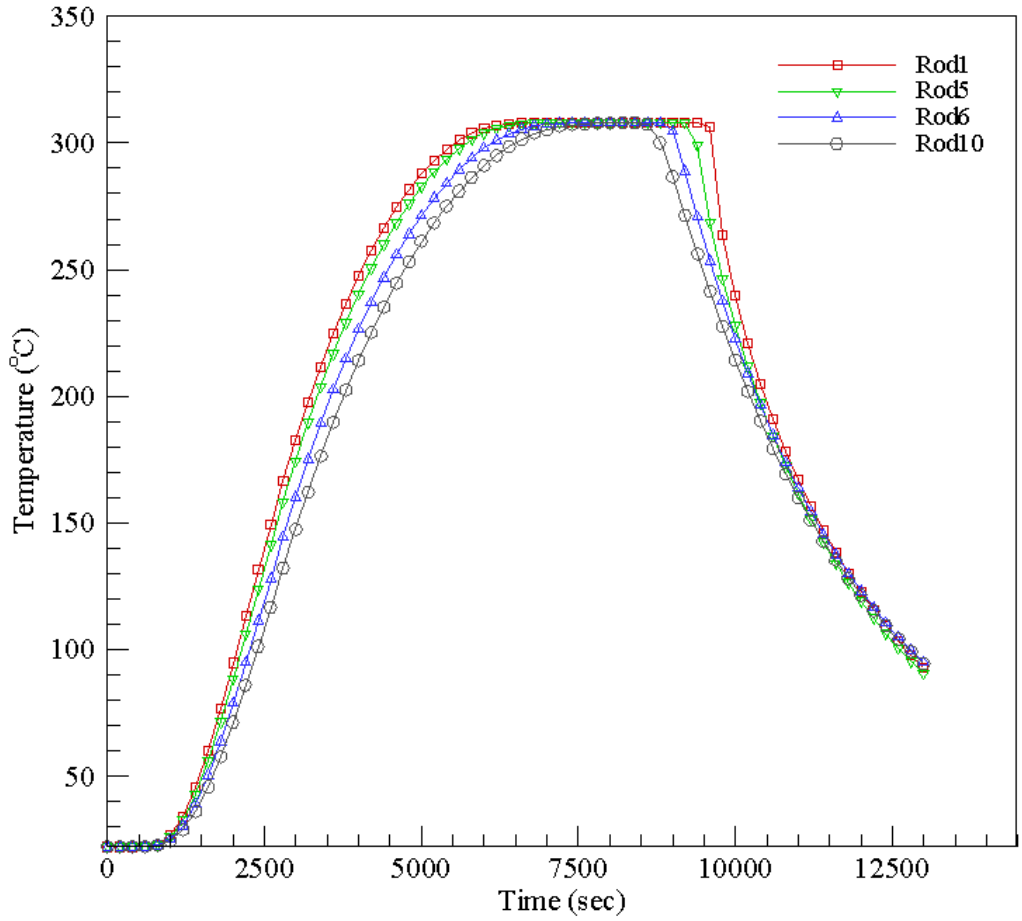

Figure 63. The temperature of several $NaNO_3$ EPCM capsule versus time during one thermal cycle.

Figure 64 depicts the convective heat transfer coefficient along the 10th $NaNO_3$ EPCM capsules at t = 4400 sec. The heat transfer coefficient follows similar pattern in each rod. The highest value of heat transfer coefficients is obtained near the front stagnation point at about 18º. The heat transfer coefficient is nearly uniform at 44 ($W/m^2\ K$) along the capsule except in the region near the front and rear stagnation point. Deflectors placed around the EPCM cause such uniform distribution of the heat transfer coefficient.

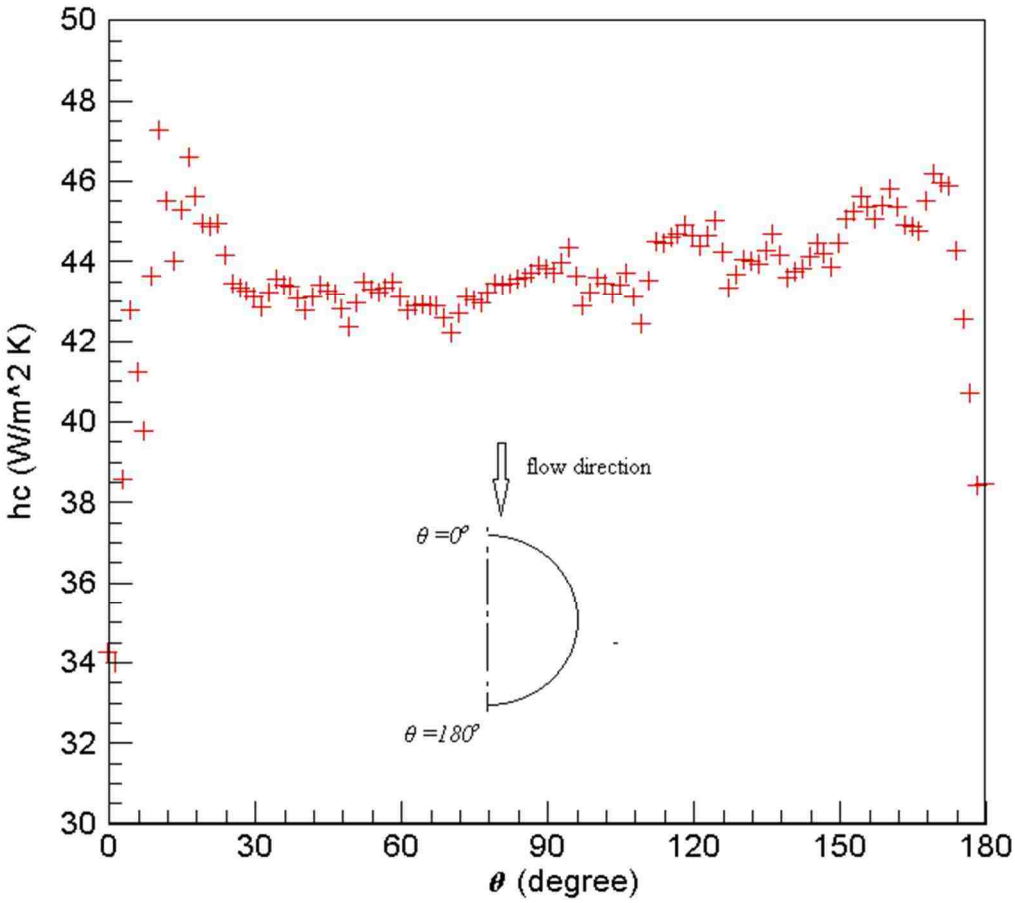

Figure 64. The heat transfer coefficients along the surface of the tenth EPCM at t = 4400seconds.

Figure 65 displays the energy released by the HTF and stored by EPCM capsules. Cumulative energy stored by EPCM capsules is 64.08% of the total energy released by the HTF. The latent heat storage is nearly 30% from the total of the energy stored in the EPCM capsule and the rest of the energy is stored as a sensible heat.

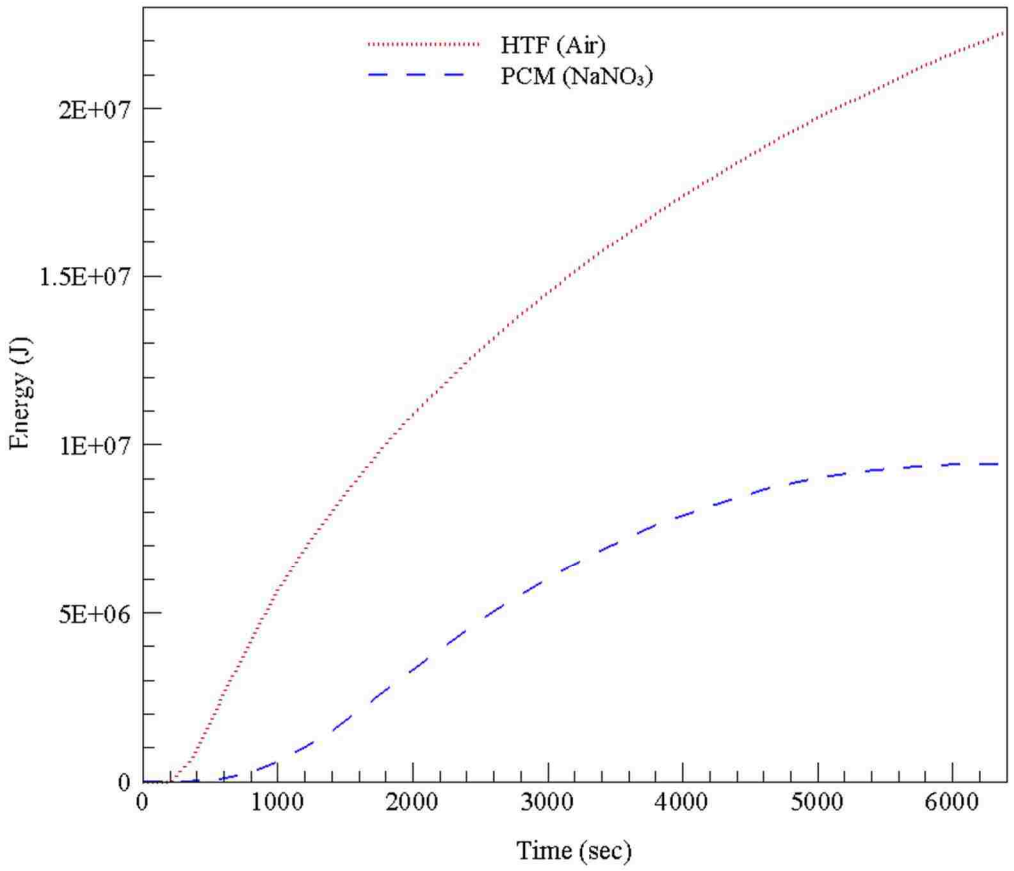

Figure 65. The energy released by HTF and the cumulative energy stored in ten $NaNO_3$ EPCMs during the charging process.

6.6. Conclusions

Enthalpy –porosity method is employed to model the heat transfer and the phase change of EPCM in the thermocline. RANS turbulence modeling is used to characterize the heat transfer fluid in thermocline. Copper rods and $NaNO_3$ EPCM are considered in the simulations. The predicted results match with the measured results which validates the mathematical models and the numerical methods. That also confirms that experimental

measurement is accurate. The results presented here aid the design and the optimization of high temperature thermal energy storage systems for concentrated power plants.

CHAPTER 7 – CONCLUSIONS

This work presents the heat transfer analysis of thermal energy storage using phase change material for high temperature applications. Numerical simulations have been conducted using ANSYS FLUENT. The geometries for all cases have created and meshed using Design Tools. The enthalpy – porosity method is employed to model heat transfer and phase change process inside the EPCM. Boussinesq approximation is applied to model the buoyancy – driven convection in the EPCM. The volume of fluid, VOF, is applied to model the multiphase flows of air and molten PCM. As results of simulation conducted here the following conclusion are drawn:

- The present study proves that enthalpy methods are valuable tools to study transport phenomena in phase changing systems.
- The interface location predicted by the enthalpy – porosity method agrees very well with front tracking method.
- The heat transfer process inside the EPCM capsule is impacted by the sizes of capsules, bigger size much longer melting time.
- The enthalpy-porosity method agrees well with experimental results for paraffin wax as a PCM to validate buoyancy – driven behavior.
- The buoyancy-driven convection in the molten PCM can shorten the storage time in the EPCM capsule.
- The effects of the buoyancy driven convection on the heat transfer time is strongly coupled with the heat transfer of the streaming fluid around the EPCM.
- Storage/retrieval times into/out of EPCM are strongly influenced by the flow characteristics of HTF near EPCM.

- The higher rate of heat transfer achieved with VP-1 as the HTF increases natural convection within the molten salt, thus reducing the total melting time.
- The presence of the air void at the top of the capsule reduces the heat transfer at the top of the capsule. The void also affects the shape of the solid/liquid interface, changing it from a circular shape to a mushroom shape.
- During the solidification process, the lack of natural convection in the liquid PCM and the low thermal conductivity of the PCM results in a solidification time that is 10 times longer than the melting time.
- The temperatures distribution of the simulation ten copper rods agree well with experimental results.
- The results of NaNO3 are in good agreement with experimental results until the NaNO3 reaches melting point (581K). The buoyancy-driven convection in the molten salt causes the deviations between predicted results and experimental results for the NaNO3 in the thermocline.
- Neglecting volume expansions of EPCM can also be the reason for this deviation between the predicted results and experimental observations in $NaNO_3$ thermocline.

The conclusions drawn can be further used to aid in the design of thermal energy storage modules for concentrating solar power plants.

REFERENCES

[1] E. Council, "its potential contribution to a sustainable energy future: its potential".

[2] I. Dincer and M. A. Rosen, Thermal Energy Storage Systems and Applications, second ed., New York: Wiley, 2011.

[3] A. Sharma, V. Tyagi, C. Chen and D. Buddhi, "Review on thermal energy storage with phase change materials and applications," *Renewable and Sustainable Energy Reviews,* vol. 13, pp. 318-345, 2009.

[4] M. M. Farid, A. M. Khudhair, S. K. Razack and S. Al-Hallaj, "A Review on Phase Change Energy Storage: Materials and Applications," *Energy Conversion and Management,* vol. 45, pp. 1597-1615, 2004.

[5] S. Neti, J. C. Chen, M. Z. Wojciech, A. Oztekin and K. Tuzla, "ENCAPSULATED PHASE CHANGE APPARATUS FOR THERMAL ENERGY STORAGE". US Patent 20110259544, 20 04 2001.

[6] B. Zalba, J. M. Marin, L. F. Cabeza and H. Mehling, "Review on thermal energy storage with phase change: materials, heat transfer analysis and applications," *Applied Thermal Engineering ,* vol. 23, pp. 251-283, 2003.

[7] H. Mehling and L. F. Cabeza, "Phase Change Materials and Their Basic Properties," *Thermal Energy Storage for Sustainable Energy Consumption,* vol. 234, pp. 257-277, 2007.

[8] Y. B. Kang, Y. P. Zhang, Y. Jiang and Y. X. Zhu, "A general Model for analyzing the thermal characterscics of a class of latent heat thermal storage system," *Journal of sloar energy engineering – transications of the ASME ,* vol. 121, pp. 185-193, 1999.

[9] T. Nomura, N. Okinaka and T. Akiyama, "Technology of latent heat storage for high temperautre application: A review.," *ISIJ international ,* vol. 50, pp. 1229-1239, 2010.

[10] W. Zhao, "Characterization of Encapsulated Phase Change Materials for Thermal Energy Storage," Theses and Dissertations. Paper 1135, Lehigh University, Bethlehem, 2013.

[11] Y. Zheng, W. Zhao, J. C. Sabol, K. Tuzla, S. Neti, A. Oztekin and J. C. Chen, "Encapsulated phase change materials for energy storage – characterization by calorimetry," *Solar Energy ,* vol. 87, pp. 117-126, 2013.

[12] R. Velraj, R. V. Seeniraj, B. Hafinr, C. Faber and K. Schwarzer, "Heat transfer enhancement in a latent heat storage system," *solar energy ,* vol. 55, pp. 171-180, 1999.

[13] S. Esakkimuthu, A. H. Hassabou, C. Palaniappan, M. Spinnler, J. Blumenberg and R. Velraj, "Experimental investigation on phase change material based thermal storage system for solar air heating applications," *Solar Energy,* vol. 88, pp. 144-15, 20133.

[14] J. Bony and S. Citherlet, "Numerical model and experimental validation of heat storage with phase change materials," *Energy and Buildings,* vol. 39, no. 10, pp. 1065-1072, 2007.

[15] A. Trp, "An experimental and numerical investigation of heat transferduring technical grade paraffin melting and solidification in a shell-and-tube latent thermal energy storage unit," *Solar Energy,* vol. 79, pp. 648-660, 2005.

[16] M. Veerappan, S. Kalaiselvam, S. Iniyan and R. Goic, "Phase change characteristic study of spherical PCMs in solar energy storage," *Solar Energy,* vol. 83, pp. 1245-1252, 2009.

[17] J. H. Ferziger and M. Peric, Computational Methods for Fluid Dynamics, third ed., New York: Springer, 2002, pp. 265-307.

[18] C. K. Chun and S. O. Park, "A fixed-grid finite difference method for phase change problems," *Numer. Heat Transfer, Part B ,* vol. 38, p. 59–73, 2000.

[19] M. Bhattacharya, T. Basak and K. G. Ayappa, "A fixed - grid finite element based enthalpy formulation for generalized phase change problems: role of superficial mushy region.," *International Journal Heat and Mass Transfer,* vol. 45, pp. 4881-4898, 2002.

[20] V. R. Voller, "FAST IMPLICIT FINITE-DIFFERENCE METHOD FOR THE ANALYSIS OF PHASE CHANGE PROBLEMS," *Numerical Heat Transfer, Part B,* vol. 17, pp. 155-169, 1990.

[21] J. A. Mackenzie and M. L. Robertson, "The Numerical Solution of One-Dimensional Phase Change Problems Using an Adaptive Moving Mesh Method," *Journal of Computational Physics,* vol. 161, pp. 537-557, 2000.

[22] A. D. Brent, V. R. Voller and K. J. Reid, "Enthalpy-porosity technique for modeling convection-diffusion phase change: application to the melting of a pure metal," *Numerical Heat Transfer,* vol. 13, pp. 297-318, 1988.

[23] O. J. Ilegbusi and M. D. Mat, "A Hybrid Model of the Mushy Region in Phase-Change Problems," *JOURNAL OF MATERIALS PROCESSING AND MANUFACTURING SCIENCE,* vol. 5, no. 3, pp. 209-224, 1997.

[24] F. E. Moore and Y. Bayazitoglu, "Melting within a spherical enclosure," *Journal heat transfer,* vol. 104, pp. 19-23, 1982.

[25] J. M. Khodadadi and Y. Zhang, "Effects of buoyancy-driven convection on melting within spherical containers," *Interntional Journal Heat Mass Transfer,* vol. 44, no. 8, pp. 1605-1618, 2001.

[26] K. A. R. Ismail and R. I. R. Moraes, "A numerical and experimental investigation of different containers and PCM options for cold storage modular units for domestic applications," *International Journal of Heat and Mass Transfer,* vol. 52, pp. 4195-4202, 2009.

[27] F. L. Tan, S. F. Hosseinizadeh, J. M. Khodadadi and L. Fan, "Experimental and computational study of constrained melting of phase change materials (PCM) inside a spherical capsule," *International Journal of Heat and Mass Transfer,* vol. 52, no. 15-16, pp. 3464-3472, 2009.

[28] E. Assis, L. Katsman, G. Ziskind and R. Letan, "Numerical and experimental study of melting in a spherical shell," *International Journal of Heat and Mass Transfer ,* vol. 50, no. 9, pp. 1790-180, 2007.

[29] S. Jayavell and S. Tiwari, "Numerical Investigation of Incompressible Flow Past Circular Tubes in Confined Channel," *CFD Letters,* vol. 1, pp. 1-14, 2009.

[30] P. Catalano, M. Wang, G. Iaccarino and P. Moin, "Numerical simulation of the flow around a circular cylinder at high Reynolds numbers," *International Journal of Heat and Fluid Flow,* vol. 24, pp. 463-469, 2003.

[31] P. ANAGNOSTOPOULOS and G. ILIADIS, "NUMERICAL STUDY OF THE BLOCKAGE EFFECTS ON VISCOUS FLOW PAST A CIRCULAR CYLINDER," *INTERNATIONAL JOURNAL FOR NLTMERICAL METHODS IN FLUIDS,* vol. 22, pp. 1061-1074, 1996.

[32] A. ROSHKO, "Experiments on the flow past a circular cylinder at very high Reynolds number".

[33] U. Piomelli, "Large-eddy simulation: achievements and challenges," *Progress in Aerospace Sciences,* vol. 35, pp. 335-362, 1999.

[34] M. Sahin and R. G. Owens, "A numerical investigation of wall effects up to high blockage ratios on two-dimensional flow past a confined circular cylinder," *PHYSICS OF FLUIDS,* vol.

16, no. 5, pp. 1305-1320, 2004.

[35] S. Ghosal and P. Moin, "The basic equations for the large eddy simulation of turbulent flow in complex geometry," *Journal of Computational Physics,* vol. 1, no. 118, pp. 24-37, 1995.

[36] D. C. Wilcox, Turbulence Modeling for CFD, New York: DCW Industries, 2006.

[37] M. Lesieur and O. Metais, "New Trends in Large-Eddy Simulations of Turbulence," *Annual Review of Fluid Mechanics,,* vol. 28, pp. 45-82, 1996.

[38] *ANSYS FLUENT Theory Guide,* 2010.

[39] V. Alexiades and A. D. Solomon, Mathematical Modeling of Melting and Freezing Processes, Washington D.C.: Hemisphere Publishing Corporation, 1993.

[40] V. R. Voller and C. Prakash, "A fixed grid numerical modeling methodology for convection-diffusion mushy region phase-change problems," *International Journal of Heat and Mass Transfer,* vol. 30, no. 8, pp. 1709-1718, 1987.

[41] V. Shatikian, G. Ziskind and R. Letan, "Numerical investigation of a PCM-based heat sink with internal fins: Constant heat flux," *International Journal of Heat and Mass Transfer ,* vol. 51, no. 5-6, p. 1488–1493, 2008.

[42] F. P. Incropera and D. P. DeWitt, Fundamentals of Heat and Mass Transfer, fifth ed., New York: John Wiley, Inc, 2002, pp. 491-502, 905-921.

[43] S. V. Patankar, Numerical heat transfer and fluid flow, Hemisphere Publishing Corporation, 1980.

[44] G. J. Janz, "Thermodynamic and transport properties for molten salts: correlation equations," *Journal of Physical and Chemical Reference Data 17 (suppl. 2) ,* vol. 79, 1988.

[45] D. Williams, "Assessment of Candidate Molten Salt Coolants for the NGNP/NHI Heat-Transfer Loop," Nuclear Science and Technology Division,, Oak Ridge, Tennessee., 2006.

[46] W. Zhao, S. Neti and A. Oztekin, "Heat Transfer Analysis of Encapsulated Phase Change Materials," *Applied Thermal Engineering,* vol. 50, no. 1, pp. 143-151, 2013.

[47] T. Bauer, D. Laing and R. Tamme, "Characterization of Sodium Nitrate as Phase Change Material," *International Journal of Thermophysics,* vol. 33, no. 1, pp. 91-104, 2012.

[48] G. J. Janz, C. B. Allen, N. P. Bansal, R. M. Murphy and R. Tomkins, *Physical properties data compilations relevant to energy storage. II. molten salts: data on single and multi-component salt systems,* Washington, D.C: U.S. Department of Commerce, National Bureau of Standards, pp. 142-154 , 1979.

[49] Y. Zheng, W. Zhao, J. Sabol, K. Tuzla, S. Neti, A. Oztekin and J. Chen, "Encapsulated phase change materials for energy storage - characterization by calorimetry,," *Solar Energy,* vol. 87, pp. 117-126, 2013.

[50] Solutia, "Therminol VP-1 Heat transfer Fluid by Solutia,," Technical Bulletin 7239115B, , St. Louis, MO, 1999.

[51] M. Ashjaee, S. Amiri and K. Habibi, "Slot Jet Impingement Heat transfer from an Isothermal Circular Cylinder," *Thermal Issues in Emerging Technologies, ThETA 2,* vol. 54, pp. 399-404, 2008.

[52] E. Buyruk, "Heat Transfer and Flow Structures Around Circular Cylinders in," *Turkish Journal of Engineering and Environmental Sciences,* vol. 23, pp. 299-315, 1999.

[53] E. Assis, G. Ziskind and R. Letan, "Numerical and experimental study of solidification in a spherical shell," *Journal of Heat Transfer,* vol. 131, no. 2, pp. 024502-1 - 024502-5 , 2008.

[54] B. Launder, G. Reece and W. Rodi, "Prograss in the development of a Reynolds - stress turbulence closure," *Journal Fluid Mechanics ,* vol. 68, no. 3, pp. 537-566, 1975.

[55] B. Kumar and S. Mittal, "Effect of blockage on critical parameters for flow past a circular cylinder," *INTERNATIONAL JOURNAL FOR NUMERICAL METHODS IN FLUID,* vol. 50, pp. 987-1001, 2006.

[56] Y. Zheng, "Thermal energy storage with encapsulated phase change materials for high temperature applications," Lehigh University, Bethlehem, USA, 2015.

[57] Y. Zheng, J. L. Barton, K. Tuzla, J. C. Chen, S. Neti, A. Oztekin and W. Z. Misiolek, "Experimental and Computational Study of Thermal Energy Storage with Encapsulated NaNO3 for High Temperature Applications," *Solar Energy,* Nov 2014 - Under Process.

[58] Y. Zheng, K. Tuzla, J. C.Chen, J. Sabol, S. Neti, A. Oztekin and W. Z. Misiolek, "Thermal Energy Storage with Encapsulated Phase Change Materials for Concentrating Solar Plant Applications," in *International Conference on Massive Energy Storage, ECI*, Newport Beach , CA, USA, Jun 2013.

[59] M. Lesieur and O. Metais, "New Trends in Large-Eddy Simulations of Turbulence," *Annual Review of Fluid Mechanics,* vol. 28, pp. 45-82, 1996.

VITA

Ali F. Elmozughi was born on January 21, 1976 in Tripoi – Libya. He is a proud husband of Narjes Shibani and proud father of Farah and Ameer. He completed his Bachelor degree in Mechanical Engineering in Tripoli University in Libya in 2000. He completed his Master of Science degree in Mechanical Engineering in 2007. He also participated in the Lehigh University's Industrial Assessment Center program. Afterward, he entered the P.C. Rossin College of Engineering and Applied Science at Lehigh University, USA, to pursue his Doctor of Philosophy degree in Mechanical Engineering in 2009.